Development of Position Controller for Pump Controlled Cylinder

Christian Black Jørgensen

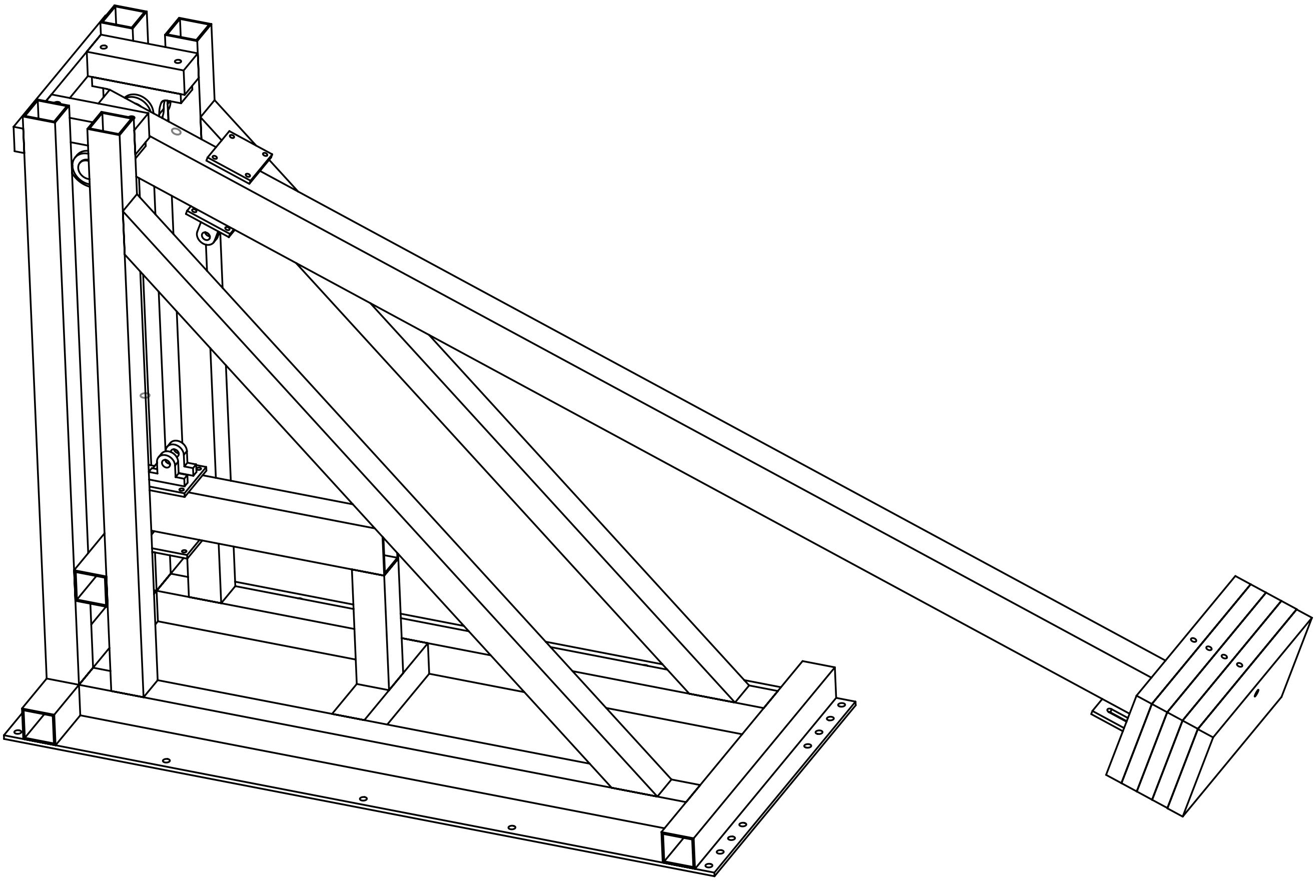

AALBORG UNIVERSITET

Student Report

Master Thesis | October 2018 | Aalborg University | Mechatronics

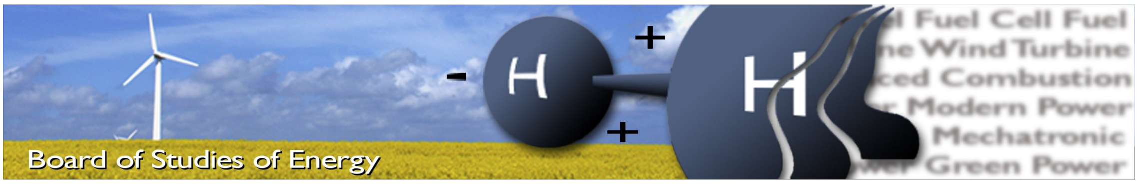

Title:	Development of Position Controller for Pump Controlled Cylinder
Semester:	10
Semester theme:	Mechatronic system design
Project period:	14/06/18 to 04/10/18
ECTS:	30
Supervisor:	Lasse Schmidt
Project group:	MCE4-1022

Christian Black Jørgensen

Synopsis:
The goal of this project is to develop different position controllers for a pump controlled crane located at the University of Agder.
A Simulink model has been developed and validated through experimental results. The model has been linearised in order to design linear controllers. VFF and linear position controllers (based on HPPF) have been designed and implemented on the experimental setup. The crane is capable of a static load holding operation by closing 2 POCV's. However, during this operation the pump pressure drops due to leakage. The low pump pressure results in a position drop when the POCV's are re-opened, and hereby the system begins to oscillate. Therefore different pressure controllers are developed such that the position drop can be reduced. FFF and PFF have also been implemented, and hereby the position drop is reduced from 2.5mm to 0.6mm. Through experiments it is shown that the maximum deviation from a given trajectory is kept below 10mm and the average error is kept below 1mm.

Copies:	1
Pages, total:	129
Appendix:	32
Supplements:	Annex

By signing this document, each member of the group confirms that all group members have participated in the project work, and thereby all members are collectively liable for the contents of the report. Furthermore, all group members confirm that the report does not include plagiarism.

Abstract

The goal of this master thesis is to develop different position controllers such that at given trajectory can be followed accurately.

The experimental setup is a pump controlled crane located at the University of Agder, and the crane is capable of a static load holding operation. This operation is activated by closing two pilot operated check valves. Hereby the cylinder can be kept in a static position without the use of energy. However, a challenge with the load holding operation is that the pressure on the high pressure side of the pump drops due to leakage. This means that when the pilot operated check valves are reopened then cylinder drops and pressure oscillations occur.

In order to design position controllers and to counter the position drop (when the pilot operated check are opened) then firstly a nonlinear model has been developed. The nonlinear model is validated through experiments and then linearised. The linearisation shows a resonance peak located at 12 rad/s, and therefore it is decided to develop high-pass filtered pressure feedback in order to increase the damping of the system. Velocity feedforward and position controllers are also developed and implemented on the experimental setup.
Furthermore, in order to counter the position drop when the pilot operated check valves are opened then pressure controllers are designed. The idea is to build up pressure before the opening of the pilot operated check valves. Through experiments it is shown that the pressure controller reduces the position drop, but the position drop still exceeds the limitations stated in the problem statement.

It is was not foreseen that the position drop would exceed the limitations stated in the problem statement.

In order to counter the position drop, the Simulink model is modified. The modified Simulink model improves the accuracy of the simulated results, and it is used to develop and test switching logic for flow feed forward and pressure feed forward. Both feed forward methods have been implemented on the experimental setup, and they both reduce the position drop significantly. Hereby the position drop is kept within the limits stated in the problem statement.

Two different trajectories for position have been developed and the controllers have been tested. It is shown that for both trajectories the average error is kept below 1mm and that the maximum deviation from the trajectory is 10mm. Furthermore, it is shown that the position drop when the pilot operated check valves are opened can be reduced from 2.5mm to 0.6mm.

Preface

This project is written by Christian Black Jørgensen at the Department of Energy Technology at Aalborg University (AAU) in the period 14.06.2018 to 04.10.2018.
The project is a 10. semester master thesis in specialization in Mechatronic Control Engineering.
The purpose of this project is to design and implement position controllers for a pump controlled crane located at the University of Agder.

The following software has been utilised in this project:

- *MATLAB/Simulink* - used for modeling and data processing.
- *Maple* - used for algebraic manipulation of equations.
- *SolidWorks* - used for 3D drawings.
- *Visio 2016* - used for making illustrations.
- *Inkscape* - used for making illustrations.

Reading Guide: A nomenclature is available at page IX, which lists all the constants, variables, quantity symbols, term abbreviations and any accompanying units used in this project.
All literature used in this project can be found in the bibliography at page 81, and is shown (when possible) in the following manner:

$$[Author][Title][Publisher][Year][ISBN][URL]$$

IEEE reference style is used in this report. Therefore the references are marked numbers in enclosed square brackets [Number]. An example: [13].

When figures, tables and equations are referenced it will be shown as: Chapter, no. of figure/table/equation. An example: 4.9.
Captions with relevant information are provided directly underneath figures and tables.

At page 85 a list off relevant constants used throughout this project can be found.

Attached to the report is there an attached ZIP-file which contains the models, the recorded data and a PDF version of the report.

I would like to thank Ph.D research fellow Daniel Hagen for helping with the implementation work of the different controllers and for good discussions regarding the experimental setup. Furthermore, I would like to thank associate professor Lasse Schmidt and Ph.D fellow Søren Ketelsen for guiding me through the project and always keeping their door open for me.

Nomenclature

The nomenclature includes lists of quantity symbols and term abbreviations which are used throughout the report. All units are in accordance with the SI-system, unless otherwise stated. The units are presented in chronological order.

Symbol	**Quantity**	**Unit**
M	Mass	kg
I	Mass moment of inertia	kg m^2
ω	Motor speed	rad/s
$\omega_{n,m}$	Eigenfrequency of the motor	rad/s
$\zeta_{n,m}$	Damping of the motor	-
p_i	Pressure	Pa
Q_i	Flow	m^3/s
F_i	Force	N
V_g	Displacement, geometric coefficient	cm^3/Per revolution
K_V	Displacement coefficient	m^3/rad
K_L	Leakage coefficient	m^3/(Pa s)
V_g	Displacement, geometric constant	m^3/(2π)
$x_{cv,n}$	Normalised opening of check valve	-
V_i	Volume	m^3
β_i	Bulk modulus constant	Pa
γ	Gas constant	-
$x, \dot{x}, \ddot{x}$	Cylinder position/velocity/acceleration	m, m/s, m/s^2
L_c	Maximum stroke length of cylinder	m
ε_{air}	Volumetric ratio of free air in the fluid	-
c_{ad}	Adiabatic constant of air	-
A_i	Surface area	m^2
τ_i	Torque	Nm
$\theta_i, \dot{\theta}_i, \ddot{\theta}_i$	Angular position/velocity/acceleration	rad, rad/s, rad/s^2
B_i	Viscous friction coefficient	Nm s
α_i	Constant angle	rad/s
$\mathcal{L}$	Lagrangian of the system	J
$\mathcal{K}$	Kinetic energy of the system	J
$\mathcal{P}$	Potential energy of the system	J
l_i	Length	m
m_i	Mass of link	kg
g	Gravitational constant	m/s^2
$\underline{\underline{D}}$	Inertia matrix	-
$\underline{\underline{C}}$	Matrix	-
ϕ	Gravitational vector	-
k_s	Spring constant	N/m
η_p	Efficiency of the pump	-
d_{ii}	Entrance in $\underline{\underline{\mathrm{D}}}$	-

$K_{\phi i}$	Linearisation constant	-
$K_{\tau i}$	Linearisation constant	-
K_{LAi}	Linearisation constant	-
$\underline{\underline{A}}$	State matrix	-
$\underline{\underline{B}}$	Input matrix	-
$\underline{\underline{C}}$	Output matrix	-
$\underline{x}, \underline{\dot{x}}$	State vector and derivative of state vector	-
$\underline{u}$	Input vector	-
$\underline{y}$	Output vector	-
e_{ref}	Error between reference and measured parameter	-
T_i	Time interval	s
t_i	Specific time point	s
ρ_{steel}	Density of steel	kg/m^3
r	Radius	m

Abbreviation	**Meaning**
Sat	Saturation
CV	Check Valve
POCV	Pilot Operated Check Valve
RPM	Rounds Per Minute
GM	Gain Margin
PM	Phase Margin
VFF	Velocity Feed Forward
RPM	Rounds Per Minute
PF	Pressure Feedback
HPPF	High-Pass Filtered Pressure Feedback
OS	Overshot
AHI	Active Holding Input
FF	Feed Forward
FFF	Flow Feed Forward
PFF	Pressure Feed Forward

Contents

1 Introduction

Hydraulic, linear actuators are widely used in the industry because of their capability to handle high loads and their robustness. However, normally linear actuators are controlled by a servo valve, and this leads to undesired power losses due to pressure drop across the valve.

An energy analysis of fluid power systems shows that approximately 35% of the input energy is consumed by control valves [16]. Due to the poor efficiency of the hydraulic system then there is a need to install a high amount of power. Furthermore, because of the poor efficiency a lot of heat is generated during the operation of the system, and overheat could cause breakdown of the machinery (because the viscosity of the oil depends on the temperature). The heat generation also leads to additional cooling, and this increases the overall cost of the system [16].
For these reasons, the focus of this master thesis is to develop accurate position control for a linear actuator without the use of servo valves in order to increase the efficiency of the hydraulic system.

The overall idea to increase the efficiency of the hydraulic system is to omit the servo valves, and instead control the position of the linear actuator by the pump speed. This idea is not a new idea, because the air craft industry has used electro-hydraulic compact drives since the 1990's. However, in the aircraft industry the linear actuator is a double rod cylinder, and this requires a high amount of installation space [10].
It is desired to decrease the amount of installation space needed because this can lead to a lower amount of installation cost. Thus it is desirable to develop position control for a single rod cylinder. However, a challenge with position control for an asymmetrical cylinder is the unequal amount of flow into the cylinder compared to the flow out of the cylinder [10].

At the University of Agder an experimental setup has been built where position control for a pump controlled asymmetrical cylinder can be tested. Therefore the goal of this master thesis is to develop accurate position control for the experimental setup seen in figure 1.1.
In order to further increase the efficiency of the system, the experimental setup is also capable of static load holding of the crane boom by closing 2 pilot operated check valves. During the static load holding, the motor does not have to compensate for leakage across the pump, and hereby the ballast stack seen in figure 1.1 can be held in a specific position without the use of energy.
However, undesired pressure spikes after the static load holding occur (This is further explained in section 2.4). Therefore, an additional goal of the project is to develop a pressure controller in order to smoothen the operation of the static load holding of the crane boom.

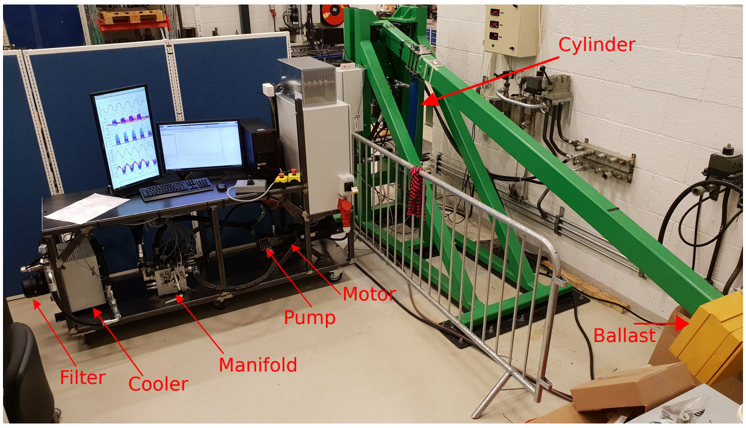

Figure 1.1: *Photograph of the experimental setup.*

2 | System Description

2.1 Mechanical Introduction

The mechanical part of the experimental setup can be seen in figure 2.1. In appendix B a mechanical analysis of the experimental setup has been conducted. In the following the most important results from the analysis are presented.

$$\begin{aligned} M_{Beam} &= 82\ kg \\ M_{Ballast} &= 320\ kg \\ I_{Tot} &= 4251\ kg\ m^2 \end{aligned} \tag{2.1}$$

M_{Beam}	Mass of beam [kg]
M_{Stack}	Mass of ballast stack [kg]
I_{Tot}	Mass moment of inertia for both the beam and ballast stack [kg·m^2]

Furthermore, the minimum length of the cylinder is 0.722 meters, and the stroke length is 0.5 meter. Hereby the ballast stack can be moved a total of 52.8 degrees up and down.

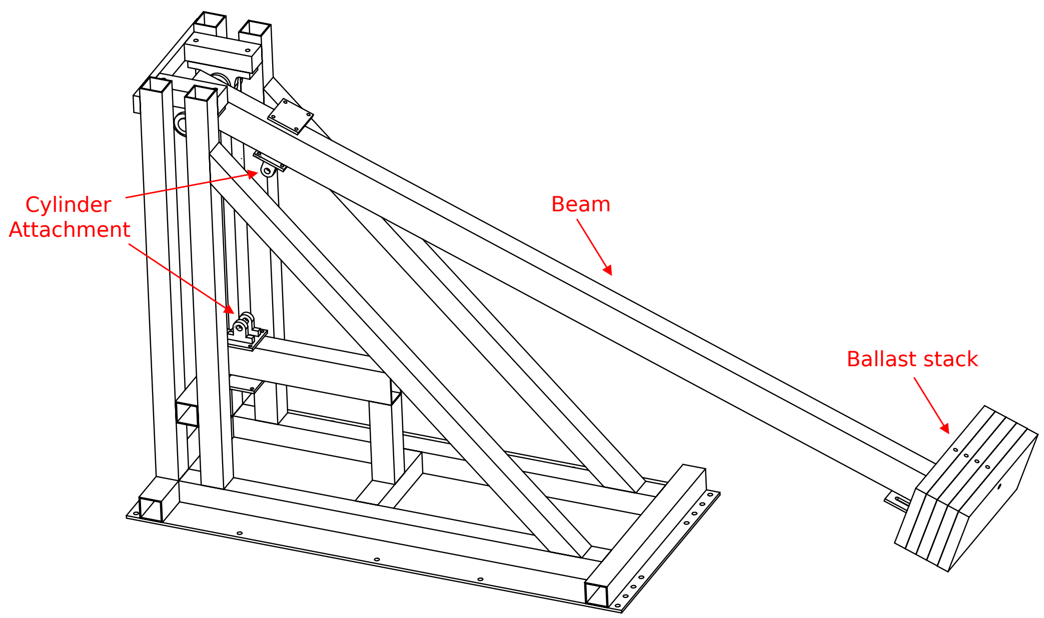

Figure 2.1: Sketch of the mechanical setup.

2.2 Introduction to Hydraulic System

The hydraulic diagram for the system can be seen in figure 2.2 and in table 2.1 a description of the different components can be seen. Furthermore, in appendix C an entire overview of the measured signals can be found.

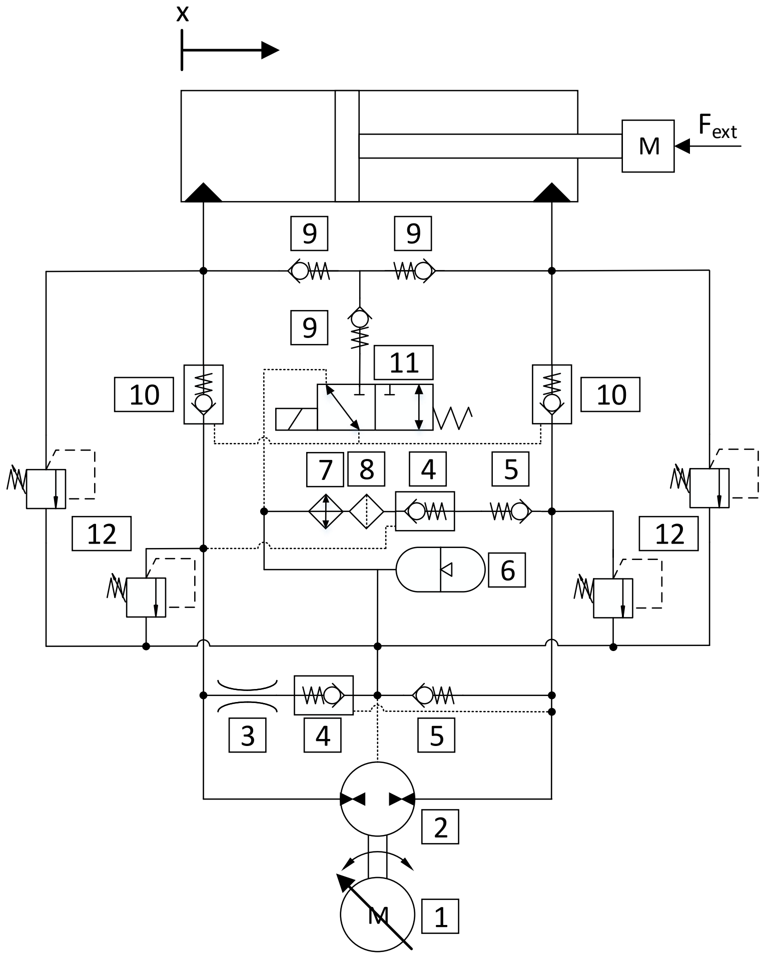

Figure 2.2: Overview of the hydrualic system.

Number	Description of the component
1	Electrical motor, drive and controller - Bosch Rexroth: IndraDyn S MSK071E-0300 [13]
2	Axial piston pump - Bosch Rexroth: A10FZG010/10W-V [3]
3	Throttle valve
4	Pilot operated check valve - SunHydraulics: CKEBXCN [14]
5	Check valve - Hawe Hydraulics: RK4 [6]
6	Accumulator - Bosch Rexroth: HAB10-330-60/0G09G-2N111-CE [4]
7	Oil cooler
8	Oil filter - Bosch Rexroth: 50LEN0 [5]
9	Check valve - Hawe Hydraulics: RB2 [6]
10	Pilot operated check valve - SunHydraulics: CVEVXFN [15]
11	Electrically actuated 3/2-way directional valve - Argo Hytos: SD1E-A3/H2S8M8 [7]
12	Pressure relief valve: 200 bar cracking pressure

Table 2.1: Explanation of the hydraulic components.

From figure 2.2 it can be difficult to understand the working principle of the hydraulic setup. Therefore a simpler drawing has been made, and it can be seen in figure 2.3.

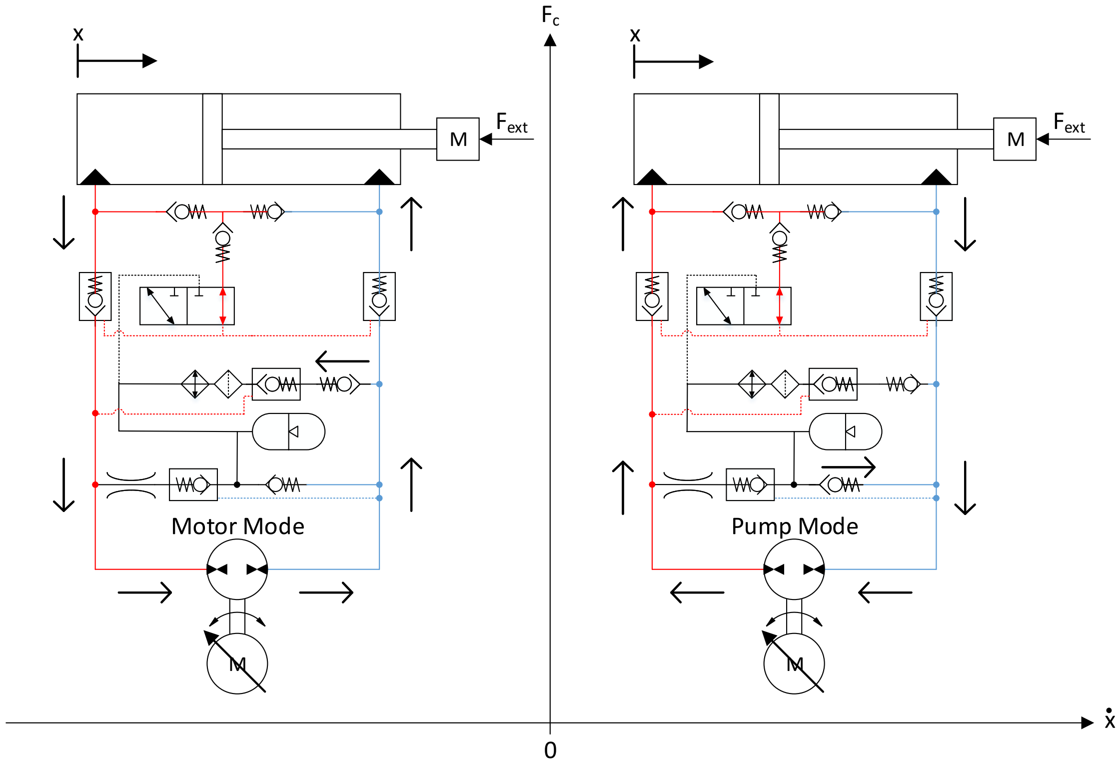

Figure 2.3: Working principle (Pressure relief valves not included).

Based on figure 2.3 it can be seen that the system can operate under two different scenarios. Either the cylinder is retracted or the cylinder is extracted.
If the cylinder is retracted then it can be seen that F_{ext} works in the same direction as the velocity of the piston. During this operation mode the system is capable of saving energy because the high pressure (red lines) is used to drive the pump. In this scenario the pump drives the motor, and hereby energy can be harvested from the system. Furthermore, during retraction the accumulator receives oil because of the area ratio between the piston side and the rod side.
If the cylinder is extracted then it can be seen that F_{ext} works in the opposite direction of the the velocity. During this operation mode energy the motor drives the pump, and energy has to be delivered to the system. Furthermore, during extrusion the accumulator delivers oil to the high pressure side because of the area ratio between the piston side and the rod side.

From figure 2.3 it is concluded that some check are always opened and some check valves are not opened at any time during operation. Therefore it is decided to simplify the hydraulic setup in order to ease the modelling of the system.

2.3 System Simplification

The simplified hydraulic diagram can be seen in figure 2.4.

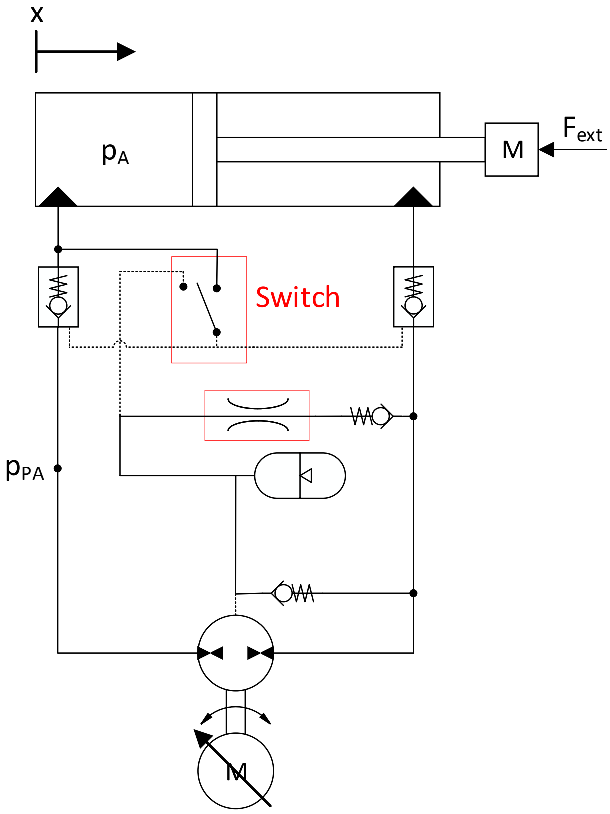

Figure 2.4: Simplified hydraulics.

It can be seen that the oil filter, oil cooler and a pilot operated check valve (number 4) have been approximated as an orifice. This simplification is based on that the pilot operated check valve is always open.
Furhermore, the 3/2-way direction valve, and the 3 check valves (number 9) are simplified to a switch which opens and closes the pilot operated check valves (number 10).
Based on figure 2.3 it can furthermore be concluded that no flow is present through the throttle valve (number 3) and a pilot operated check valve. Therefore these 2 components are neglected.
Lastly, the pressure relief valves are also neglected because no flow is present through them during normal operation.

2.4 Challenge with Static Load Holding

In chapter 1 (Introduction) it is stated that undesired pressure oscillations occur after the static load holding. In this section these pressure oscillations are shown by an open loop experiment, and a solution is presented.
In the experiment a reference velocity is given to the motor, and the reference and the measured motor velocity are seen in figure 2.5. It can be seen that the POCV's are closed after 47 seconds and reopened after 117 seconds. During this time interval the static load holding is activated. This means that the cylinder pressure in chamber A (p_A) is kept constant while the pump pressure on the A side (p_{PA}) is decreasing due to leakage across the pump. This can be seen in figure 2.6.

Furthermore, in figure 2.6 the pressure oscillations can be seen after the static load holding.

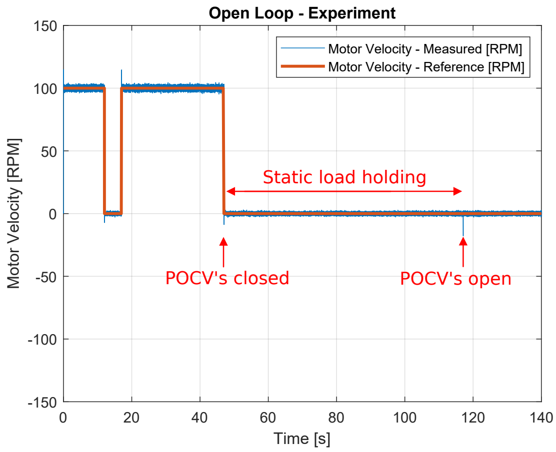

Figure 2.5: Motor velocity.

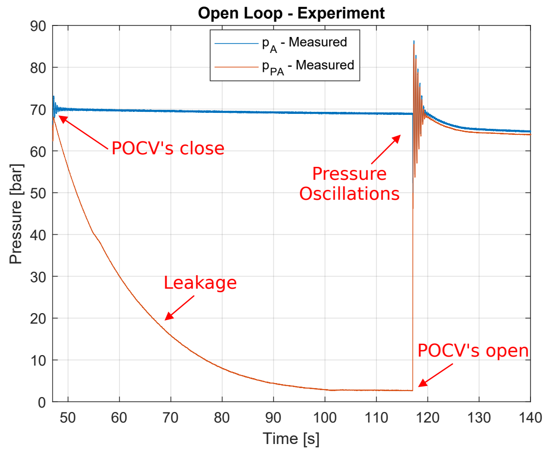

Figure 2.6: Measured pressure.

In figure 2.7 the measured cylinder position can be seen during the experiment. After 117 seconds it can be see that the position drops and in figure 2.8 it can be seen that the position drop is approximately 2.2 mm.

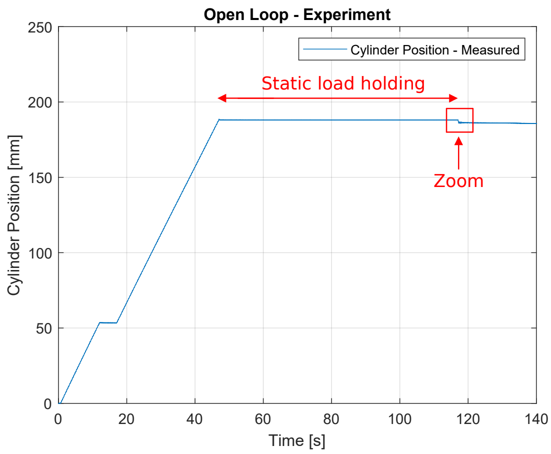

Figure 2.7: Measured cylinder position.

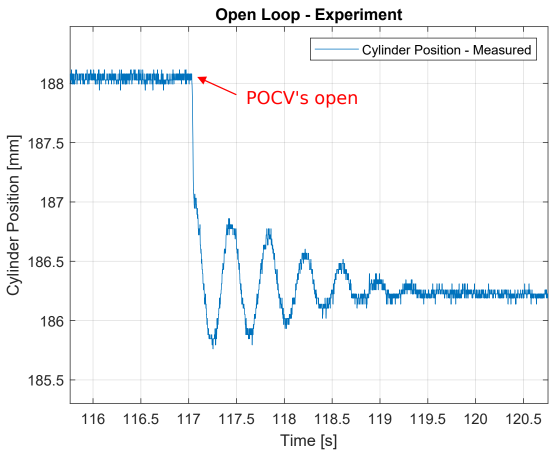

Figure 2.8: Measured cylinder position (Zoom).

It is desired to decrease the oscillations, and a solution could be to design a pressure controller such that the pressure p_{PA} can be build up before the POCV's are opened.

3 | Problem Statement

As mentioned in the introduction then the main goal of this project is to develop and test different control strategies for position control. Therefore the following main research question has been developed.

> ***"How can different control strategies be designed and tested at the experimental setup such that a given trajectory is followed accurately?"***

5 sub-questions have been developed based on the main research question. These outline the major parts of the project.

- How can an accurate nonlinear model be developed?
- How can the model be validated?
- How can the model be linearised?
- How should the controllers be designed?
- How can the designed controllers be implemented in the experimental setup?

Demands

Several demands have been developed such that the final design fulfils the requirements. The demands are separated into hard demands and soft demands.

Hard demands - Hard demands must be met.

- The average error during the trajectory must not be higher than 1mm.
- The maximum deviation from the trajectory must not be higher than 10mm.
- The position drop after the re-opening of the POCV's must be below 1mm.

Soft demands - Soft demands are preferable to meet.

- The pressure oscillations after the re-opening of the POCV's should be reduced.

Delimitation

The delimitation of this project is an important factor, because this master thesis is 1 month shorter compared to a normal time scale at Aalborg University. Therefore, in order to secure that the main goal of this project is fulfilled then some delimitations must be applied.
It is decided to approximate the motor as a second order system. This decision is based on the work done by a previous project group [11], and the project group showed that the motor dynamics could be described by a second order system.

4 Nonlinear Model

In figure 4.1 a block diagram representation of the model can be seen. The inputs and outputs for each of the sub-models are shown in order to give an understanding of the structure of the nonlinear model. The control structure is not described in this chapter, but it is included in order to show the overall structure of the model.
The chapter is divided into 3 sections, where the 3 sections describe the 3 sub-models (Motor and Drive Model, Hydraulic Model and Mechanical Model).

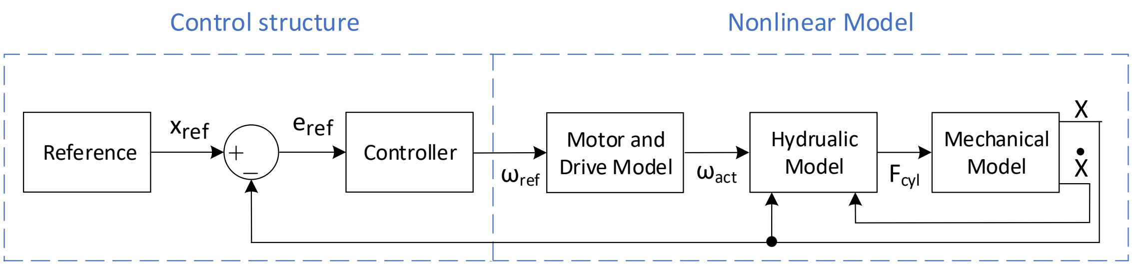

Figure 4.1: Block diagram representation of the nonlinear model.

4.1 Motor and Drive Model

It is decided to approximate the motor and drive as a second order system. This decision is based on the work of a previous project group [11]. The second order system is seen in equation 4.1.

$$\frac{\omega_{act}}{\omega_{ref}} = \frac{\omega_{n,m}^2}{s^2 + 2 \cdot \zeta_m \cdot \omega_{n,m} \cdot s + \omega_{n,m}^2} \tag{4.1}$$

ω_{act}	Actual speed of the motor [rad/s]
ω_{ref}	Reference speed for the motor [rad/s]
$\omega_{n,m}$	Eigenfrequency of the motor [rad/s]
ζ_m	Damping coefficient for the motor [-]

Equation 4.1 is now transformed to the time domain.

$$\ddot{\omega}_{act} + 2 \cdot \zeta_m \cdot \omega_{n,m} \cdot \dot{\omega}_{act} + \omega_{act} \cdot \omega_{n,m}^2 = \omega_{n,m}^2 \cdot \omega_{ref} \tag{4.2}$$

Isolating for $\ddot{\omega}_{act}$ yields:

$$\begin{aligned} \ddot{\omega}_{act} &= \omega_{n,m}^2 \cdot \omega_{ref} - 2 \cdot \zeta_m \cdot \omega_{n,m} \cdot \dot{\omega}_{act} - \omega_{act} \cdot \omega_{n,m}^2 \\ \ddot{\omega}_{act} &= \omega_{n,m}^2 \cdot (\omega_{ref} - \omega_{act}) - 2 \cdot \zeta_m \cdot \omega_{n,m} \cdot \dot{\omega}_{act} \end{aligned} \tag{4.3}$$

The implementation of the motor model can be seen in figure 4.2.

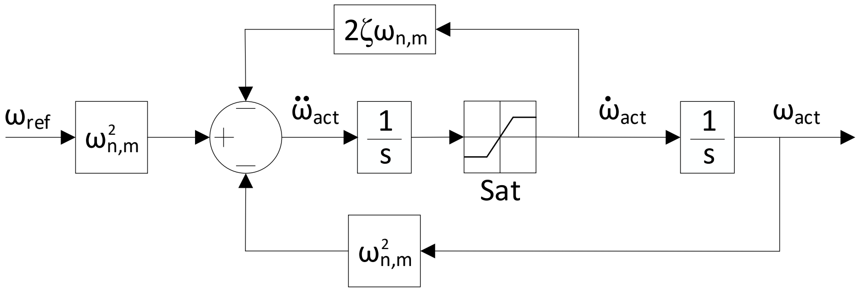

Figure 4.2: Block diagram representation of the motor model.

The coefficients for the motor model and the saturation limit are based on [11], and the coefficients are given below.

$$\begin{aligned} \omega_{n,m} &= 754 rad/s \\ \zeta_m &= 0.5 \\ Saturation &= 9948 \end{aligned} \tag{4.4}$$

4.2 Hydraulic Model

The input for the hydraulic model is the motor speed (ω_{act}) and the output is the cylinder force (F_{cyl}). In figure 4.3 an overview of all the flow directions can be seen. Furthermore, this figure shows all the pressure nodes, and it is used as the reference figure for all definitions in this section.
The hydraulic model consists of the following components:

- Pump Model
- Check Valve Model
- Pilot Operated Check Valve Model (Appendix D)
- Orifice Model (Appendix D)
- Accumulator Model
- Cylinder Model

It is decided to move the model of the POCV's and the orifice to appendix D because the model procedure is similar to the check valve model.

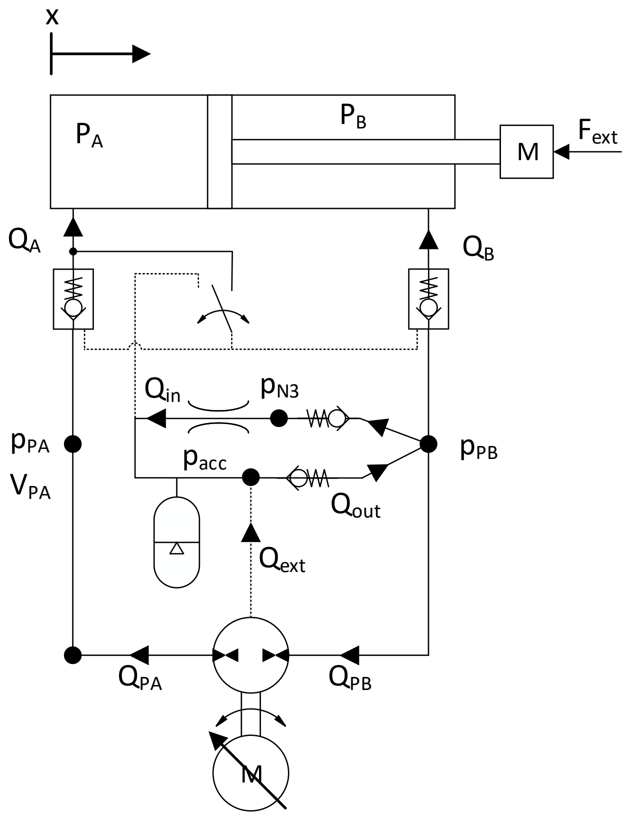

Figure 4.3: Schematic used to define flow directions and pressure nodes.

4.2.1 Pump Model

The input for the pump model is ω_{act}, and the outputs are the pump flows (Q_{PA}, Q_{PB} and Q_{ext}). The pump model is modelled as seen in the equations below, and the directions of the flows are seen in figure 4.4.

$$\left.\begin{aligned}
Q_{PA} &= K_V \cdot \omega_{act} - Q_{ext,A} - Q_{int} \\
Q_{PB} &= K_V \cdot \omega_{act} - Q_{ext,B} + Q_{int} \\
Q_{ext,A} &= K_{L,ext} \cdot (p_{PA} - p_{acc}) \\
Q_{ext,B} &= K_{L,ext} \cdot (p_{PB} - p_{acc}) \\
Q_{ext} &= Q_{ext,A} + Q_{ext,B} \\
Q_{int} &= K_{L,int} \cdot (p_{PA} - p_{PB})
\end{aligned}\right\} p_{PA} \geq p_{PB}$$

$$\left.\begin{aligned}
Q_{PA} &= K_V \cdot \omega_{act} - Q_{ext,A} + Q_{int} \\
Q_{PB} &= K_V \cdot \omega_{act} - Q_{ext,B} - Q_{int} \\
Q_{ext,A} &= K_{L,ext} \cdot (p_{PA} - p_{acc}) \\
Q_{ext,B} &= K_{L,ext} \cdot (p_{PB} - p_{acc}) \\
Q_{ext} &= Q_{ext,A} + Q_{ext,B} \\
Q_{int} &= K_{L,int} \cdot (p_{PA} - p_{PB})
\end{aligned}\right\} p_{PA} < p_{PB}$$

Q_{PA}	Pump flow delivered to the A-side [m^3/s]
Q_{PB}	Pump flow delivered to the B-side [m^3/s]
Q_{ext}	External leakage delivered to the accumulator [m^3/s]
Q_{int}	Internal leakage in the pump [m^3/s]
K_V	Displacement coefficient [m^3/rad]
$K_{L,i}$	Leakage coefficient [m^3/(Pa s)]

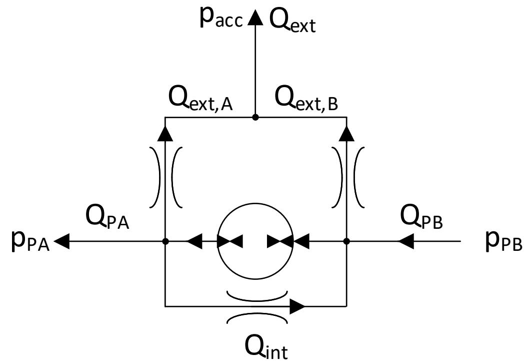

Figure 4.4: This figure shows the directions of the pump flows.

It is assumed that the leakage flow is laminar and proportional to the pressure differences. The constant K_V is determined from the datasheet. In the datasheet the displacement, geometric constant V_g is given [3].

$$V_g = \frac{10.6\ cm^3}{\text{rev}} \tag{4.5}$$

Hereby K_V is defined to be as in equation 4.6.

$$K_V = \frac{V_g}{2 \cdot \pi} \tag{4.6}$$

It should be mentioned that the constant V_g has been changed to a slightly lower value than seen in equation 4.5. The reason for this is that not all the oil is pumped into the system (the volumetric efficiency is not 100%).

4.2.2 Check Valves

The flows through the check valves with number 5 (see figure 2.2) are modelled by equation 4.7.

$$Q_{cv} = \frac{Q_{cv,n}}{\Delta p_{cv,n}} \cdot x_{cv,n} \cdot \sqrt{\Delta p_{cv}} \cdot sign(\Delta p_{cv}) \tag{4.7}$$

With the flow direction as defined as in figure 4.5, and Δp_{cv} given by equation 4.8.

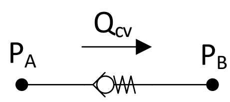

Figure 4.5: This figure shows the flow direction.

$$\Delta p_{cv} = p_A - p_B \tag{4.8}$$

$x_{cv,n}$ is the normalised opening, and it is is given by equation 4.9.

$$x_{cv,n} = \begin{cases} 0 & \Delta p_{cv} < p_{cv,cp} \\ \frac{\Delta p_{cv} - p_{cv,cp}}{p_{cv,cpe} - p_{cv,cp}} & p_{cv,cp} < \Delta p_{cv} < p_{cv,cpe} \\ 1 & \Delta p_{cv} > p_{cv,cpe} \end{cases} \tag{4.9}$$

Q_{cv}	Flow through the check valve [m^3/s]
$Q_{cv,n}$	Nominal flow through the check valve at nominal pressure [m^3/s]
$p_{cv,n}$	Nominal pressure [Pa]
Δp_{cv}	Pressure difference across the valve [Pa]
$x_{cv,n}$	Normalised valve opening (Between 0 and 1) [-]
$p_{cv,cp}$	Check valve crack pressure (Defines when the valve is beginning to open.)[Pa]
$p_{cv,cpe}$	Check valve crack pressure end (Defines when the valve is fully open.) [Pa]

In figure 4.6 a comparison between data points from the datasheet and the approximation is seen. It is decided that the approximation describes the flow characteristic accurately enough for being used in the Simulink model.

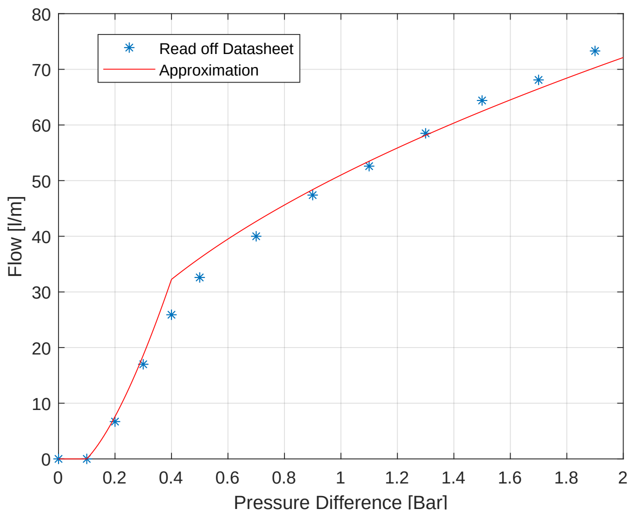

Figure 4.6: A comparison between data points and the approximated flow.

In the table below a summery of the constants can be seen.

Name	$p_{cv,cp}$	$p_{cv,cpe}$	$Q_{cv,n}$	$\Delta p_{cv,n}$
CV5	0.1 [bar]	0.4 [bar]	51 [l/min]	[1 bar]

4.2.3 Accumulator Model

In figure 4.7 a schematic of a bladder accumulator is seen. The purpose of this subsection is to describe the pressure dynamics of the accumulator.

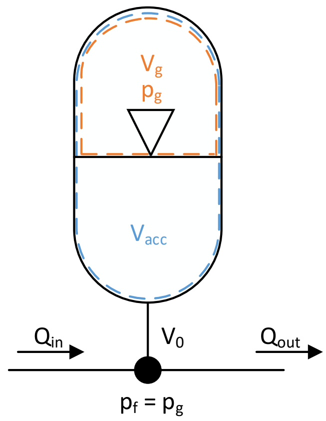

Figure 4.7: *Schematic of a bladder accumulator.*

The friction and the bladder mass is neglected, and thus the gas pressure p_g is equal to the fluid pressure p_f.

$$p_f = p_g \tag{4.10}$$

The continuity equation is applied on the accumulator and the is seen in equation 4.11.

$$(Q_{in} - Q_{out}) = \dot{V}_f + \dot{p}\frac{V_f}{\beta_{eff}} \tag{4.11}$$

Next $\dot{p}$ is isolated:

$$\begin{aligned} \dot{p} &= (Q_{in} - Q_{out} - \dot{V}_f) \cdot \frac{\beta_{eff}}{V_f} \\ \dot{p} &= (Q_{in} - Q_{out} + \dot{V}_g) \cdot \frac{\beta_{eff}}{V_{acc} + V_0 - V_g} \end{aligned} \tag{4.12}$$

$\dot{p}_g$ can be can be calculated based on differentiation and the ideal adiabatic gas law seen in equation 4.13 .

$$p_g \cdot V_g^{\gamma} = const. \tag{4.13}$$

γ	Gas constant for N_2 [-]

$$\frac{d}{dt}(p_g \cdot V_g^{\gamma}) = \frac{d}{dt}(const.) \tag{4.14}$$

Applying the product rule on equation 4.14 yields equation 4.15.

$$\dot{p}_g \cdot V_g^{\gamma} + p_g \cdot \frac{d}{dt}(V_g^{\gamma}) = 0 \tag{4.15}$$

$$\dot{p}_g \cdot V_g^{\gamma} + p_g \cdot (\gamma \cdot V_g^{\gamma-1} \cdot \dot{V}_g) = 0 \tag{4.16}$$

$$\dot{p}_g \cdot V_g^{\gamma} + p_g \cdot \frac{\gamma \cdot V_g^{\gamma} \cdot \dot{V}_g}{V_g} = 0 \tag{4.17}$$

Now $\dot{V}_g$ is isolated:

$$p_g \cdot \frac{\gamma \cdot V_g^{\gamma} \cdot \dot{V}_g}{V_g} = -\dot{p}_g \cdot V_g^{\gamma} \tag{4.18}$$

$$\dot{V}_g = -\frac{\dot{p}_g \cdot V_g^{\gamma} \cdot V_g}{p_g \cdot \gamma \cdot V_g^{\gamma}} \tag{4.19}$$

$$\dot{V}_g = -\frac{1}{\gamma} \cdot \frac{V_g}{p_g} \cdot \dot{p}_g \tag{4.20}$$

V_g is calculated using equation 4.21.

$$V_g = \begin{cases} V_{acc} & p < p_0 \\ V_{acc} \cdot \left(\frac{p_0}{p}\right)^{\frac{1}{\gamma}} & p \geq p_0 \end{cases} \tag{4.21}$$

p_0	Precharge pressure for the accumulator [Pa]

Now the expression for the pressure dynamics can be expressed. Equation 4.20 is inserted in equation 4.12 (with $p = p_g = p_f$).

$$\begin{aligned} \dot{p} &= (Q_{in} - Q_{out} - \frac{1}{\gamma} \cdot \frac{V_g}{p} \cdot \dot{p}) \cdot \frac{\beta_{eff}}{V_{acc} + V_0 - V_g} \\ \dot{p} &= (Q_{in} - Q_{out}) \cdot \frac{1}{\frac{V_{acc}+V_0-V_g}{\beta_{eff}} + \frac{1}{\gamma} \cdot \frac{V_g}{p}} \end{aligned} \tag{4.22}$$

4.2.4 Cylinder Model

In figure 4.8 a schematic of an asymmetrical cylinder is seen.

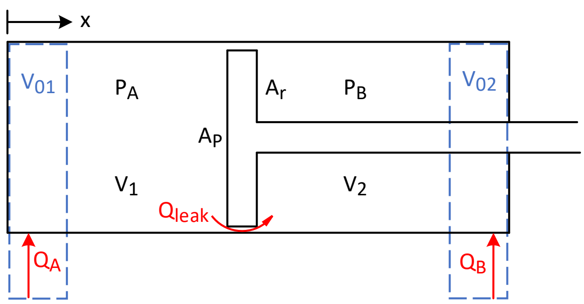

Figure 4.8: *Schematic of an asymmetrical cylinder.*

The continuity equation is used to describe the pressure dynamics, and it is given by equation 4.23.

$$Q_{in} - Q_{out} = \dot{V} + \frac{V}{\beta_{eff}}\dot{p} \tag{4.23}$$

Now the continuity equation is applied at figure 4.8.

$$Q_A - Q_{leak} = A_p\dot{x} + \frac{A_p x + V_{01}}{\beta_{eff}}\dot{p}_A \tag{4.24}$$

$$Q_B + Q_{leak} = -A_p\dot{x} + \frac{A_r(L_c - x) + V_{02}}{\beta_{eff}}\dot{p}_B \tag{4.25}$$

Q_{leak}	Leakage flow [m^3/s]
x	Cylinder position [m]
V_{0i}	Constant volume [m^3]
L_c	Maximum stroke length of the cylinder [m]
β_{eff}	Effective stiffness of the oil [Pa]

The flow Q_{leak} could be modelled as a laminar flow and proportional to the pressure drop across the valve. However, it is decided to neglect Q_{leak} because it is assumed small compared to Q_A and Q_B.

The effective stiffness of the oil is not a constant, because the oil contains a small amount of air. The stiffness of air is much less compared to the stiffness of oil, and thus a small amount of air has an influence of β_{eff} [1].

$$\beta_{eff} = \frac{1}{\frac{1}{\beta_{oil}} + \frac{\varepsilon_{air}}{c_{ad} \cdot pa}} \tag{4.26}$$

β_{oil}	Stiffness of pure oil [Pa]
ε_{air}	The volumetric ratio of free air in the fluid [-]
c_{ad}	Adiabatic constant of air [-]
p_a	Absolute pressure [Pa]

The equation for β_{eff} is implemented in the nonlinear model, and a saturation limit at 10000 bar is added [1].

Next $\dot{p}_A$ and $\dot{p}_B$ are isolated in equation 4.27.

$$\begin{aligned} \dot{p}_A &= (Q_A - A_p\dot{x}) \cdot \frac{\beta_{eff}}{A_p x + V_{01}} \\ \dot{p}_B &= (Q_B + A_r\dot{x}) \cdot \frac{\beta_{eff}}{A_r \cdot (L_c - x) + V_{02}} \end{aligned} \tag{4.27}$$

The cylinder force can be calculated by equation 4.28.

$$F_{cyl} = p_A \cdot A_p - p_B \cdot A_r \tag{4.28}$$

A block diagram representation of the cylinder model can be seen in figure 4.9.

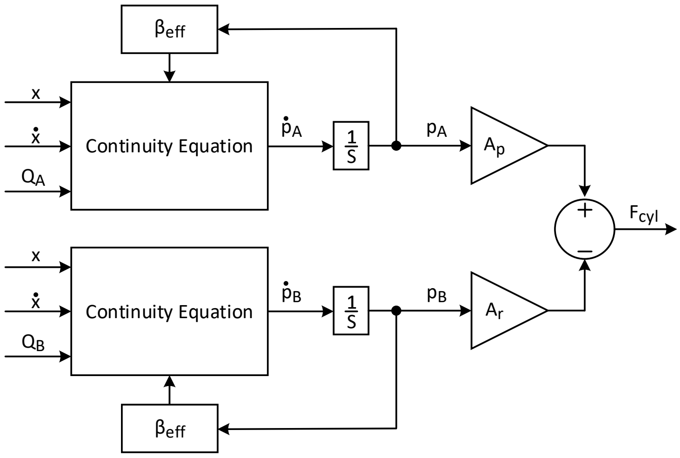

Figure 4.9: *Block diagram representation of the cylinder model.*

4.3 Mechanical Model

In figure 4.10 the block diagram representation of the mechanical model can be seen. The input for the mechanical model is the cylinder force (F_{cyl}), and the output is the cylinder velocity and position. This section is divided into the following subsections:

- Force-Torque Relation
- Friction Torque
- Geometry (θ_1, θ_2)
- Euler-Lagrange
- Geometry (Angular-Linear Relation)

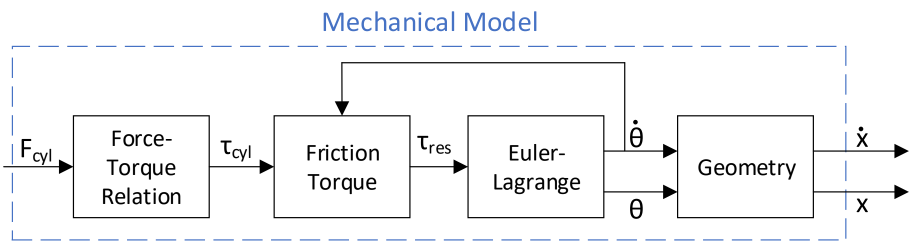

Figure 4.10: *Block diagram representation of the cylinder model.*

4.3.1 Force-Torque Relation

The force from the cylinder results in a torque delivered by the cylinder, and this torque is given by equation 4.29.

$$\tau_c = F_{cyl} \cdot |AC| \cdot sin(\theta_\tau) \tag{4.29}$$

Based on figure 4.11 then θ_τ is given by

$$\theta_\tau = cos^{-1}\left(\frac{|BC|^2 + |AC|^2 - |AB|^2}{2 \cdot |BC| \cdot |AC|}\right) \tag{4.30}$$

|BC| is calculated by the minimum length of the cylinder and the cylinder position.

$$|BC| = |BC_{min}| + x \tag{4.31}$$

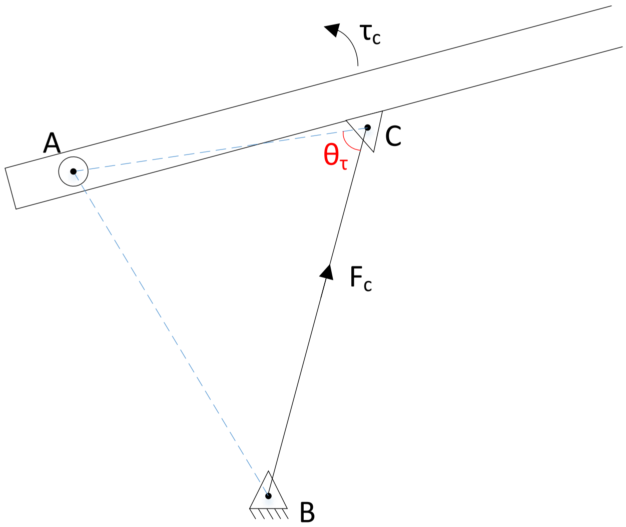

Figure 4.11: This figure shows the angle used to calculate the torque-force relation.

4.3.2 Friction Torque

The friction torque is modelled as a coulomb friction and a viscous friction as seen in figure 4.12.

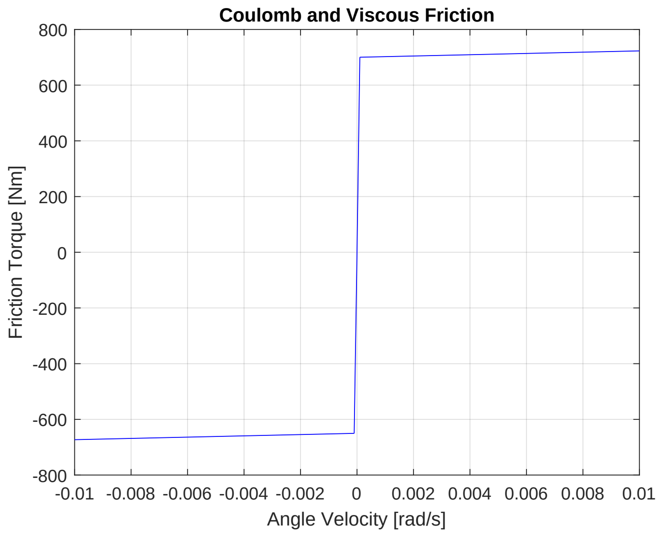

Figure 4.12: *Graph showing the coulomb and viscous friction torque for different* $\dot{\theta}_1$*.*

As it can be seen in figure 4.12 then a steep slope has been implemented for $\dot{\theta}_1$ close to 0 rad/s. The reason for this is to ease the simulation for low angular velocities. The implementation of the friction torque can be seen in equation 4.32.

$$\tau_{fric} = \begin{cases} -\tau_{couN} + B_{\omega N} \cdot \dot{\theta}_1 & \dot{\theta}_1 \leq -\dot{\theta}_{thres} \\ \frac{\tau_{couN} + B_{\omega N} \cdot \dot{\theta}_{thres}}{\dot{\theta}_{thres}} \cdot \dot{\theta}_1 & -\dot{\theta}_{thres} < \dot{\theta}_1 < 0 \\ \frac{\tau_{couP} + B_{\omega P} \cdot \dot{\theta}_{thres}}{\dot{\theta}_{thres}} \cdot \dot{\theta}_1 & 0 < \dot{\theta}_1 < \dot{\theta}_{thres} \\ \tau_{couP} + B_{\omega P} \cdot \dot{\theta}_1 & \dot{\theta}_{thres} \leq \dot{\theta}_1 \end{cases} \tag{4.32}$$

τ_{couN}	Coulomb friction for negative velocity [Nm]
$B_{\omega N}$	Viscous friction coefficient for negative velocity [Nm s]
τ_{couP}	Coulomb friction for positive velocity [Nm]
$B_{\omega P}$	Viscous friction coefficient for positive velocity [Nm s]
$\dot{\theta}_{thres}$	Threshold velocity [rad/s]

It should be noted that the friction torque is calculated based only at $\dot{\theta}_1$. However, in reality the friction torque depends both on the angular velocity ($\dot{\theta}_1$) and the linear velocity ($\dot{x}$).

4.3.3 Geometry (θ_1, θ_2)

In order to apply the Euler-Lagrange equation on the system, then θ_1 has to be defined, and θ_1 is seen in figure 4.13.

$$\theta_1 = cos^{-1}\left(\frac{|AB|^2 + |AC|^2 - |BC|^2}{2 \cdot |AB| \cdot |AC|}\right) - \alpha_2 + \alpha_1 \tag{4.33}$$

The expressions for the constant angles α_1 and α_2 are seen in equation 4.34.

$$\alpha_1 = tan^{-1}\left(\frac{|AC_y|}{|AC_x|}\right) \quad , \quad \alpha_2 = tan^{-1}\left(\frac{|AB_y|}{|AB_x|}\right) \tag{4.34}$$

θ_2 is also defined in figure 4.13. θ_2 is used in the Euler-Lagrange equations because during movement of the beam it has been observed that during acceleration the beam oscillates. The oscillations causes pressure fluctuations, and in order to include these pressure fluctuations in the simulations then a torsion spring is included in the simulation. It should be noted that by implementing a torsion spring then the beam is split into two different components. An analysis of the mass moment of inertia can be found in appendix B.

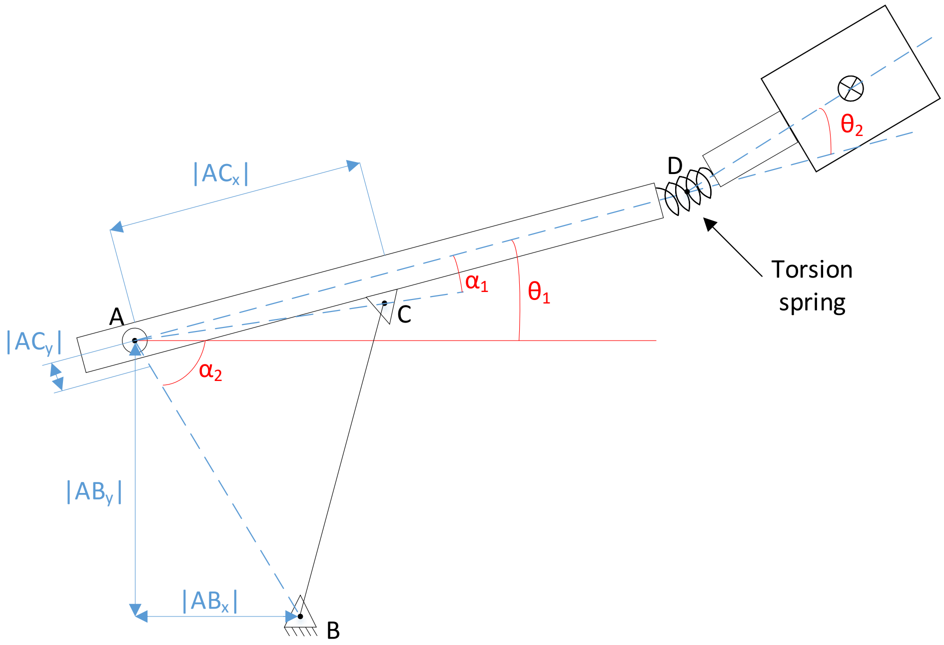

Figure 4.13: Defined angles and lengths - The angle θ_2 is exaggerated

4.3.4 Euler-Lagrange

In this subsection a summary of appendix E is presented, and only the results from the Euler-Lagrange equations are presented. The rest of the calculations can be found in appendix E.
The dynamics of the crane is described by the Euler-Lagrange equation and the equation is seen in equation 4.35 [9].

$$\frac{d}{dt}\frac{\partial \mathcal{L}}{\partial \dot{\underline{\theta}}} - \frac{\partial \mathcal{L}}{\partial \underline{\theta}} = \underline{\tau} \tag{4.35}$$

For a 2-DOF system then the following is defined:

$$\underline{\theta} = \begin{bmatrix} \theta_1 \\ \theta_2 \end{bmatrix} \quad , \quad \dot{\underline{\theta}} = \begin{bmatrix} \dot{\theta}_1 \\ \dot{\theta}_2 \end{bmatrix} \tag{4.36}$$

Derived from equation 4.35 the dynamics of the system can be described by equation 4.37.

$$\ddot{\underline{\theta}} = \underline{\underline{D}}^{-1}(\underline{\theta})[\underline{\tau} - \underline{C}(\underline{\theta}, \dot{\underline{\theta}}) - \underline{\phi}(\underline{\theta})] \tag{4.37}$$

With $\underline{\tau}$ seen in equation 4.38.

$$\underline{\tau} = \begin{bmatrix} F_{cyl} \cdot |AC| \cdot sin(\theta_\tau) \\ 0 \end{bmatrix} \tag{4.38}$$

The block diagram representation can be seen in figure 4.14.

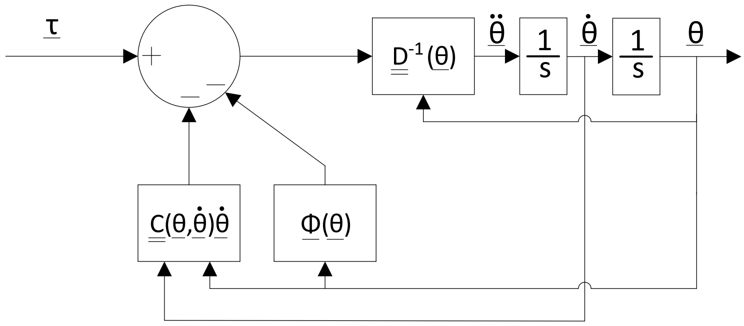

Figure 4.14: Block diagram of the implementation of the Euler Lagrange equations.

4.3.5 Geometry (Angular-Linear Relation)

The output from the Euler-Langrange equations are the angular accelerations, angular velocities and angular positions. These angular outputs are transformed into linear velocities and positions by the following equations.

$$x = \sqrt{(-cos(\theta_1 - \alpha_1 + \alpha_2)) \cdot 2 \cdot |AB| \cdot |AC| + |AB|^2 + |AC|^2} - |BC|_{min} \tag{4.39}$$

In order to calculate the linear velocity of the cylinder the chain rule is applied to equation 4.39. The chain rule is seen in equation 4.40.

$$\dot{x} = \frac{dx}{dt} = \frac{dx}{d\theta_1} \cdot \frac{d\theta_1}{dt} \tag{4.40}$$

$$\dot{x} = \frac{-(sin(-\theta_1 + \alpha_1 - \alpha_2) \cdot |AB| \cdot |AC|)}{\sqrt{-2 \cdot cos(-\theta_1 + \alpha_1 - \alpha_2) \cdot |AB| \cdot |AC| + |AB|^2 + |AC|^2}} \cdot \dot{\theta}_1 \tag{4.41}$$

5 Validation

In order to validate the model then the motor has been given step-inputs for a speed reference. The input for the experimental setup can be seen in figure 5.1. An input reference for the motor speed at 50 RPM has been chosen because because it is a relative slow motor speed. Hereby the transient responses can be seen.

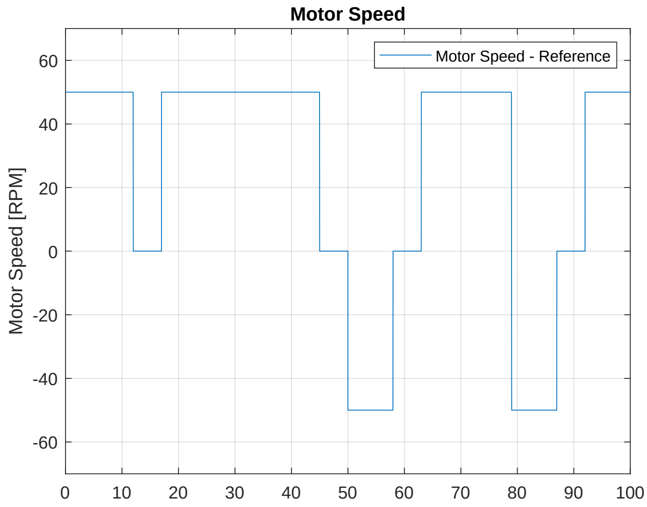

Figure 5.1: Reference for open loop input.

5.1 Motor Model Validation

In figure 5.2 and 5.3 the measured and simulated motor speed are seen. It can be seen that the simulated data corresponds well with the measured data.

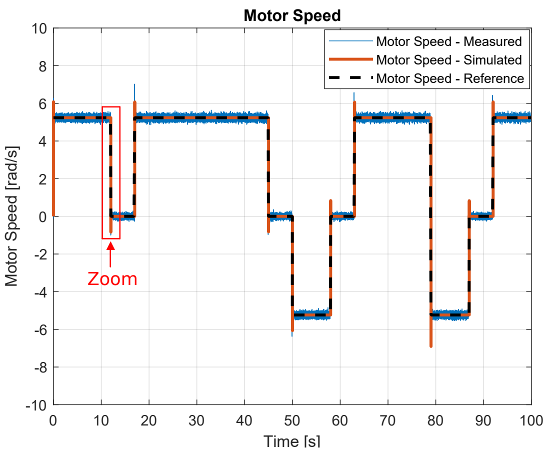

Figure 5.2: Measured data and simulation.

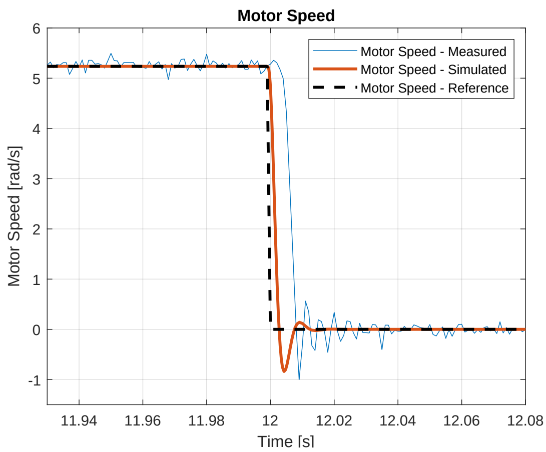

Figure 5.3: Measured data and simulation - Zoom.

Therefore it is concluded that the simplified motor and drive model (section 4.1) describes the dynamic behaviour of the motor accurately.
In figure 5.3 it can be seen that the measured motor speed is a bit slower and a bit delayed compared to the simulated data. A reason for this could be that the coefficients for the motor was found for a no load condition, and this could explain why the model is faster [11]. An additional reason could also be that a saturation limit for the current-build-up for the motor has been reached.

5.2 Leakage Coefficient

During the validation process of the model it has been found that the pump model (section 4.2) does not describe the leakage across the pump accurately.
The 4 time intervals seen in figure 5.4 are all time intervals where the motor speed is 0 rad/s, and the pressure difference across the pump is almost the same for the 4 time intervals. According to the pump model then the leakage across the pump should be the same for all time intervals. However, as it can be seen in figure 5.4 then this is not the case.
In equation 5.1 the leakage coefficients have been compared to the leakage coefficient for the 1^{st} time interval. It can be seen that the leakage coefficients vary a lot.

$$\begin{aligned} \frac{K_{L,Time\ Interval\ 2}}{K_{L,Time\ Interval\ 1}} &= 1.25 \\ \frac{K_{L,Time\ Interval\ 3}}{K_{L,Time\ Interval\ 1}} &= 1.98 \\ \frac{K_{L,Time\ Interval\ 4}}{K_{L,Time\ Interval\ 1}} &= 6.35 \end{aligned} \tag{5.1}$$

In the model the leakage across the pump is only a a function of the pressure difference. However, in this section it is shown that this is not the case for experimental setup. It is believed that the leakage across the pump is a function of both the pressure difference and the pump position. An explanation for this could be that the pump contains 9 pistons, and the leakage also depends on their position. This is further explained in appendix F.
In this project it is chosen to keep the leakage as a function of only the pressure difference. The reason for this is that a leakage model based both on the pressure difference and the pump position would be time consuming, and it would be beyond the scope of this project.

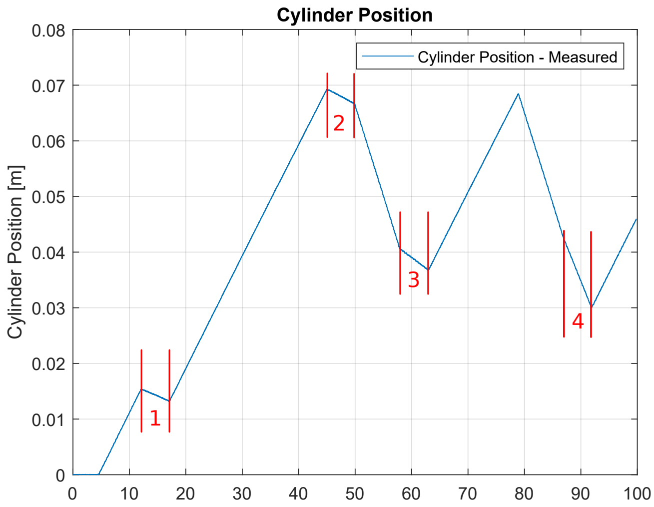

Figure 5.4: Determination of leakage coefficients for the pump.

5.3 Pressure and Position

As seen in figure 5.4 then the leakage coefficient for the 4^{th} time interval is significantly higher compared to the other intervals. Therefore it is chosen only to show the time interval for t = 0s to t = 85s for the pressures and the cylinder position. The reason for this that the cylinder position in the model is much higher compared to the measurements for t > 85s.

In figure 5.5 and in figure 5.6 the pressure for the accumulator and the pressure in chamber B is seen. It is seen that the simulated pressures correspond well with the measured data. However, it can be seen that pressure B in the cylinder is approximately 0.3 bar to low. This offset is small, and thus it is deemed acceptable.

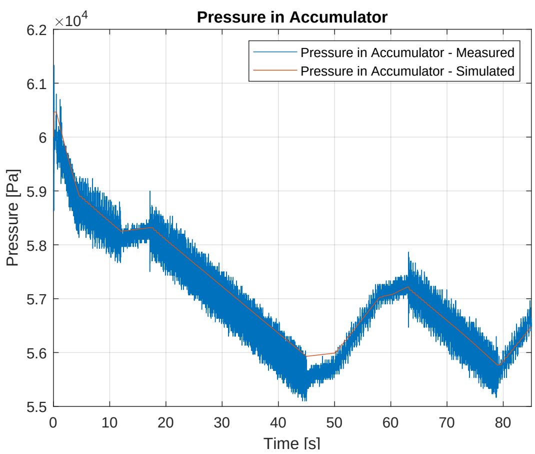

Figure 5.5: Accumulator pressure.

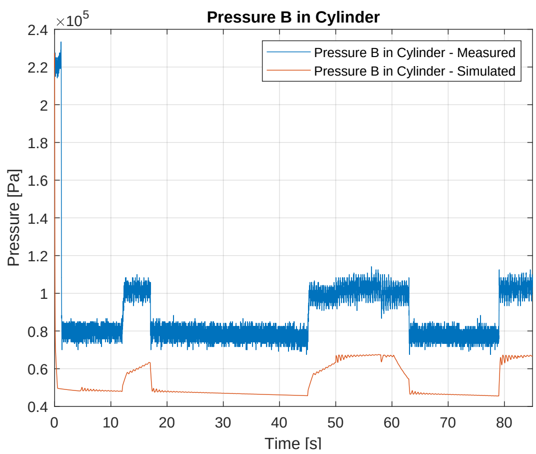

Figure 5.6: Pressure B in cylinder.

In figure 5.7 the pressure A in the cylinder can be seen. It can be seen that the steady state values for the simulation corresponds well with the measured data. It can furthermore be seen that both the amplitude and damping for the pressure spikes are too high for the simulated data.

The high damping in the Simulink model has been chosen because the simulated pressure spikes are higher compared to the measured data. This can especially be seen during the time interval between t = 17s to t = 45s. During this time period the measured data oscillates the whole time period with a low amplitude and a low damping. In contrast the simulated data oscillates with a higher amplitude in the beginning but does not oscillate during the whole time period.
The zoom has been conducted because the high amplitudes for the oscillations causes the cylinder position to vibrate (both in the simulations and the measured data). The zoom and the vibrations are discussed in the next section.

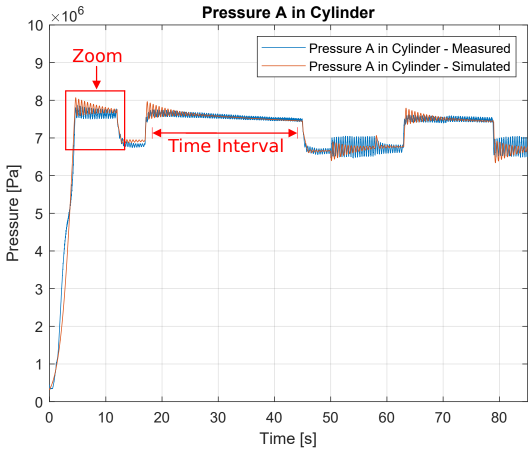

Figure 5.7: Pressure A in cylinder.

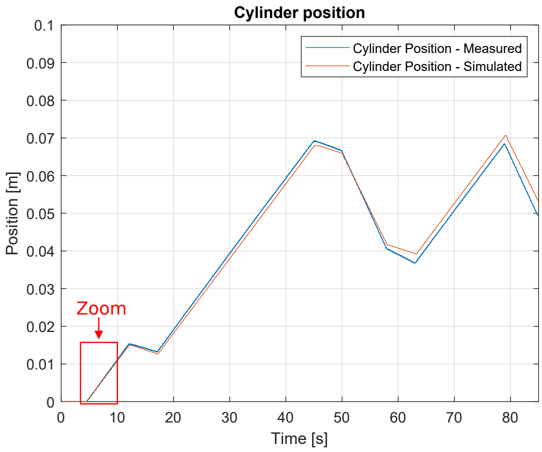

Figure 5.8: Cylinder position.

In figure 5.8 the cylinder position can be seen. It can be seen that the simulated data corresponds well with the measured data. As discussed in section 5.2 then it can be seen that the leakage model causes the simulated data to deviate from the measured data when the motor speed is 0 rad/s.
The zoom of the cylinder position is discussed in the following section.

5.4 Discussion

In figure 5.9 is zoom of the pressure A can be seen. It can be seen that the amplitude of the pressure oscillations is to high and that the frequency is to low compared to the measured data. These pressure oscillations can also be seen in figure 5.10. It can be seen that the amplitude for the simulated oscillations for the cylinder position is too high and that the frequency is too low (as for the simulated pressure).
It is believed that the reason for this is the modelled torsion spring. Therefore a simulation for the chosen spring constant k_s and a low k_s has been carried out. This is seen in figure 5.11.

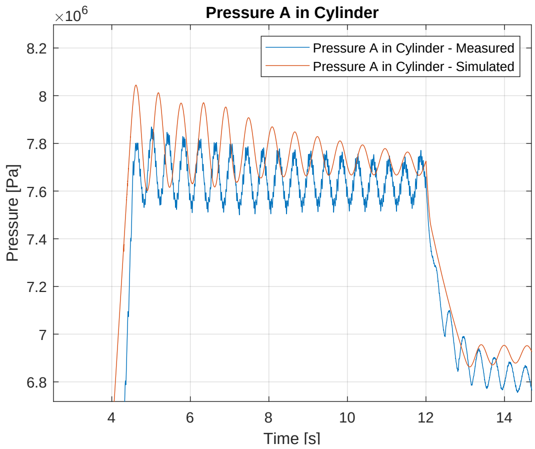

Figure 5.9: Pressure A in cylinder - Zoom.

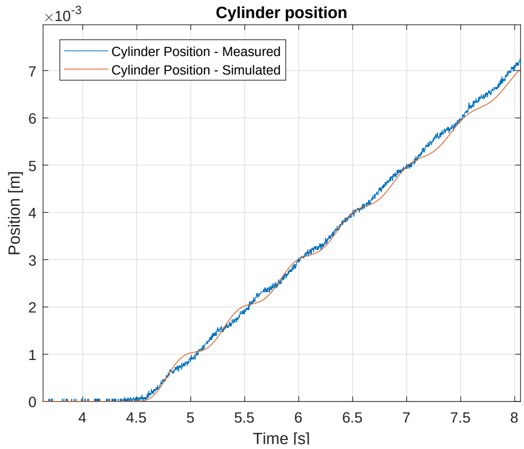

Figure 5.10: Cylinder position - Zoom.

Based on figure 5.11 then it can be seen that a higher value for k_s tends to give rise to the wanted pressure dynamics (higher frequency and lower damping). However, the model has calculation challenges for higher values for k_s, and thus a compromise has been taken.

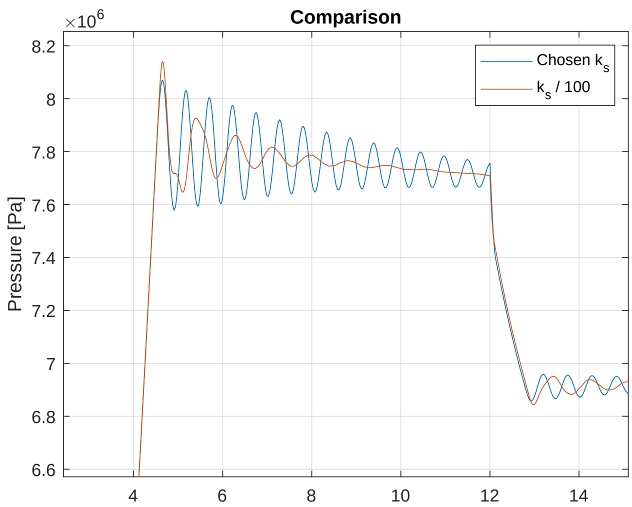

Figure 5.11: Comparison between chosen k_s and low k_s.

The consequence of the compromise is that the eigenfrequency of the model is lower compared to the experimental setup. This means the resonance peak in the bodeplot (after the linearisation) is moved towards a lower frequency, and hereby the resonance peak is closer to the 0 dB line. This results in a more conservative controller design, and thus the designed controllers are still are going to be stable when implemented in the experimental setup.

An additional argument to justify the compromise is that in section 7.4 a high-pass filtered pressure feedback (HPPF) is designed. The HPPF damps the system more at high frequencies, and thus the HPPF affects the resonance peak of the experimental setup more compared to the simulation. Hereby the designed controllers are still going to be stable even though the eigenfrequency of the system is simulated to low.

6 Linearisation

The input for linear model is the reference speed for the motor ω_{ref}, and the output is the angel θ_1. In this chapter the transfer function seen in equation 6.1 is derived.

$$\frac{\theta_1}{\omega_{ref}} = G(s) \tag{6.1}$$

6.1 Mechanical Linearisation

In appendix E the Euler-Lagrange equation for the system is derived. The equation describing the dynamics is repeated in equation 6.2.

$$\underline{\underline{D}}(\underline{\theta})\underline{\ddot{\theta}} + \underline{\underline{C}}(\underline{\theta}, \underline{\dot{\theta}}) + \underline{\phi}(\underline{\theta}) = \underline{\tau} \tag{6.2}$$

In order to linearise the Euler-Lagrange equation then each term in the Euler-Lagrange equation is going to be studied in order to determine which terms are almost constants and which terms can be neglected. The study can be found in appendix G.

6.1.1 Summery of Appendix G

In this subsection a summery of appendix G is presented, and therefore only the results from Euler-Lagrange study is shown.
It is decided to keep the D-matrix constant ($\underline{\underline{D}}_0$), and the expression for $\underline{\underline{D}}_0^{-1}$ is seen in equation 6.3.

$$\underline{\underline{D}}_0^{-1} = \frac{1}{d_{11}d_{22} - d_{12}d_{21}} \begin{bmatrix} d_{22} & -d_{12} \\ -d_{21} & d_{11} \end{bmatrix} = \begin{bmatrix} d_a & d_b \\ d_c & d_d \end{bmatrix} \tag{6.3}$$

Furthermore, it is chosen to neglect the expression for $\underline{\underline{C}}(\underline{\theta}, \underline{\dot{\theta}})\underline{\dot{\theta}}$, and it is chosen to linearise the expressions for $\underline{\phi}$. The linearised expression for $\underline{\phi}$ is seen in equation 6.4.

$$\begin{bmatrix} \Delta\phi_1 \\ \Delta\phi_2 \end{bmatrix} = \begin{bmatrix} K_{\phi 1}\Delta\theta_1 \\ K_{\phi 2}\Delta\theta_1 + K_{\phi 3}\Delta\theta_2 \end{bmatrix} \tag{6.4}$$

Hereby the simplified and linear expression for the Euler-Lagrange expression is seen in equation 6.5.

$$\underline{\ddot{\theta}} = \underline{\underline{D}}_0^{-1}(\underline{\theta})[\underline{\tau} - \underline{\phi}(\underline{\theta})] \tag{6.5}$$

The viscous friction is also added to equation in order to see the whole, linear expression for the Euler-Lagrange equation. This can be seen in equation 6.6. It should be noted that the Δ-signs are omitted.

$$\underline{\ddot{\theta}} = \underline{\underline{D}}_0^{-1}(\underline{\theta}) \left(\begin{bmatrix} \tau_1 \\ 0 \end{bmatrix} - \begin{bmatrix} B_\omega \dot{\theta}_1 \\ B_s \dot{\theta}_2 \end{bmatrix} - \begin{bmatrix} K_{\phi 1}\theta_1 \\ K_{\phi 2}\theta_1 + K_{\phi 3}\theta_2 \end{bmatrix} \right) \tag{6.6}$$

6.1.2 Linearisation of τ_1

The expression for τ_1 is repeated in equation 6.7.

$$\tau_1 = F_{cyl} \cdot |AC| \cdot sin(\theta_\tau) \tag{6.7}$$

With θ_τ given by equation 6.8.

$$\theta_\tau = cos^{-1}\left(\frac{|(BC_{min}+x)|^2 + |AC|^2 - |AB|^2}{2 \cdot |(BC_{min}+x)| \cdot |AC|}\right) \tag{6.8}$$

The expression for θ_τ depends on the cylinder position, and the cylinder position corresponds to an angular position as seen in equation 6.9.

$$x = \sqrt{(-cos(\theta_1 - \alpha_1 + \alpha_2)) \cdot 2 \cdot |AB| \cdot |AC| + |AB|^2 + |AC|^2} - |BC|_{min} \tag{6.9}$$

In order to linearise the expression for τ_1 then the first order Taylor approximation is used.

$$\tau_1(\theta_1, p_A) \approx \tau_1(\theta_{10}, p_{A0}) + \underbrace{\frac{\partial \tau_1}{\partial \theta_1}\bigg|_{\theta_{10},p_{A0}}}_{K_{\tau 1}}(\theta_1 - \theta_{10}) + \underbrace{\frac{\partial \tau_1}{\partial p_A}\bigg|_{\theta_{10},p_{A0}}}_{K_{\tau 2}}(p_A - p_{A0}) \tag{6.10}$$

$$\Delta\tau_1 = K_{\tau 1} \cdot \Delta\theta_1 + K_{\tau 2} \cdot \Delta p_A \tag{6.11}$$

$K_{\tau i}$	Linearisation constant, i = 1,2

6.2 Hydraulic Linearisation

During normal operation of the experimental setup the POCV are always open, and the pressure B in the cylinder is almost constant. Therefore it is decided to simplify the hydraulic system, and the simplification is seen in figure 6.1.

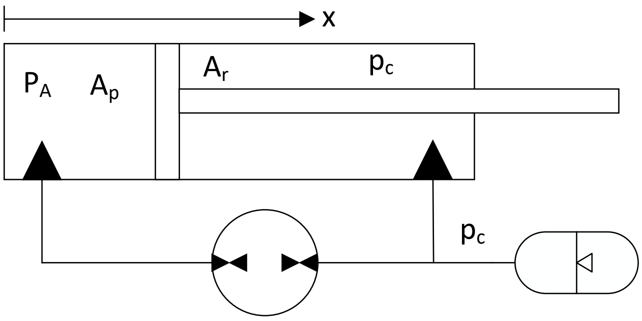

Figure 6.1: Hydraulic simplification used for linearisation.

The continuity equation for chamber A is given by equation 6.12.

$$\dot{p}_A = (K_V \cdot w_{act} \cdot \eta_p - K_{L,ext} \cdot (p_A - p_{Acc}) - K_{L,int} \cdot (p_A - p_B) - Ap \cdot \dot{x}) \cdot \frac{\beta_{eff}}{Ap \cdot x + V_A} \tag{6.12}$$

The expression for p_{acc} and p_B are now substituted with the constant pressure p_c.

$$\dot{p}_A = (K_V \cdot w_{act} \cdot \eta_p - K_{L,ext} \cdot (p_A - p_c) - K_{L,int} \cdot (p_A - p_c) - Ap \cdot \dot{x}) \cdot \frac{\beta_{eff}}{Ap \cdot x + V_A} \tag{6.13}$$

In order to linearise 6.13 then the constant pressure p_c is neglected. Furthermore, the bulk modulus and the cylinder position are assumed constants. This can be seen in equation 6.14.

$$\dot{p}_A = (K_V \cdot w_{act} \cdot \eta_p - K_{L,ext} \cdot p_A - K_{L,int} \cdot p_A - Ap \cdot \dot{x}) \cdot \frac{\beta_{lin}}{V_{lin}} \tag{6.14}$$

As it can be seen in equation 6.14 then the expression depends on the $\dot{x}$. However, the expressions for the mechanical linearisation depends on angular states. Therefore it is decided to change equation 6.14 such that it depends on $\dot{\theta}_1$. The link between the cylinder velocity and the angular velocity is given by equation 6.15.

$$\dot{x} = \frac{-(sin(-\theta_1 + \alpha_1 - \alpha_2) \cdot |AB| \cdot |AC|)}{\sqrt{-2 \cdot cos(-\theta_1 + \alpha_1 - \alpha_2) \cdot |AB| \cdot |AC| + |AB|^2 + |AC|^2}} \cdot \dot{\theta}_1 \tag{6.15}$$

By using the first order Taylor approximation then equation 6.15 reduces to equation 6.16.

$$\dot{x}(\theta_1, \dot{\theta}_1) \approx \dot{x}(\theta_{10}, \dot{\theta}_{10}) + \underbrace{\frac{\partial \dot{x}}{\partial \theta_1}\Big|_{\theta_{10}, \dot{\theta}_{10}}}_{K_{LA1}} (\theta_1 - \theta_{10}) + \underbrace{\frac{\partial \dot{x}}{\partial \dot{\theta}_1}\Big|_{\theta_{10}, \dot{\theta}_{10}}}_{K_{LA2}} (\dot{\theta}_1 - \dot{\theta}_{10}) \tag{6.16}$$

$$\Delta \dot{x}(\theta_1, \dot{\theta}_1) = K_{LA1} \cdot \Delta\theta_1 + K_{LA2} \cdot \Delta\dot{\theta}_1 \tag{6.17}$$

K_{LAi}	Constant transforming linear velocity into angular velocity, i = 1,2

6.3 State Space Representation

The linear differential equations for the mechanical system are given in the following (The Δ-signs are omitted):

$$\ddot{\theta}_1 = d_a \cdot (K_{\tau 1}\theta_1 + K_{\tau 2}p_A - B_\omega \dot{\theta}_1 - K_{\phi 1}\theta_1) + d_b \cdot (-B_s\dot{\theta}_2 - K_{\phi 2}\theta_1 - K_{\phi 3}\theta_2) \tag{6.18}$$

$$\ddot{\theta}_2 = d_c \cdot (K_{\tau 1}\theta_1 + K_{\tau 2}p_A - B_\omega \dot{\theta}_1 - K_{\phi 1}\theta_1) + d_d \cdot (-B_s\dot{\theta}_2 - K_{\phi 2}\theta_1 - K_{\phi 3}\theta_2) \tag{6.19}$$

The linear differential equation for the hydraulic system is given in the following (The Δ-signs are omitted):

$$\dot{p}_A = (K_V \cdot w_{act} \cdot \eta_p - K_{L,ext} \cdot p_A - K_{L,int} \cdot p_A - Ap \cdot (K_{LA1} \cdot \theta_1 + K_{LA2} \cdot \dot{\theta}_1)) \cdot \frac{\beta_{lin}}{V_{lin}} \tag{6.20}$$

Now the differential equations are transformed into state space form. The state space representation is seen in equation 6.21.

$$\begin{aligned} \underline{\dot{x}} &= \underline{\underline{A}}\underline{x} + \underline{\underline{B}}\underline{u} \\ \underline{y} &= \underline{\underline{C}}\underline{x} \end{aligned} \tag{6.21}$$

The state vector and the derivative of the state vector is given by equation 6.22.

$$\underline{x} = \begin{bmatrix} x_1 \\ x_2 \\ x_3 \\ x_4 \\ x_5 \\ x_6 \\ x_7 \end{bmatrix} = \begin{bmatrix} \theta_1 \\ \dot{\theta}_1 \\ \theta_2 \\ \dot{\theta}_2 \\ p_A \\ \omega_{act} \\ \dot{\omega}_{act} \end{bmatrix} \quad , \quad \underline{\dot{x}} \begin{bmatrix} \dot{\theta}_1 \\ \ddot{\theta}_1 \\ \dot{\theta}_2 \\ \ddot{\theta}_2 \\ \dot{p}_A \\ \dot{\omega}_{act} \\ \ddot{\omega}_{act} \end{bmatrix} \tag{6.22}$$

The state space representation of equation 6.18, 6.19 and 6.20 can be seen below.

$$\underline{\underline{A}x} = \begin{bmatrix} 0 & 1 & 0 & 0 & 0 & 0 & 0 \\ d_a(K_{\tau 1} - K_{\phi 1}) - d_b K_{\phi 2} & -d_a B_\omega & -d_b K_{\phi 3} & -d_b B_s & d_a K_{\tau 2} & 0 & 0 \\ 0 & 0 & 0 & 1 & 0 & 0 & 0 \\ d_c(K_{\tau 1} - K_{\phi 1}) - d_d K_{\phi 2} & -d_c B_\omega & -d_d K_{\phi 3} & -d_d B_s & d_c K_{\tau 2} & 0 & 0 \\ -A_p K_{LA1} \frac{\beta_{lin}}{V_{lin}} & -A_p K_{LA2} \frac{\beta_{lin}}{V_{lin}} & 0 & 0 & (-K_{L,ext} - K_{L,int}) \frac{\beta_{lin}}{V_{lin}} & K_V \eta_p \frac{\beta_{lin}}{V_{lin}} & 0 \\ 0 & 0 & 0 & 0 & 0 & 0 & 1 \\ 0 & 0 & 0 & 0 & 0 & -\omega_{n,m}^2 & -2\zeta_m \omega_{n,m} \end{bmatrix} \begin{bmatrix} \theta_1 \\ \dot{\theta}_1 \\ \theta_2 \\ \dot{\theta}_2 \\ p_A \\ \omega_{act} \\ \dot{\omega}_{act} \end{bmatrix} \tag{6.23}$$

$$\underline{\underline{B}u} = \begin{bmatrix} 0 \\ 0 \\ 0 \\ 0 \\ 0 \\ 0 \\ \omega_{n,m}^2 \end{bmatrix} \omega_{ref} \quad , \quad \underline{\underline{C}x} = \begin{bmatrix} 1 & 0 & 0 & 0 & 0 & 0 & 0 \end{bmatrix} \begin{bmatrix} \theta_1 \\ \dot{\theta}_1 \\ \theta_2 \\ \dot{\theta}_2 \\ p_A \\ \omega_{act} \\ \dot{\omega}_{act} \end{bmatrix} \tag{6.24}$$

6.4 Choice of Linearisation Point

In order to determine the linearisation point for θ_{10}, $\dot{\theta}_{10}$ and θ_{20} then different linearisation points have been tested.
It is desired to choose a linearisation point with low damping, low gain margin and low phase margin. This is desired because if such a linearisation point is chosen then the linearisation point represents the worst case scenario with respect of stability of the system.

Linearisation point θ_{10}

In figure 6.2 a sweep for different values for θ_{10} is seen. Based on figure 6.2 it can be seen that the choice for θ_{10} does not change the bode diagram drastically. However, it can be seen that if θ_{10} is chosen near $\theta_{1,min}$ then the eigenfrequency of the system is lower and gain margin decreases. Therefore it is chosen to linearise the system near $\theta_{1,min}$.

Legend:	$\theta 1 - min$	$\theta 1 - min/2$	$\theta 1 - 0$	$\theta 1 - max/2$	$\theta 1 - max$
Corresponds To: [rad]	$\theta_{1,min}$	$\theta_{1,min}/2$	0	$\theta_{1,max}/2$	$\theta_{1,max}$

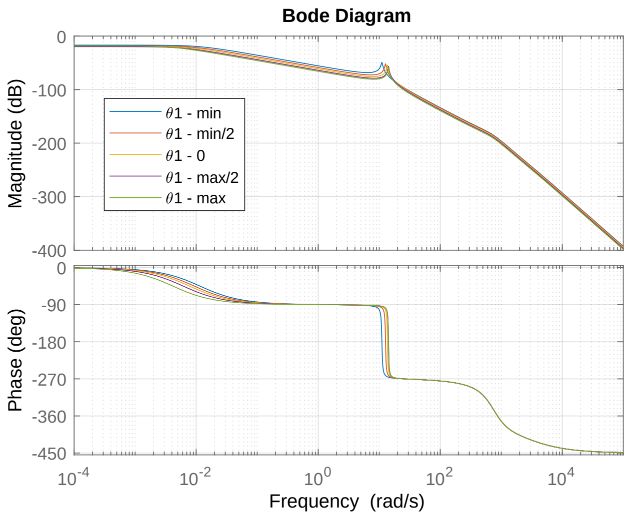

Figure 6.2: Sweep for different values of θ_1.

Linearisation point $\dot{\theta}_{10}$

In figure 6.3 a sweep for different values for $\dot{\theta}_{10}$ is seen. The values for $\dot{\theta}_{10}$ are based on the expected maximum and minimum angular velocities for the trajectory. It can be seen that the choice of $\dot{\theta}_{10}$ influences the frequency area in the range of 0 rad/s to 1 rad/s. However, since the resonance peak is placed at 12 rad/s then this only has a small impact on stability issues. It can be seen that the angular velocity does not influence the resonance peak a lot. Therefore it is concluded that the choice for $\dot{\theta}_{10}$ does not play an important role.

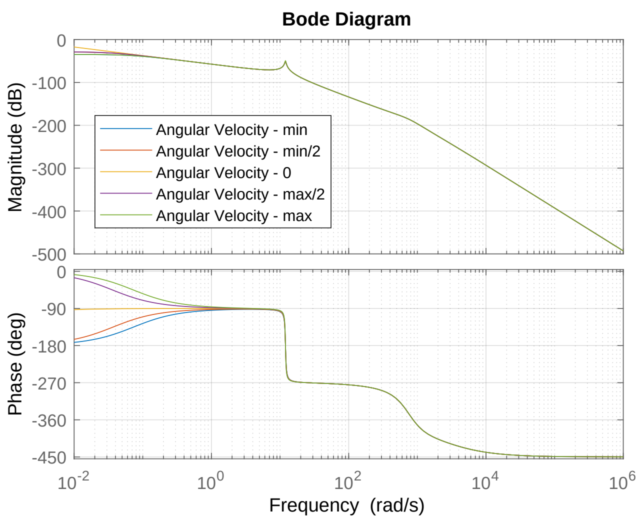

Figure 6.3: Sweep for different values of $\dot{\theta}_1$.

Linearisation point θ_{20}

In figure 6.4 a sweep for different values for θ_{20} is seen. Based on figure 6.4 it can be seen that the choice for θ_{20} only has a small influence on stability issues. Therefore it is concluded that the choice for $\dot{\theta}_{20}$ does not play an important role.

Legend:	$\theta 2 - min$	$\theta 2 - min/2$	$\theta 2 - 0$	$\theta 2 - max/2$	$\theta 2 - max$
Corresponds To: [rad]	$\theta_{2,min}$	$\theta_{2,min}/2$	0	$\theta_{2,max}/2$	$\theta_{2,max}$

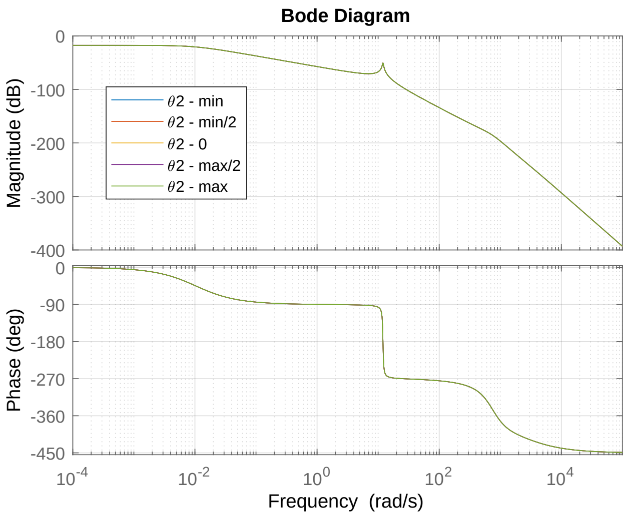

Figure 6.4: Sweep for different values of θ_2.

Chosen Linearisation Point

In the table below the chosen linearisation point can be seen. The values for θ_{10}, $\dot{\theta}_{10}$ and θ_{20} are chosen based on the bode diagram analysis in this section, and the value for p_{A0} has been determined through a simulation by the nonlinear model (the value of p_A in the linearisation point - see figure 6.6).

Linearisation Point	θ_{10} [rad]	$\dot{\theta}_{10}$ [rad/s]	θ_{20} [rad]	p_{A0} [Pa]	β_{lin} [Pa]
Value	-0.3	$6.06 \cdot 10^{-3}$	$-1.34 \cdot 10^{-5}$	$7.52 \cdot 10^{6}$	$9.5 \cdot 10^{8}$

6.5 Validation of the Linear Model

The validation of the linear model is carried out by comparing the linear model with the non linear model. Both models receives a step input at the chosen linearisation point.

Positive Step Input

In figure 6.5 the reference input for the linear and nonlinear model can be seen. It can be seen that the linear and the nonlinear motor model are very similar. The reason for this is that the motor motor was approximated as a second order system in section 4.1. The step input at 18 sec corresponds to an increase of 25 RPM in the motor speed.
In figure 6.6 pressure A in the cylinder can be seen. It can be seen that the frequency corresponds well, but a steady state error is present.

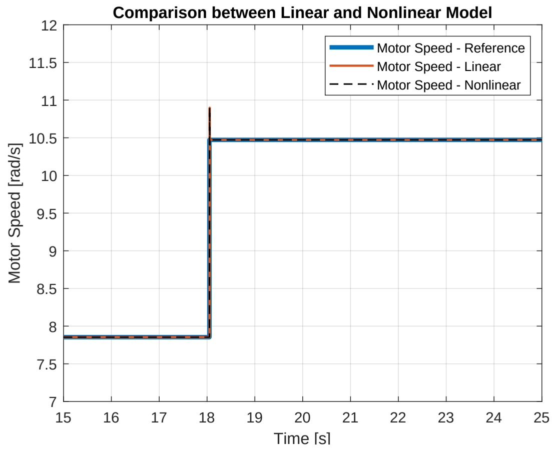

Figure 6.5: Step input.

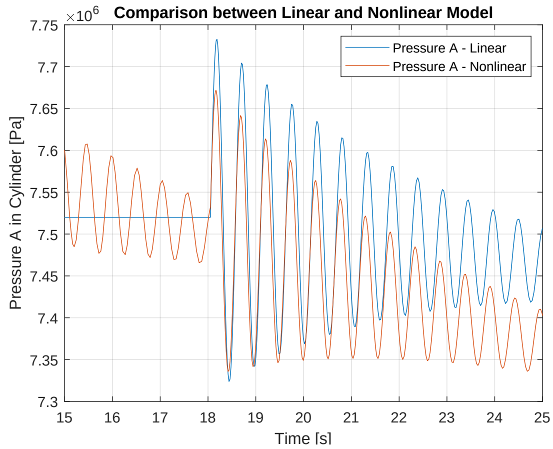

Figure 6.6: Pressure A in the cylinder.

The angular velocities ($\dot{\theta}_1$ and $\dot{\theta}_2$) can be seen in figure 6.7 and 6.8. As for the pressure then it can be seen that the frequency corresponds well, but a steady state error is present.

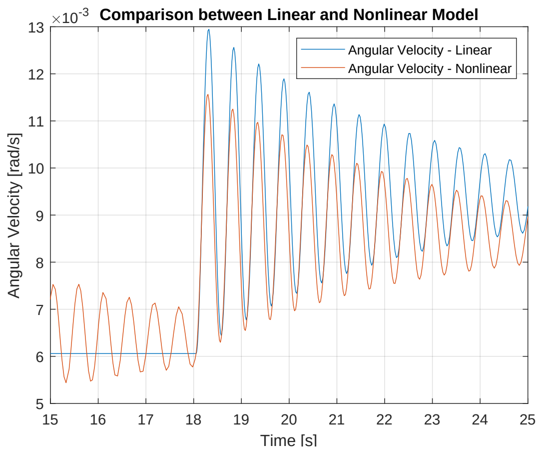

Figure 6.7: Angular velocity $\dot{\theta}_1$.

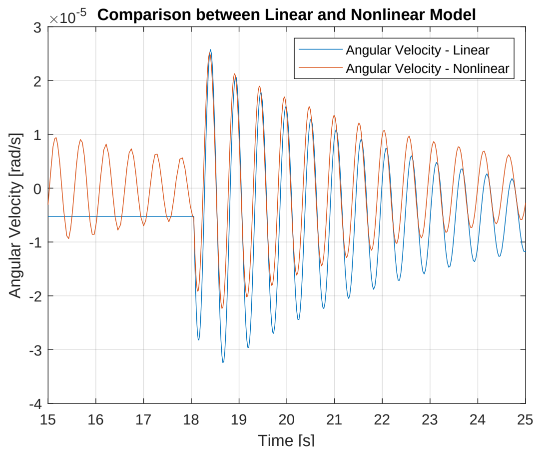

Figure 6.8: Angular velocity $\dot{\theta}_2$.

Negative Step Input

As for the positive step input then the negative step input is applied at t = 18 sec. The negative step input decreases the velocity by 25 RPM. The anglular velocities ($\dot{\theta}_1$ and $\dot{\theta}_2$) can be seen in figure 6.9 and 6.9. In the figures it can be seen that the the frequency corresponds well, but a steady state error is present.

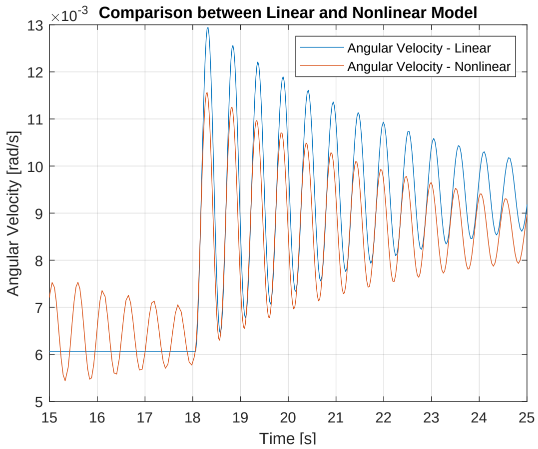

Figure 6.9: Angular velocity $\dot{\theta}_1$.

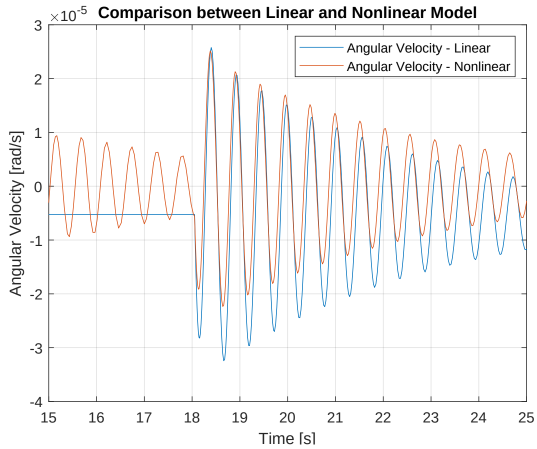

Figure 6.10: Angular velocity $\dot{\theta}_2$.

6.6 Linearisation - Preliminary Conclusion

In this chapter the linearisation of the model was conducted. It was shown that that the linear model describes the dynamics of the nonlinear model accurately, but that a steady state error was present.
The phase and gain margin of the derived transfer function can be seen in figure 6.11. It can be seen that a resonance peak is present is approximately 12 [rad/s]. This resonance peak has to be taken into account when designing the controllers.

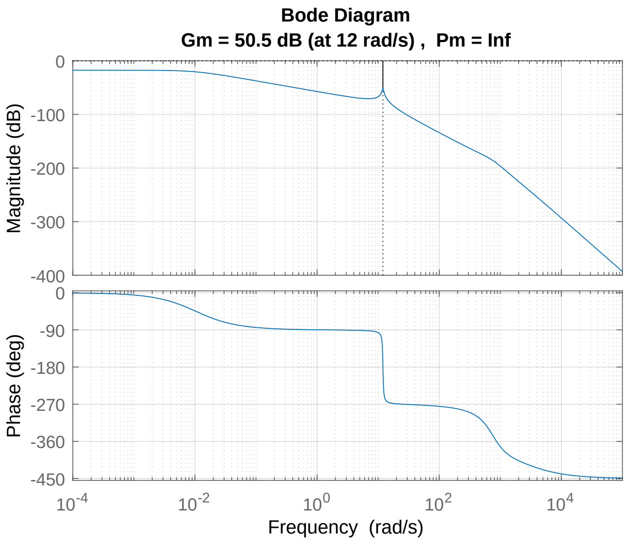

Figure 6.11: Phase and gain margin for G(s).

7 | Position Controller Design

7.1 Trajectory Planning

A benchmark trajectory has been developed in order test the position controllers, and the chosen position trajectory for the angle θ_1 is seen in figure 7.1. It can be seen that the position trajectory contains an initialisation period. The idea behind the initialisation period is to move the cylinder piston away from the end stop such that the system has time to build up pressure. Furthermore, a time period has been added for static hold such that the POCV can be closed. Hereby static hold of the crane boon can be applied, and pressure control can be applied. A safety period has also been added. The safety period is added in case an overshot is present during the controller tests. Without the safety period then the cylinder could hit the end stop with a great amount of force and the experimental setup could be damage. Lastly, as it can be seen in figure 7.1 then values on the y-axis is present. These values are present in order to show that the controllers are tested in a large spectrum of position values.
The position trajectory has been created based on the reference for the acceleration seen in figure 7.2. The reference for the acceleration has been created by a series of ramp-inputs. The velocity and position references has been created by integrating the acceleration reference. Care must be taken when choosing the slope for the acceleration reference. If the slope is too high then the reference input for the motor (ω_{ref}) will exceed 3000 RPM (which is the limit).

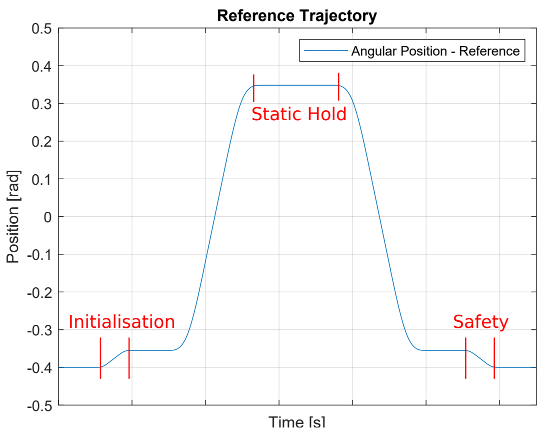

Figure 7.1: Chosen position reference.

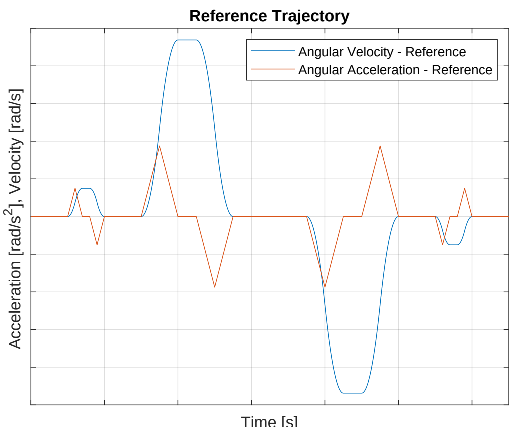

Figure 7.2: Velocity and acceleration reference.

7.2 Velocity Feed Forward

Velocity feed forward (VFF) can improve the control performance of the system. The idea behind VFF can be seen in figure 7.3. The desired velocity trajectory is multiplied by a V_{FF}-block, and hereby an additional input-reference for the motor is generated.

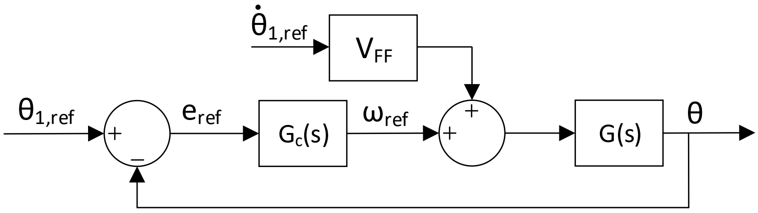

Figure 7.3: Block diagram of the implementation of the velocity feed forward control.

V_{FF} is determined by analysing the pump flow to chamber A in the cylinder. Furthermore an approximation for Q_{PA} is made:

$$\begin{aligned} Q_{PA} &\approx \dot{x} \cdot A_p \\ \dot{x} \cdot A_p &\approx K_V \cdot \omega_{act} \cdot \eta_p - Q_{ext,A} - Q_{int} \end{aligned} \tag{7.1}$$

Since the motor is fast then $\omega_{act} \approx \omega_{ref}$.

$$\omega_{ref} \approx \frac{\dot{x} \cdot A_p + Q_{ext,A} + Q_{int}}{K_V \cdot \eta_p} \approx \dot{x} \cdot \frac{A_p + \frac{Q_{ext,A}}{\dot{x}} + \frac{Q_{int}}{\dot{x}}}{K_V \cdot \eta_p} \tag{7.2}$$

Lastly, the correlation between $\dot{x}$ and $\dot{\theta}_1$ is seen in equation 7.3. The correlation is derived in section 4.3.5.

$$\dot{x} = \frac{-(sin(-\theta_1 + \alpha_1 - \alpha_2) \cdot |AB| \cdot |AC|)}{\sqrt{-2 \cdot cos(-\theta_1 + \alpha_1 - \alpha_2) \cdot |AB| \cdot |AC| + |AB|^2 + |AC|^2}} \cdot \dot{\theta}_1 \tag{7.3}$$

By inserting equation 7.3 in equation 7.2 then equation 7.4 is derived.

$$\omega_{ref} \approx \dot{\theta}_{1,ref} \cdot V_{FF}(\theta_1, p_{pA}, p_{pB}, p_{acc}) \tag{7.4}$$

In order to analysis whether or not the VFF affects the system then a block diagram manipulation is seen in figure 7.4. It can be seen that the VFF works a pre-filter, and thus it does not affect the stability of the closed loop.

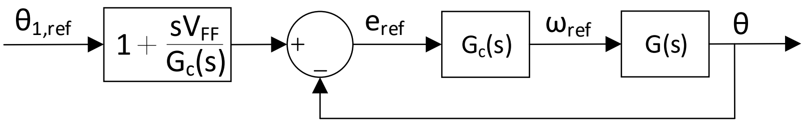

Figure 7.4: Block diagram showing the analysis of velocity feed forward control.

7.2.1 Simulationtest of VFF without Feedback Controller

In order to test how well the designed VFF works then a simulation is conducted without the use of a feedback controller. The reference and the simulated angular position is seen in figure 7.5. It can be seen that the reference is tracked precisely. The reason for the deviation in the beginning, top and end is caused by the pressure build up in chamber A. It is believed that when a feed back controller is added then this error will decrease.

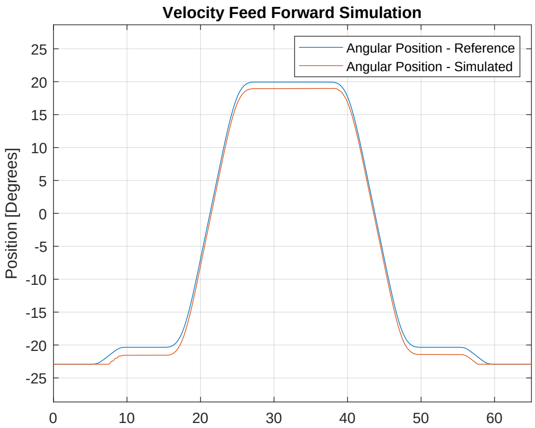

Figure 7.5: Chosen position reference.

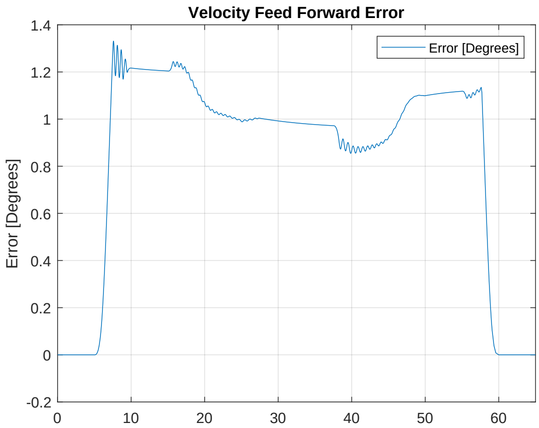

Figure 7.6: Error for VFF control.

Based on the simulation test for VFF then it is concluded that VFF should be implemented along with a feedback controller.

7.3 Linear Controller Design without HPPF

Initially it is decided to design a P-controller in order to compare the controller design before and after the implementation of the HPPF. Therefore this section serves as an argument for HPPF design.
It is decided to design the P-controller such that the gain-margin is 8 dB. This gain margin is chosen because then the controller gain can be high and a safety margin of 8 dB is sufficient. The controller gain can be seen in equation 7.5.

$$K_{p,c} = 133.1 \tag{7.5}$$

7.4 Damping with Pressure Feedback

It is decided to implement pressure feedback such that a higher damping of the system is achieved. Two different pressure feedback methods have been tested, and they are listed below.

- Passive pressure feedback (Appendix H)
- High-pass filtered pressure feedback

Based on the analysis in appendix H it is decided not to implemented the passive pressure feedback because it reduces the DC gain significantly. For this reason the passive pressure feedback is also moved to appendix H.

7.4.1 High-Pass Filter Pressure Feedback (HPPF)

The pressure feedback with a high-pass filter is seen in equation 7.6.

$$G_{HPPF} = \frac{p_D}{p_A} = K_{HPPF} \cdot \frac{s\,\omega_f}{s+\omega_f} \quad , \quad \omega_f = \frac{\omega_n}{2} \tag{7.6}$$

p_D | Damping pressure - Additional state [Pa]

The high-pass filter is incorporated in the state space model, and thus an additional state is included in the state space model. Equation 7.6 is transformed into the time domain and $\dot{p}_D$ is isolated in equation 7.7.

$$\dot{p}_D = \omega_f \cdot (K_{HPPF} \cdot \dot{p}_A - p_D) \tag{7.7}$$

Now $\dot{p}_A$ is replaced.

$$\dot{p}_D = \omega_f \cdot \left(K_{HPPF} \cdot \left(\frac{\beta_{lin}}{V_{lin}} (K_V \omega_{act} \eta_p - K_{L,ext} p_A - K_{L,int} p_A - A_p \cdot (K_{LA1} \theta_1 + K_{LA2} \dot{\theta}_1)) \right) - p_D \right) \tag{7.8}$$

For convenience then the following constants are defined.

$$K_L = K_{L,ext} + K_{L,int} \quad , \quad C_D = \omega_f \cdot K_{HPPF} \cdot \frac{\beta_{lin}}{V_{lin}} \tag{7.9}$$

It is decided to neglect the motor dynamics of the system, because the motor is significantly faster compared to the rest of the system.
Hereby the state vector and the derivative of the state vector is given by equation 7.10.

$$\underline{x} = \begin{bmatrix} x_1 \\ x_2 \\ x_3 \\ x_4 \\ x_5 \\ x_6 \end{bmatrix} = \begin{bmatrix} \theta_1 \\ \dot{\theta}_1 \\ \theta_2 \\ \dot{\theta}_2 \\ p_A \\ p_D \end{bmatrix} \quad , \quad \dot{\underline{x}} \begin{bmatrix} \dot{\theta}_1 \\ \ddot{\theta}_1 \\ \dot{\theta}_2 \\ \ddot{\theta}_2 \\ \dot{p}_A \\ \dot{p}_D \end{bmatrix} \tag{7.10}$$

The state space matrices are seen in equation 7.11 and 7.12.

$$\underline{\underline{A}}\underline{x} = \begin{bmatrix} 0 & 1 & 0 & 0 & 0 & 0 \\ d_a(K_{\tau 1} - K_{\phi 1}) - d_b K_{\phi 2} & -d_a B_\omega & -d_b K_{\phi 3} & -d_b B_s & d_a K_{\tau 2} & 0 \\ 0 & 0 & 0 & 1 & 0 & 0 \\ d_c(K_{\tau 1} - K_{\phi 1}) - d_d K_{\phi 2} & -d_c B_\omega & -d_d K_{\phi 3} & -d_d B_s & d_c K_{\tau 2} & 0 \\ -A_p K_{LA1} \frac{\beta_{lin}}{V_{lin}} & -A_p K_{LA2} \frac{\beta_{lin}}{V_{lin}} & 0 & 0 & -K_L \frac{\beta_{lin}}{V_{lin}} & -K_V \eta_p \frac{\beta_{lin}}{V_{lin}} \\ -C_D A_p K_{LA1} & -C_D A_p K_{LA2} & 0 & 0 & -C_D K_L & -C_D K_V \eta_p - \omega_f \end{bmatrix} \begin{bmatrix} \theta_1 \\ \dot{\theta}_1 \\ \theta_2 \\ \dot{\theta}_2 \\ p_A \\ p_D \end{bmatrix} \tag{7.11}$$

$$\underline{\underline{B}}\underline{u} = \begin{bmatrix} 0 \\ 0 \\ 0 \\ 0 \\ K_V \eta_p \frac{\beta_{lin}}{V_{lin}} \\ K_V \eta_p C_D \end{bmatrix} \omega_{ref} \quad , \quad \underline{\underline{C}}\underline{x} = \begin{bmatrix} 1 & 0 & 0 & 0 & 0 & 0 \end{bmatrix} \begin{bmatrix} \theta_1 \\ \dot{\theta}_1 \\ \theta_2 \\ \dot{\theta}_2 \\ p_A \\ p_D \end{bmatrix} \tag{7.12}$$

In figure 7.7 the bode diagram for transfer function with and without the high-pass filtered pressure feedback is seen. It can be seen that the high-pass filtered pressure feedback works. The HPPF damps the second order system without decreasing the DC gain.

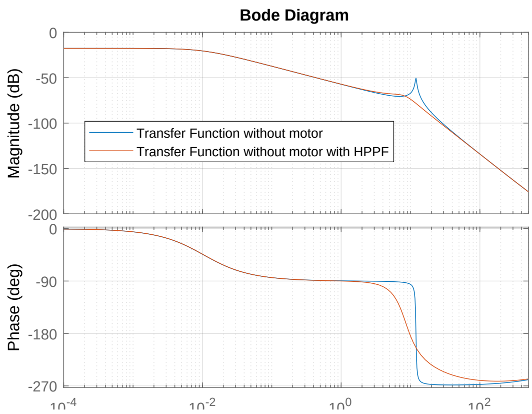

Figure 7.7: Effect of HPPF.

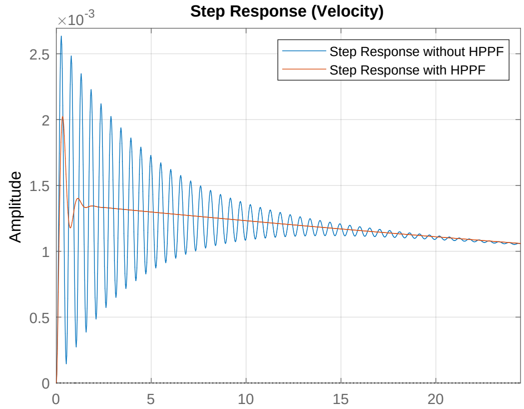

Figure 7.8: Effect of HPPF.

In order to see the effect of the HPPF then system has been given a step response (with the velocity as output). As it can be seen in figure 7.8 then the HPPF damps the oscillations.

7.5 Linear Controller Design with HPPF

In this section 4 different position controllers are designed. It is chosen to design a P-controller because it is capable of reducing the steady steady error and improving the transient response. Furthermore, 2 different PI-controller are designed. The integral term ensures 0 steady state error, and thus the position error can be decreased. Lastly, it is chosen to design a P-lead controller because hereby the bandwidth can be increased.
The 4 different controllers are seen below.

- P-controller
- PI-controller (PM $\approx$ 40 degrees)
- PI-controller (No overshot in step response)
- P-lead controller

The P-controller and the PI-controller with GM $\approx$ 40 degrees are designed analytically, and thus the GM and PM are listed for the transfer function with HPPF.

$$\begin{aligned} \text{GM}_{HPPF} &= 72.9 \text{ dB} \\ \text{PM}_{HPPF} &= \text{Inf} \end{aligned} \tag{7.13}$$

In general a design criteria of GM $\approx$ 8 dB and/or PM $\approx$ 40 degrees are desired [12].

P-Controller

The P-controller is designed analytically, and the gain for the P-controller is seen in equation 7.14.

$$K_P = \frac{1}{(72.9 - 8)dB} = 1758 \tag{7.14}$$

PI-Controller (PM $\approx$ 40)

If the PI-controller is designed such that PM $\approx$ 40 then it normally leads to fast response and a only a small overshot [12]. The PI-controller is designed analytically.
First the frequency ω_{PI} for which the angle G(jω_{PI}) is equal to (-180^o + 40^o + 5^o) is determined.

$$\omega_{PI} = 7.05 rad/s \tag{7.15}$$

Then gain K_P is determined by equation 7.16.

$$K_P = \frac{1}{|G(j\omega_{PI})|} = \frac{1}{-68.745\ dB} = 2737 \tag{7.16}$$

Then gain K_I is determined by equation 7.17.

$$K_I = 0.1 \cdot \omega_{PI} \cdot K_P = 1930 \tag{7.17}$$

PI-Controller (No overshot in step response)

This PI-controller is designed by using the gain from the designed P-controller, and then adjusting the integral gain such that no overshoot is present in the closed loop step response. The gains can be seen below.

$$K_P = 1758 \quad , \quad K_I = 18 \tag{7.18}$$

From equation 7.18 it can be seen that $K_I << K_P$, and thus this controller performs almost as a P-controller.

P-lead Controller

The controller structure can be seen in equation 7.19.

$$G_{P-lead} = K_P \cdot \frac{\frac{s}{\omega_0} + 1}{\frac{s}{\omega_p} + 1} \quad , \quad \omega_0 < \omega_p \tag{7.19}$$

In general the lead controller is a form of high-pass filter because it amplifies the high frequency relative to the low frequencies [12]. This can be seen in figure 7.9. The bodeplot is shown without the K_P gain.

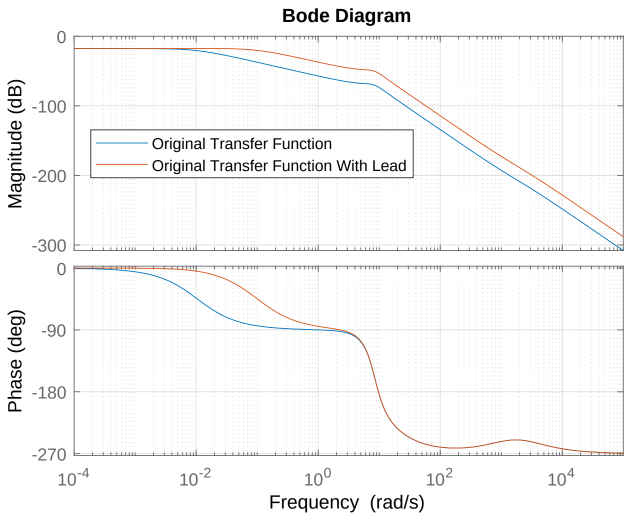

Figure 7.9: Step response with the velocity as output.

Next the K_P gain is adjusted such that a GM of 8 dB is achieved. Hereby the controller is given by equation 7.20.

$$G_{P-lead} = 177.8 \cdot \frac{100s + 1}{10s + 1} \tag{7.20}$$

7.6 Linear Position Controller Testing - Simulation

The benchmark trajectory is used to test the designed controllers. The results can be seen in figure 7.10. It can be seen that all of the designed position controllers are stable, and all controllers are capable of following the benchmark trajectory. However, as seen in figure 7.11 then the average error for P-lead controller is higher compared to the other controller designs. A reason for this could be that the chosen K_P value is lower compared to the other controllers.
It is concluded that all 4 controllers could be implemented in the experimental setup due to the low average errors.

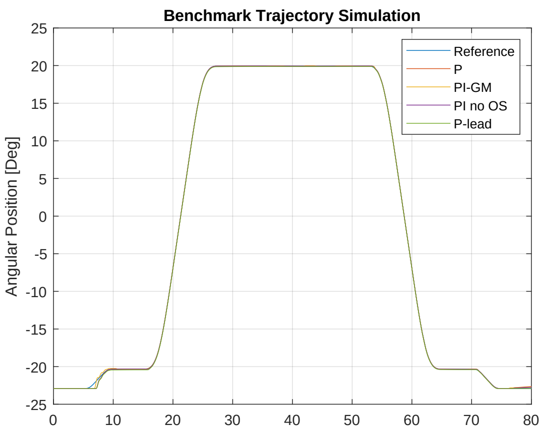

Figure 7.10: Reference trajectory and simulated position.

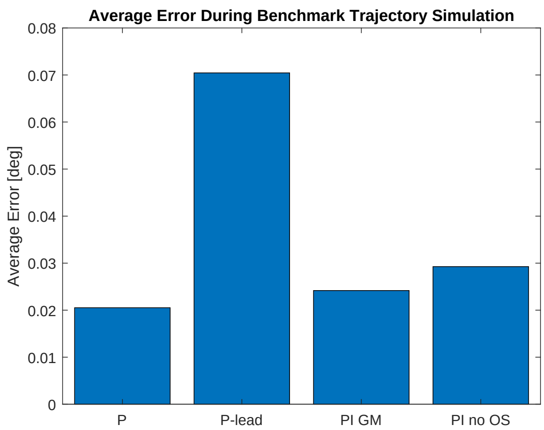

Figure 7.11: Average position error.

8 Pressure Controller Design

In chapter 2 the need for a pressure controller after the static hold operation is shown. The could be seen in figure 2.6, and in this chapter different pressure controllers are developed in order to reduce pressure oscillations.

8.1 State Space Representation

The pressure controllers are activated when the POCV's are closed, and therefore the hydraulic system can be reduced. The reduced hydraulic system can be seen in figure 8.1.

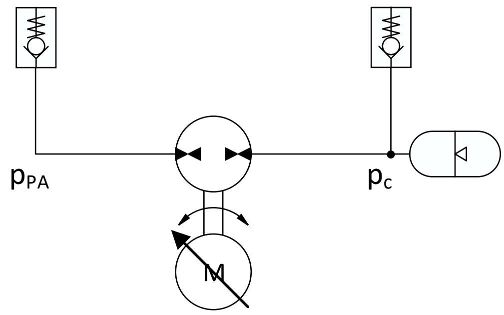

Figure 8.1: Sketch used to show the hydraulic system when the POCV's are closed.

The differential equation for the pressure can be seen in equation 8.1.

$$\dot{p}_{PA} = (K_V \cdot \omega_{act} \cdot \eta_p - K_{L,ext} \cdot p_{PA} - K_{L,int} \cdot p_{PA}) \cdot \frac{\beta_{PA}}{V_{PA}} \tag{8.1}$$

The dynamic of the motor is also included in the state space model, and therefore it is therefore decided that the state vector and the derivative of the state vector is given as in equation 8.2

$$\underline{x} = \begin{bmatrix} x_1 \\ x_2 \\ x_3 \end{bmatrix} = \begin{bmatrix} p_{PA} \\ \omega_{act} \\ \dot{\omega}_{act} \end{bmatrix} \quad , \quad \underline{\dot{x}} = \begin{bmatrix} \dot{p}_{PA} \\ \dot{\omega}_{act} \\ \ddot{\omega}_{act} \end{bmatrix} \tag{8.2}$$

The state space representation of the pressure dynamics when the POCV's are closed can be seen in equation 8.3 and 8.4.

$$\underline{\underline{A}x} = \begin{bmatrix} (-K_{L,ext} - K_{L,int}) \cdot \frac{\beta_{PA}}{V_{PA}} & K_V \cdot \eta_p \cdot \frac{\beta_{PA}}{V_{PA}} & 0 \\ 0 & 0 & 1 \\ 0 & -\omega_{n,m}^2 & -2\zeta_m \omega_{n,m} \end{bmatrix} \begin{bmatrix} p_{PA} \\ \omega_{act} \\ \dot{\omega}_{act} \end{bmatrix} \tag{8.3}$$

$$\underline{\underline{B}u} = \begin{bmatrix} 0 \\ 0 \\ \omega_{n,m}^2 \end{bmatrix} \omega_{ref} \quad , \quad \underline{\underline{C}x} = \begin{bmatrix} 1 & 0 & 0 \end{bmatrix} \begin{bmatrix} p_{PA} \\ \omega_{act} \\ \dot{\omega}_{act} \end{bmatrix} \tag{8.4}$$

8.2 Validation of Linear Pressure Model

In order to validate the linear pressure model then the motor is given a reference step input when the POCV's are closed. This can be seen in figure 8.2.

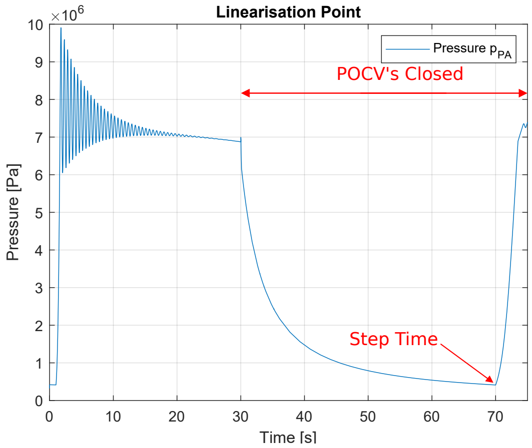

Figure 8.2: Graph showing the step time.

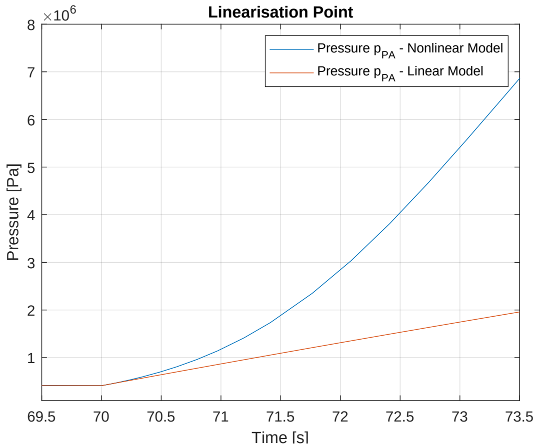

Figure 8.3: Comparison.

As it can be seen in figure 8.2 then the pressure p_{PA} decreases as long as the POCV's are closed. This results in a challenge regarding the validation of the linear pressure model because if the pressure p_{PA} varies then β_{PA} also varies. However, in the linear model β_{PA} is set to a constant value. Therefore it is expected that the linear model is only valid for a short period of time and that the nonlinear model is faster. This can be seen in figure 8.3.

The challenge regarding having a constant bulk modulus can be seen in figure 8.4. As it can be seen in figure 8.4 then the bode diagrams vary a lot for different choices for β_{PA}. This means that if a controller is designed on the worst case scenario then the controller choice would be conservative. This would lead to a slow respond (especially for low pressures).

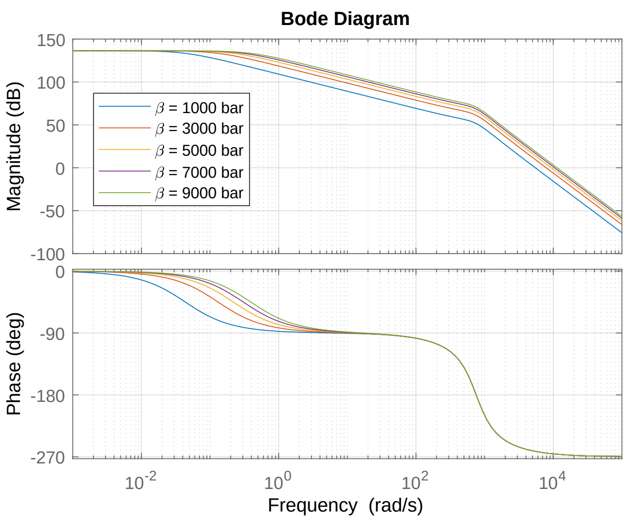

Figure 8.4: Bode diagram for different constant values for β_{PA}.

Instead of designing a conservative controller then a gain scheduling controller could be designed. The controller gains could be updated as a function of β_{PA}. This can be seen in figure 8.5.

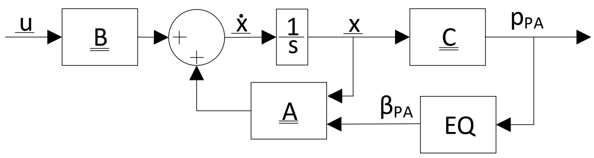

Figure 8.5: Block diagram showing the continuously updating of β_{PA}.

The system seen in figure 8.5 is given the same step input as for the constant β_{PA}. It can be seen in figure 8.6 that the updating β_{PA} graph follows the nonlinear graph more precisely. This indicates that designing a gain scheduling controller that depends on β_{PA} could be an idea.

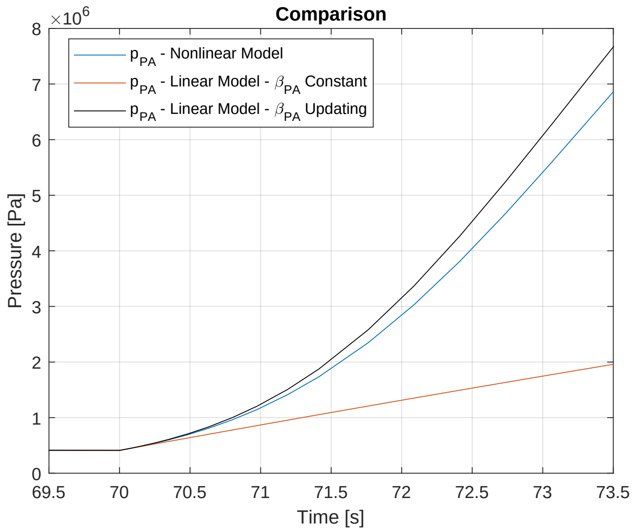

Figure 8.6: Block diagram showing the continuously updating of β_{PA}.

For these reasons it is decided to design gain schedule controllers. Furthermore, it is chosen to design a P-controller because it is capable of reducing the steady state error and improving the response. Furthermore, it is also chosen to design a PI-controller because the integral term insures 0 steady state error. The chosen controllers can be seen below.

- Conservative P-controller
- Conservative PI-controller
- Gain schedule P-controller
- Gain schedule PI-controller

8.3 Pressure Controller Design

8.3.1 Conservative Pressure Controller

As it is seen in the bode diagram for different, constant values of β_{PA} (figure 8.4) then the bode diagrams vary a lot depending on the chosen β_{PA}. The phase and gain margin have been calculated for each value for β_{PA}, and this can be seen in the table below.

	Gain Margin [dB]	Phase Margin [deg]
$\beta_{PA} = 1000$ [bar]	-51.6	-82.0
$\beta_{PA} = 3000$ [bar]	-61.2	-84.5
$\beta_{PA} = 5000$ [bar]	-65.6	-85.4
$\beta_{PA} = 7000$ [bar]	-68.5	-85.9
$\beta_{PA} = 9000$ [bar]	-70.7	-86.2

Table 8.1: Gain and phase margin for different, constant value of β_{PA}.

It can be seen that the worst case scenario is for $\beta_{PA} = 9000$. A controller is designed for this case because then the controller is stable for all working points.

Conservative P-controller

It is decided to design the P-controller with a design criteria of GM = 30 dB for β_{PA} = 9000 [bar]. This design criteria is chosen because it yields a time constant of 0.0423 seconds. The time time corresponds well with a sampling time of 0.001 seconds, because approximately 42 data points are measured within one time constant.

$$K_P = \frac{1}{(70.7 + 30)\ dB} = 9.2257 \cdot 10^{-6} \tag{8.5}$$

Conservative PI-controller

It is decided to design a PI-controller because then zero steady state error can be achieved. As for the P-controller a design criteria of GM = 30 dB for β_{PA} = 9000 [bar] is desired. Furthermore, an additional design criteria is that no overshot should be present, because an overshot would cause an undesired opening of the POCV.
The gain K_P is calculated with the same procedure as for the P-controller. Then the K_I value is determined by decreasing the value until no overshot is present for the closed loop step response. The gains are seen in equation 8.6.

$$\begin{aligned} K_P &= \frac{1}{(70.7 + 30)\ dB} = 9.2257 \cdot 10^{-6} \\ K_I &= 3.608 \cdot 10^{-6} \end{aligned} \tag{8.6}$$

8.3.2 Gain Scheduling - P and PI

Another design approach could be to calculate different P- and PI-controllers based on different values for β_{PA}. Hereby it would be possible to switch between different controllers based on the calculated value for β_{PA}. The design procedure is identical with the conservative P- and PI-controller, and thus it is not repeated. The values for the P-controller is only the values for the column K_p-values, whereas the controller gain for the PI-controller are seen in both the K_p- and K_I-colums. The calculated controller gains can be seen in table 8.2.

Chosen Linearisation Point	K_P-value	K_I-value	GM [dB]	PM [deg]
$\beta_{PA} = 2000$ $[bar]$	$4.1687 \cdot 10^{-5}$	$3.6080 \cdot 10^{-6}$	30.0	88.2
$\beta_{PA} = 3000$ $[bar]$	$2.7542 \cdot 10^{-5}$	$3.6080 \cdot 10^{-6}$	30.0	88.2
$\beta_{PA} = 4000$ $[bar]$	$2.0654 \cdot 10^{-5}$	$3.6080 \cdot 10^{-6}$	30.0	88.2
$\beta_{PA} = 5000$ $[bar]$	$1.6596 \cdot 10^{-5}$	$3.6080 \cdot 10^{-6}$	30.0	88.2
$\beta_{PA} = 6000$ $[bar]$	$1.3804 \cdot 10^{-5}$	$3.6080 \cdot 10^{-6}$	30.0	88.2
$\beta_{PA} = 7000$ $[bar]$	$1.1885 \cdot 10^{-5}$	$3.6080 \cdot 10^{-6}$	30.0	88.2
$\beta_{PA} = 8000$ $[bar]$	$1.0351 \cdot 10^{-5}$	$3.6080 \cdot 10^{-6}$	30.2	88.2
$\beta_{PA} = 9000$ $[bar]$	$9.2257 \cdot 10^{-6}$	$3.6080 \cdot 10^{-6}$	30.0	88.2

Table 8.2: Controller gains.

The calculated controller gains have been plotted in figure 8.7 and 8.8. It can be seen that an approximation has been constructed, and the approximation is implemented in the simulink model.

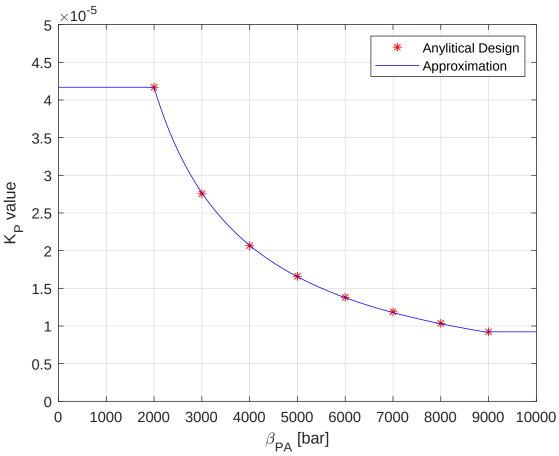

Figure 8.7: K_P values as a function of β_{PA}.

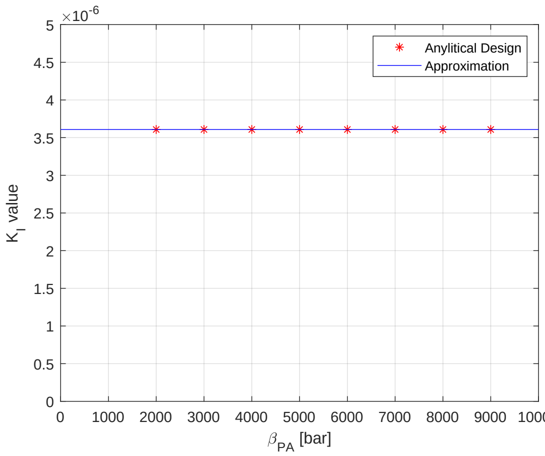

Figure 8.8: K_I values as a function of β_{PA}.

8.4 Trajectory and Controller Testing - Simulation

In order to test the designed pressure controllers then first a step input for the motor speed is given to the model. When the pressure has settled then the POCV's are closed and the reference for the motor speed is set equal to 0 RPM. Hereby the pressure drops and after 5 seconds the pressure controllers are activated. The procedure can be seen in figure 8.9.

In figure 8.10 the simulation results can be seen. It has been decided to test the pressure controllers at both low and high pressures in order to investigate the impact of the changing controller gains for the gain schedule. It can be seen that all 4 controllers are stable.

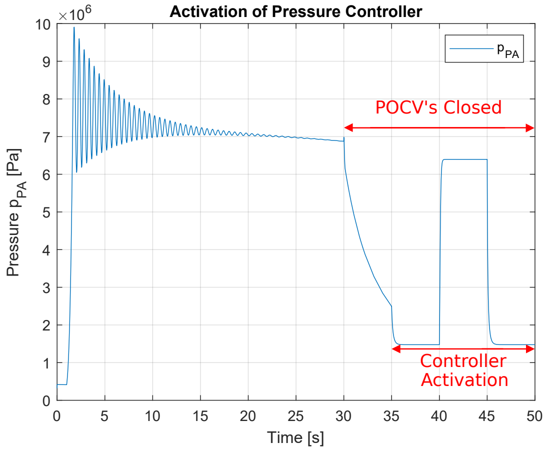

Figure 8.9: Activation of the pressure controllers.

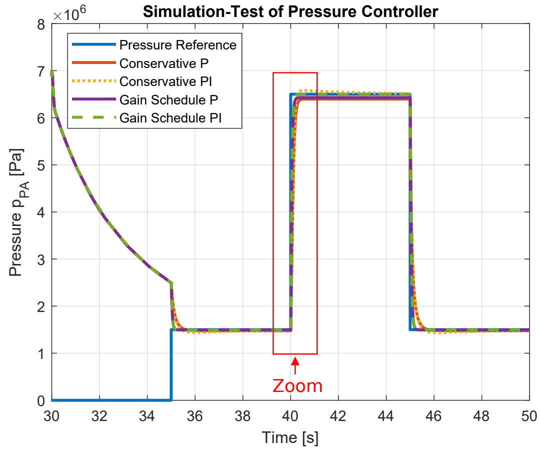

Figure 8.10: Step responses for the controllers.

In figure 8.11 it can be seen that the conservative controllers have a slower response compared to the gain scheduling controllers.
Furthermore, the step responses for the 2 gain schedule controllers are similar. However, it can be seen that the PI-controller reaches 0 steady state error, and the P-controller reaches almost 0 steady state error.

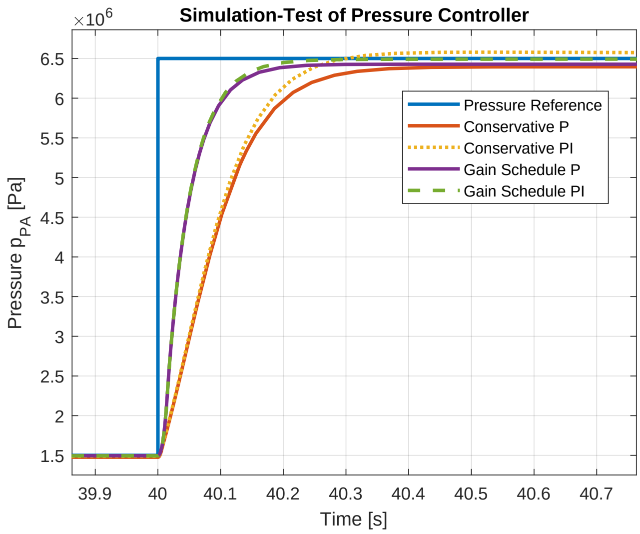

Figure 8.11: Step response - Zoom.

9 | Controller Test - Simulation

In this chapter the pressure controllers and the position controllers are tested together. This means that the controller choice and the trajectory are going to switch doing the trajectory.

9.1 Trajectory and Controller Choice - Switching

In figure 9.1 an overview of the different time intervals can be seen. Each time interval contains a different controller choice and trajectory. Two different switching conditions have been tested in the simulation.

- Time Condition
- State Condition

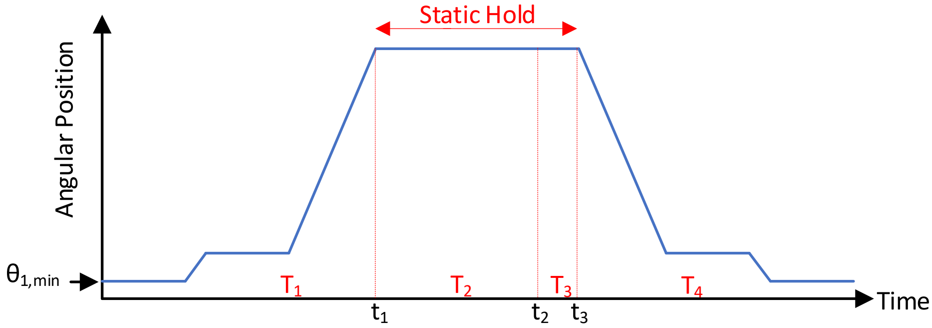

Figure 9.1: Schematic used to show the different time intervals.

Time Switching

If time is chosen as the switching condition then the switching conditions can be seen in table 9.1. The time conditions are implemented in the Simulink model using logic and clock-values. This implementation method is also applicable in the experimental setup.
An advantage with the time conditions is that it is easy to implement. However, a drawback with the time conditions is regarding safety. If for example the pressure is not build up during time interval T_3 then the trajectory will still switch into a position trajectory in T_4. This could potentially be a dangerous situation because hereby the crane will drop and begin to oscillate if the pressure is not build up during T_3.

Intervals	Controller Choice	Trajectory Reference	Condition	Reference POCV
T_1	Position	Position Trajectory	$\mathrm{t} < \mathrm{t}_1$	Open
T_2	Internal Model Control	0 rad/s	$\mathrm{t}_1 \leq \mathrm{t} < \mathrm{t}_2$	Closed
T_3	Pressure	Pressure Trajectory	$\mathrm{t}_2 \leq \mathrm{t} < \mathrm{t}_3$	Closed
T_4	Position	Position Trajectory	$\mathrm{t} \geq \mathrm{t}_3$	Open

Table 9.1: Table showing the different controller choices and references.

State Switching

If states are chosen as the switching parameters then the switching conditions can be seen in table 9.2. The AHI stands for Active Holding Input, and is an external input for the logic. This means that a person can active the passive holding operation during the trajectory. Furthermore, by applying the state conditions then the crane does not need a predefined trajectory. The operating person will however experience a delay of approximately 0.3 seconds in the steering after the passive holding operating. The reason for this is that the the pressure difference between p_A and p_{PA} needs to be less than 2 bar, and the pressure settlement takes approximately 0.3 seconds.

Controller Choice	Trajectory Reference	Condition	Reference POCV
Position	Position Trajectory	Else Condition	Open
Internal Model Control	0 rad/s	$\theta_{1,error} < 0.002$ rad AHI = 0	Closed
Pressure	Pressure Trajectory	$p_{PA,error} > 2$ bar AHI = 1	Closed

Table 9.2: Table showing the different controller choices and references.

Comparison between Switching Methods

In order to see the difference between the switching methods then a position comparison and a pressure comparison can be seen in figure 9.2 and 9.3. It can be seen that the outcome of the two switching methods are similar to each other, and both could potentially be implemented on the experimental setup.
It should be noted that the used position controller is a P-controller without HPPF and with VFF.

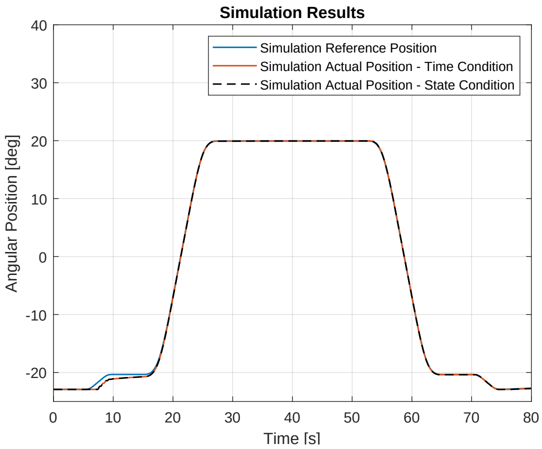

Figure 9.2: Position comparison.

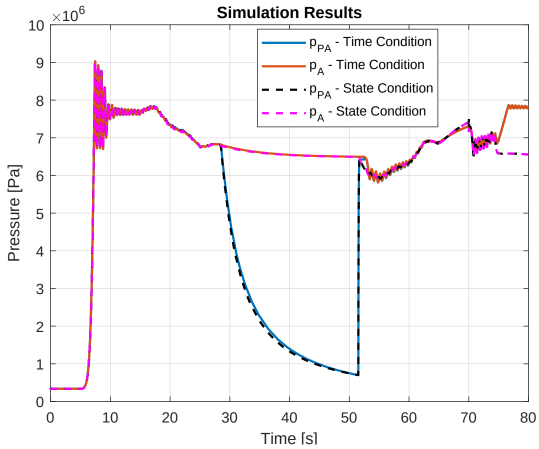

Figure 9.3: Pressure comparison.

The following sections describe the controller-testing, and it is chosen to base the trajectory and controller choices based on the state conditions. This decision is made because (as explained earlier) the state conditions provide a more safe operation of the crane.

9.2 Controller Tests

9.2.1 Overview of Simulation Tests

A series of simulation tests have been performed in order to show the impact of the different controller choices. An overview is seen in table 9.3.

Test Number	Trajectory	Position Controller	Pressure Controller	HPPF
1	1000 RPM	P	P - GS	Off
2	1000 RPM	P	P - GS	On
3	1000 RPM	P	Off	On
4	1000 RPM	P, PI GM, PI no OS, P-lead	P - GS	On
5	2800 RPM	P, PI GM, PI no OS, P-lead	P - GS	On

Table 9.3: Overview of simulation tests.

9.2.2 Test 1 and Test 2

In order to study the effect of the high-pass filtered pressure feedback then the 2 designed P-controllers are tested against each other. The results can be seen in figure 9.4 and 9.5. It can be seen that both of the designed P-controllers are capable of following the trajectory. However, it can also be seen that the pressure oscillations are reduced with HPPF.

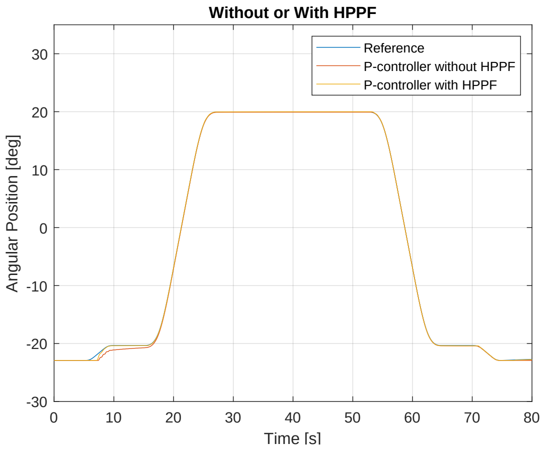

Figure 9.4: Position comparison.

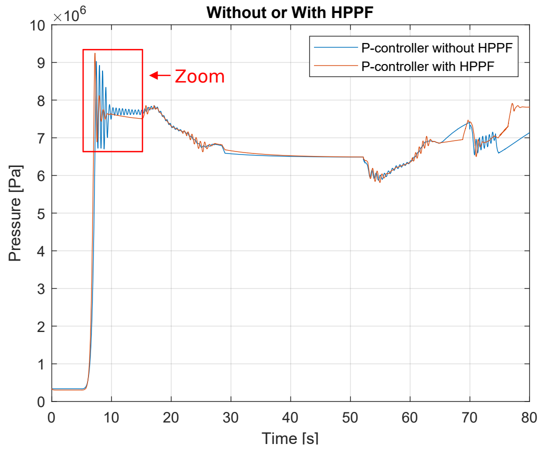

Figure 9.5: Pressure p_A comparison.

In figure 9.6 it can be seen that the HPPF damps the pressure oscillations. Based on this it is decided only to implement controller designed with the HPPF on the experimental setup.

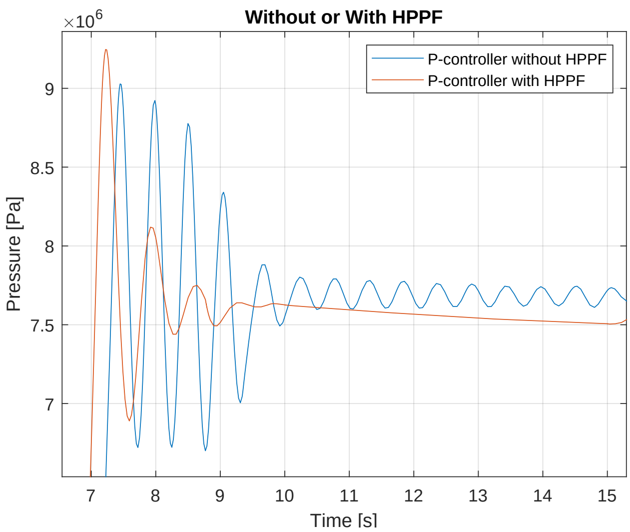

Figure 9.6: Zoom of the pressure.

9.2.3 Test 2 and Test 3

In order to study the effect of the designed pressure controller then the trajectory is simulated without and with the pressure controller. The simulation results for the pressure can be seen in figure 9.7 and 9.8. It can be seen that without the pressure controller the pressure oscillates when the POCV's are opened, and this also results in an undesired position drop for the cylinder position.
Therefore it is concluded that a pressure controller should be implemented along with a position controller in the experimental setup.

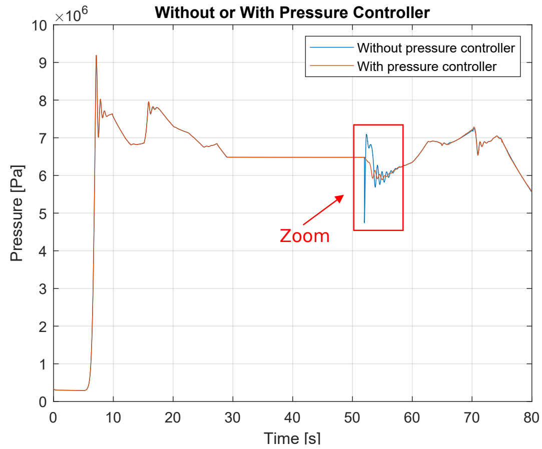

Figure 9.7: Pressure p_A comparison.

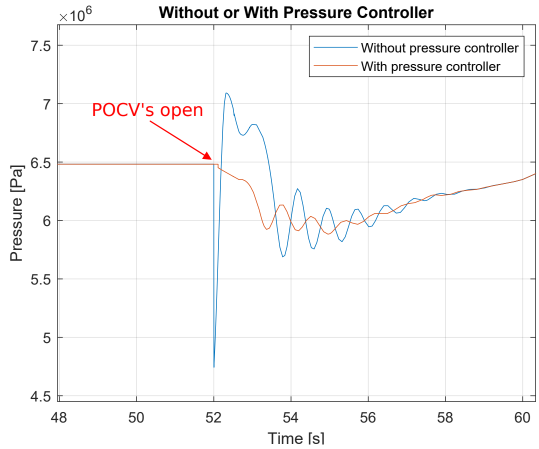

Figure 9.8: Pressure p_A comparison - Zoom.

9.2.4 Test 4 and 5

The controllers have been tested with the state switching conditions and the results can be seen in figure 9.9. In the trajectory seen in figure 9.9 the maximum motor speed is approximately 1000 RPM. In order to test the controllers then an additional trajectory has been created. The trajectory can be seen in figure 9.10, and the maximum motor speed is approximately 2800 RPM. It can be seen that all 4 controllers are capable of following the trajectory precisely.

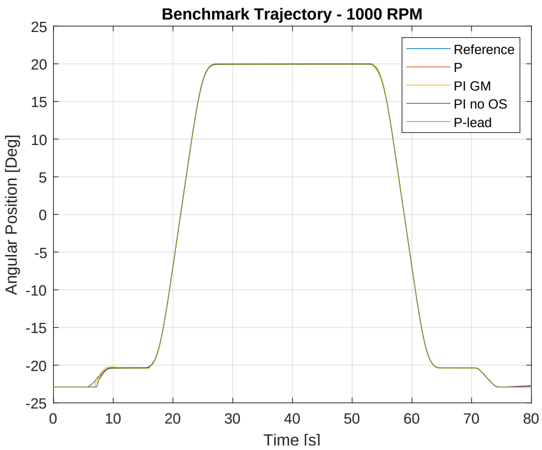

Figure 9.9: Position trajectory - 1000 RPM.

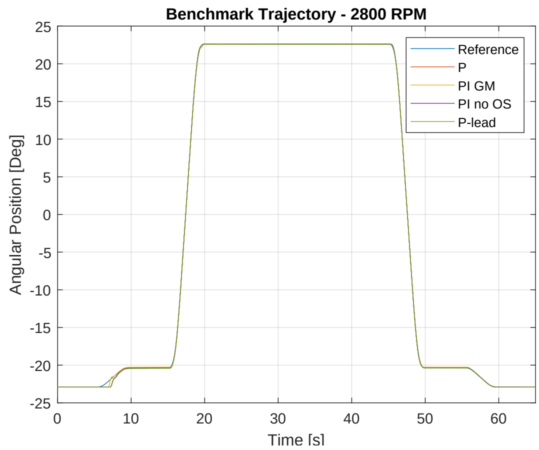

Figure 9.10: Position trajectory - 2800 RPM.

In order to further investigate the controllers then the cylinder pressure in chamber A has been plotted. The pressure can be seen in figure 9.11 and in figure 9.12. It can be seen that pressure tends to oscillate more for the PI-controller with a phase margin of 40^o. It is therefore chosen not to implement this controller on the experimental setup.

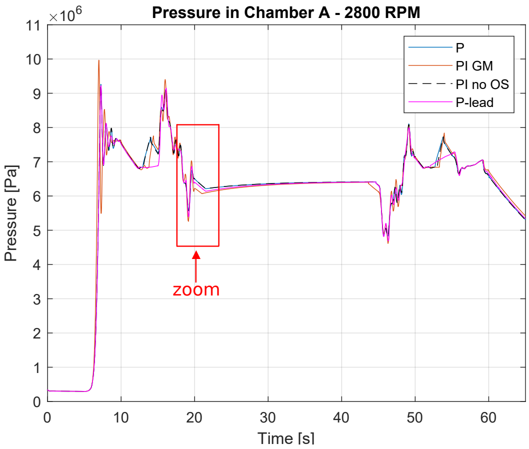

Figure 9.11: Pressure in chamber A - 2800 RPM.

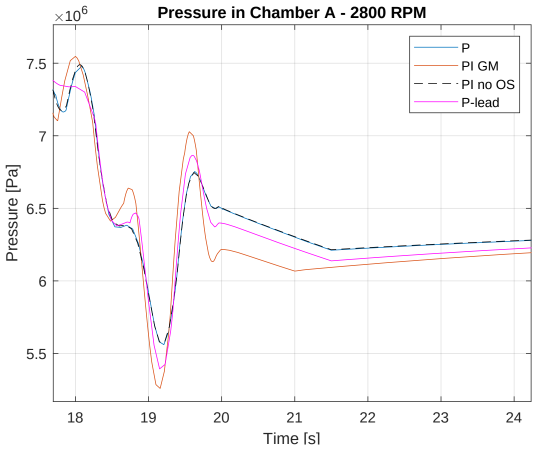

Figure 9.12: Zoom of pressure - 2800 RPM.

9.3 Preliminary Conclusions

Test 1 and 2
Based on the simulation results from test 1 and test 2, it is concluded that the HPPF damps the pressure oscillations significantly. It is shown in figure 9.6 that with HPPF pressure oscillations occur for approximately 3 seconds. Without HPPF the pressure oscillations do not stop within the shown time frame. It is therefore concluded that the HPPF works as intended.

Test 2 and 3
Based on the simulation results for test 2 and 3, it is concluded that the pressure controller reduces the pressure drop when the when the pressure controller is implemented. It can be seen in figure 9.8 that if the pressure controller is implemented then no pressure drop is present. In contrast, if the pressure controller is not implemented then the pressure drops 17 bar. It is therefore concluded that the pressure controller works as intended.

Test 4 and 5
Based on the simulation results for test 4 and 5, it is concluded that all of the designed position controllers are capable of following both the 1000 RPM and 2800 RPM trajectory. However, it is also seen in figure 9.12 that the amplitude for the pressure oscillations are higher for the PI controller designed with GM $\approx 40^o$. For this reason it is decided not to implement this controller.

10 | Experimental Results

10.1 Initial Pressure Controller Tests

In order to investigate the impact of the pressure controller and the HPPF then 6 different tests have been performed. The cylinder position reference for the 6 tests can be seen in figure 10.1, and a description of the 6 tests can be found in table 10.1. The same position and pressure controllers are used for all 6 experiments. It should be noted that the used position controller is chosen such that the closed loop is stable with and without HPPF. Therefore the position tracking is not accurate.

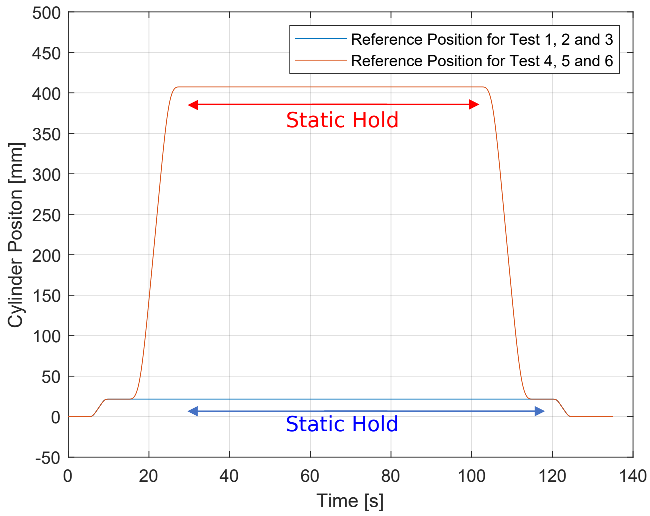

Figure 10.1: Reference position for pressure controller tests.

Test Number	Cylinder Position	Pressure Controller	HPPF
Test 1	Low	Off	Off
Test 2	Low	On	Off
Test 3	Low	On	On
Test 4	High	Off	Off
Test 5	High	On	Off
Test 6	High	On	On

Table 10.1: Overview of the 6 experiments.

10.1.1 Test 1, 2 and 3

In these experiments the static hold time has been increased to 88 seconds in order to make sure that the pressure p_{PA} settles near the accumulator pressure. This can be seen in figure 10.2. It can be seen that the leakage varies a lot. In order to see the impact from the pressure controller and the HPPF then 2 zooms have been conducted.

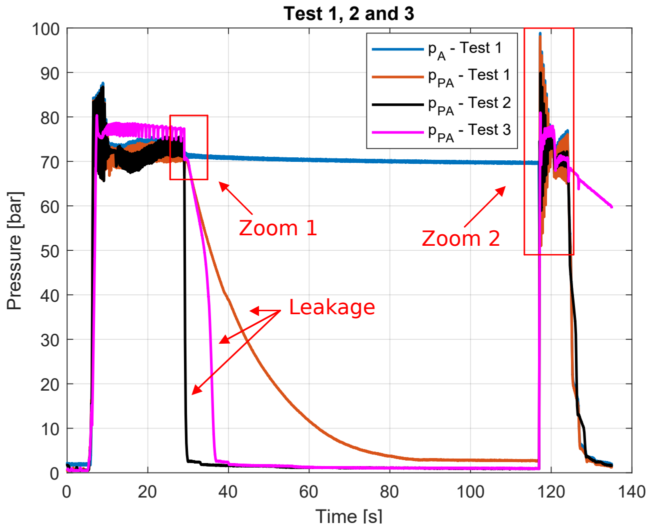

Figure 10.2: Pressure measurements.

In figure 10.3 it can be seen that the pressure p_A does not drop much when the POCV's are closed. In figure 10.4 the pressure p_{PA} can be seen when the POCV's are reopened, and it can be seen that the pressure oscillations are significant. It can be seen that adding the pressure controller reduces that amplitude of the pressure oscillations, and that the HPPF damps the systems.

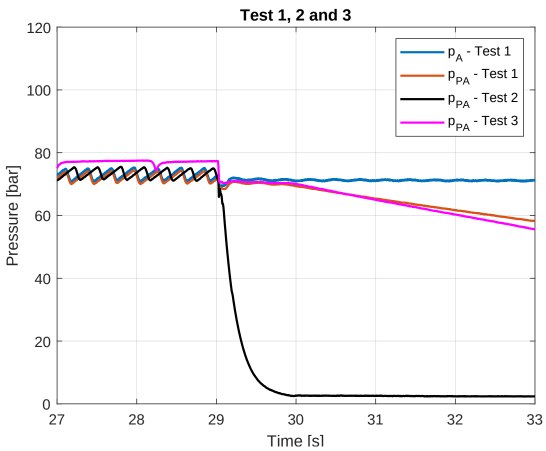

Figure 10.3: Pressure measurements - Zoom 1.

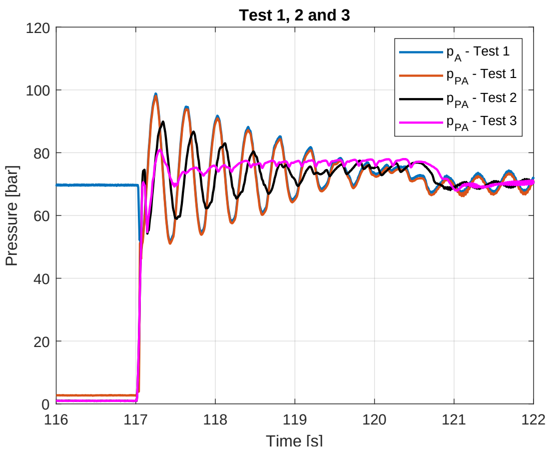

Figure 10.4: Pressure measurements - Zoom 2.

The same tendencies for the pressure can be seen in measurements for the cylinder position. In figure 10.5 it can be seen that 2 zooms have been conducted, and the 2 zooms can be seen in figure 10.6 and 10.7.

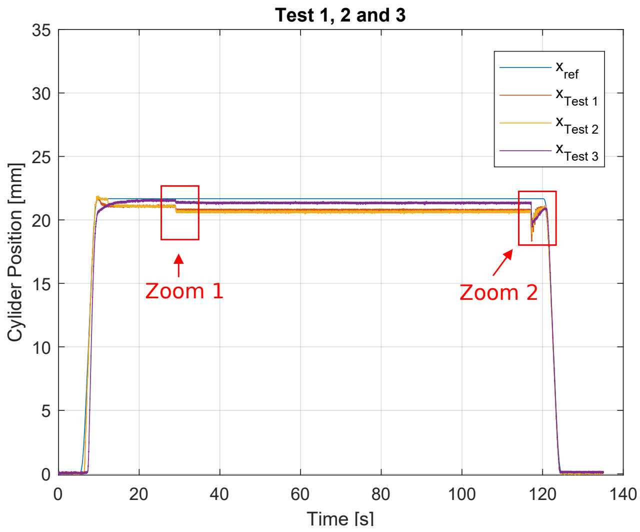

Figure 10.5: Measured position for pressure controller tests.

In figure 10.6 it can be seen that the cylinder position only drops approximately 0.2 mm when the POCV's are closed. However, as seen in figure 10.7 then the cylinder drops approximately 2 mm when the POCV's are reopened. It can be seen that pressure controller reduces the the drop, but that the cylinder still drops significantly.

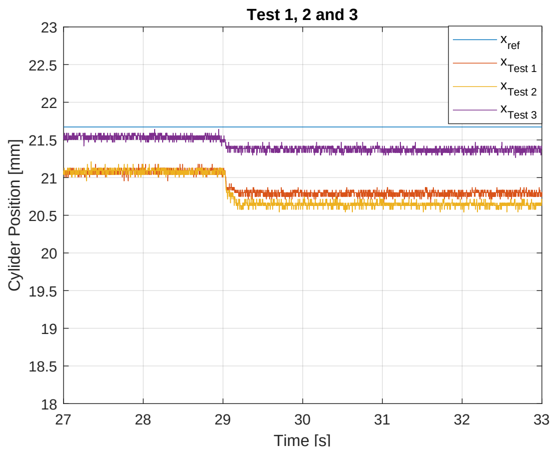

Figure 10.6: Measured position - Zoom 1.

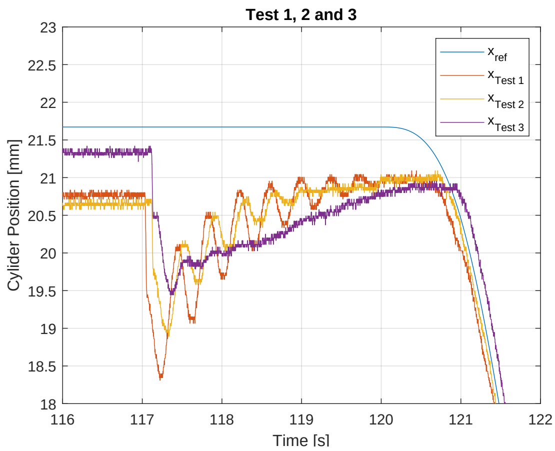

Figure 10.7: Measured position - Zoom 2.

Experimental Comparison

In order to see how different volumes affect the pressure oscillations after the static holding then a comparison between the experiments have been conducted. The results can be seen in 10.8 and 10.9. It can be seen that when the static holding is carried out in a high position, the pressure oscillations are smaller compared to when the static holding is carried out in a low position.

It should be noted that the time axes for the high holding experiments have been shifted be 17.5 seconds in order to compare the pressure oscillations. Furthermore, the comparison between test 1 and 4 is not shown because it yields the same results as seen in figure 10.8 and 10.9.

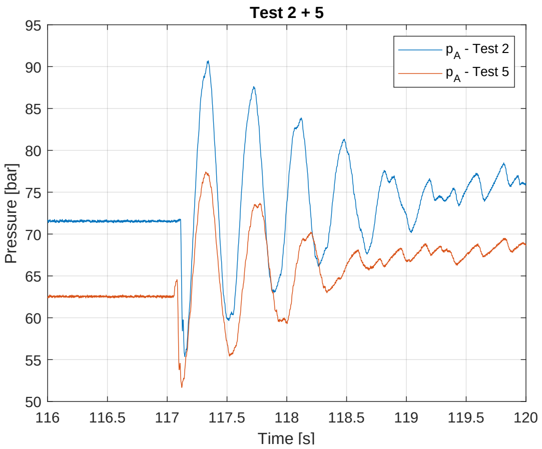

Figure 10.8: Comparison between test 2 and 5.

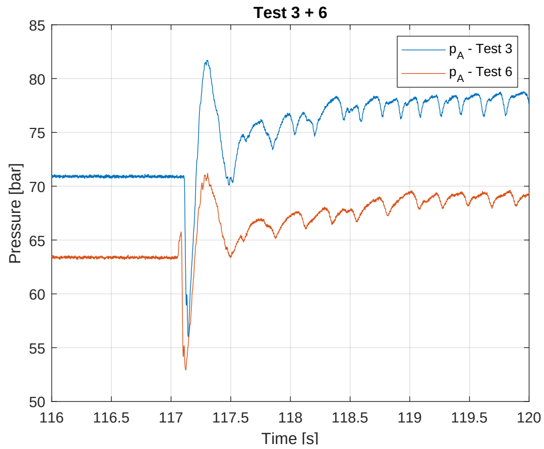

Figure 10.9: Comparison between test 3 and 6.

Based on the figures above then it is concluded that the volumes have an impact on the pressure oscillations. A reason for this could be that the eigenfrequency decreases if the volume increases.
Furthermore, it is concluded that the developed Simulink model is not accurate enough because it does not simulate the pressure oscillations after the static holding. A hypothesis for the deviation in the Simulink model is given in the following subsection.

10.1.2 Hypothesis for Model Deviation

The hypothesis for the model deviation is the volume $V_{3/2}$ seen in figure 10.10 and in 10.11. The volume is not included in the Simulink model, and in the following the impact of the volume is explained.
As it is shown in the pressure controller experiments, the pressure oscillations are very small when the POCV's are closing. The reason for this can be seen in figure 10.10. In figure 10.10 the pressure $p_{3/2}$ is high, and the 3/2 valve changes position fast. Hereby only a small pressure drop in p_A is experienced when the 3/2 valve changes position.

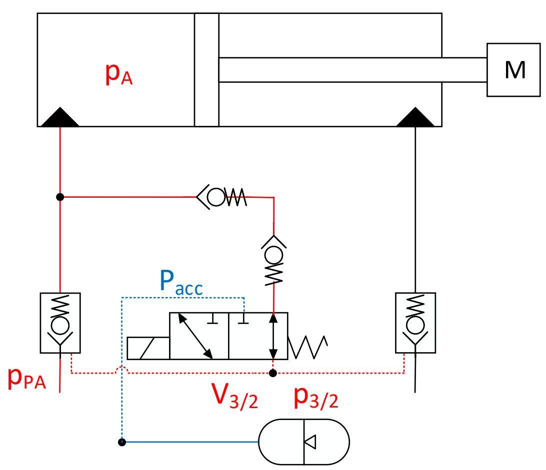

Figure 10.10: POCV's opened.

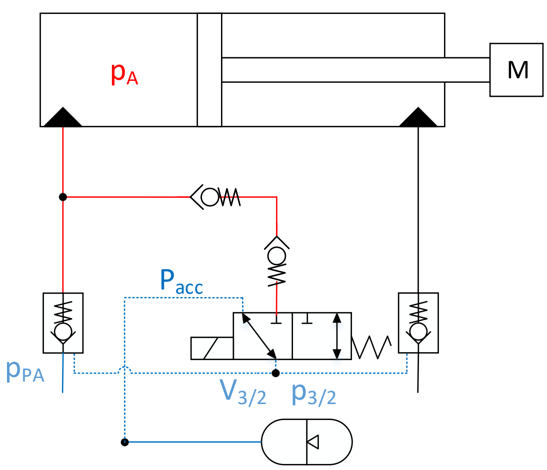

Figure 10.11: POCV's closed.

In contrast, it is seen in the experiments that when the POCV's are opening, the pressure oscillations are bigger. The reason for this can be seen in figure 10.11. When the POCV's are opening then the pressure $p_{3/2}$ is low, and the volume $V_{3/2}$ is "added" to the cylinder volume. Hereby the pressure p_A is going to drop (even though the pressure p_{PA} is build up) when then 3/2 switches position.

Based on the explanation above it is concluded that the current approach for reducing the pressure oscillations is not satisfactory (the position drop is above the 1mm limit as stated in the problem statement). The designed pressure controllers increase the pressure p_{PA} before the re-opening of the POCV's, and it is shown that is reduces the pressure oscillations. However, the volume $V_{3/2}$ is not taken into account, and this could explain why the pressure oscillations are still present despite the pressure controller.

10.1.3 Gain Reduction

It is decided to reduce the pressure controller gain by 30% in order to avoid the overshot seen in figure 10.12. A reason for the overshot could be the impact of the implementation (discrete-time-system), but this has not been investigated further. It is decided not to implement the gain schedule pressure controller in the experimental setup because it is believed that the controller would result in an even bigger overshot and because of time limitations. However, a gain schedule could controller could still potentially work satisfactory if the gains are reduced.

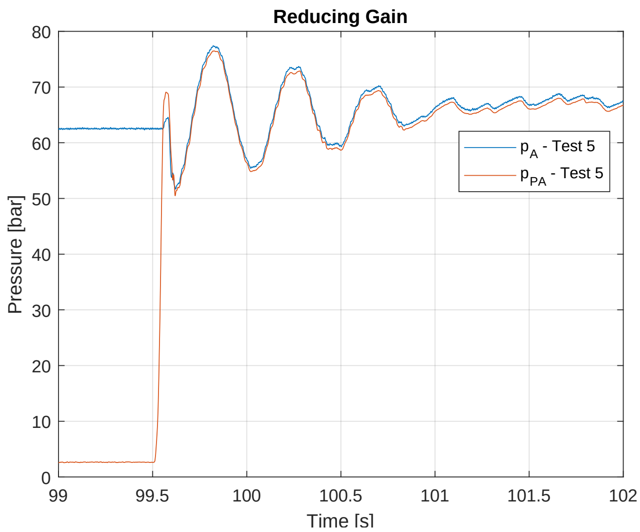

Figure 10.12: Measurements showing reason for gain reduction.

10.2 Combined Position and Pressure Controller Tests

The designed position controllers have been implemented and tested in the experimental setup. Table 10.2 and 10.3 provide an overview for the 6 experiments.

Test Number	Trajectory	HPPF, VFF and Pressure Controller	Position Controller
7	1000 RPM	On	P
8	1000 RPM	On	PI
9	1000 RPM	On	P-lead

Table 10.2: Overview of controller test 7, 8 and 9.

Test Number	Trajectory	HPPF, VFF and Pressure Controller	Position Controller
10	2800 RPM	On	P
11	2800 RPM	On	PI
12	2800 RPM	On	P-lead

Table 10.3: Overview of controller test 10, 11 and 12.

10.2.1 Test 7, 8 and 9 - Measurements

The result can be seen in figure 10.13. The tested trajectory have a limit of approximately 1000 RPM for the motor speed. It can be seen that the reference is followed precisely.

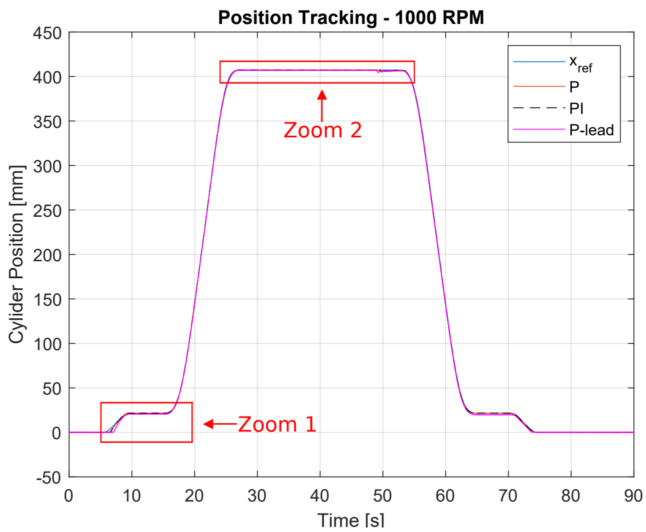

Figure 10.13: Measured position - Test 7, 8 and 9.

Based on figure 10.14 and 10.15 it can be seen that the P-lead controller does not track the reference as precisely as the 2 other controllers. This was expected based on the simulations in section 7.6. Furthermore, it can be seen that the experimental results for the P and PI controller are very similar. This is also expected because $K_I << K_P$.

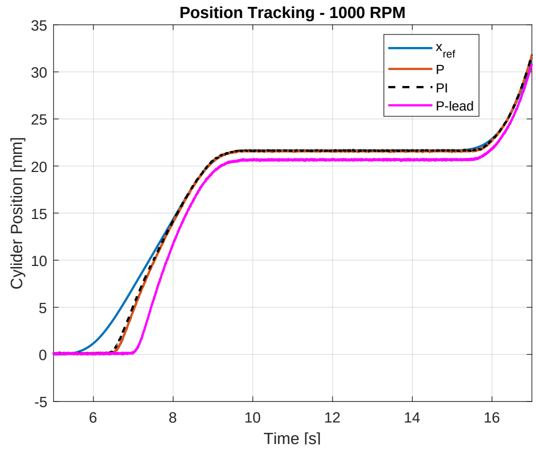

Figure 10.14: Measured position - Zoom 1.

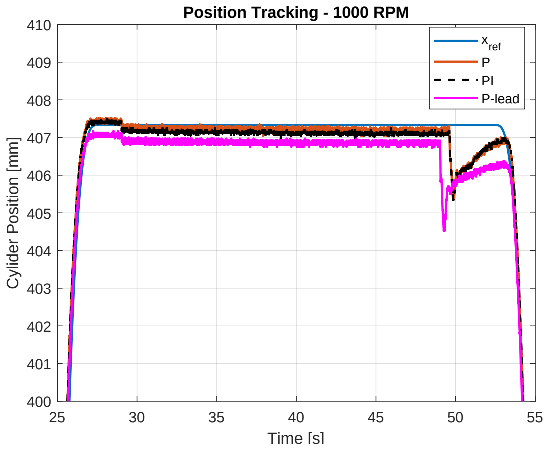

Figure 10.15: Measured position - Zoom 2.

10.2.2 Comparison between Model and Test 7

In this subsection the differences between the Simulink model and the experimental results are explained. The measured and simulated cylinder position can be seen in figure 10.16 and figure 10.17. It can be seen that the the simulated and measured position correspond well with each other. However, as seen in the zoom then the position drop seen in figure 10.17 at 49.5 seconds is not seen in the simulation. The reason for this has been explained in section 10.1.1.

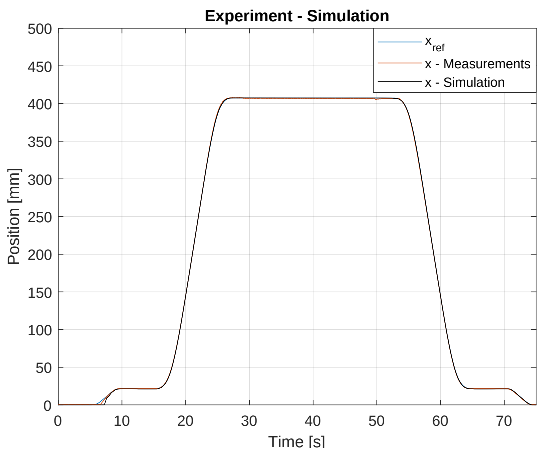

Figure 10.16: Position comparison.

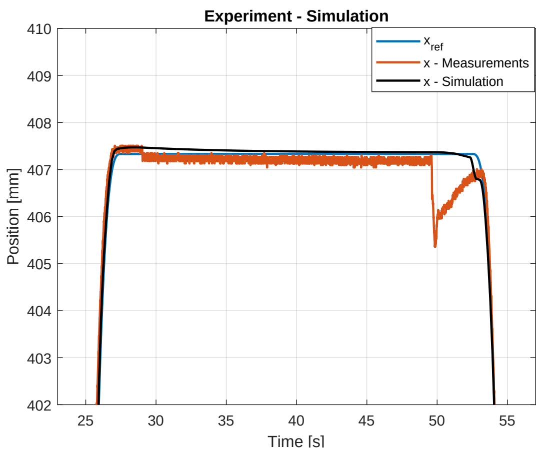

Figure 10.17: Position comparison - Zoom.

The position drop seen in figure 10.17 can also be seen in the measured pressures p_A and p_{PA}. This can be seen in figure 10.18 and 10.19. It can be seen that the Simulink model describes the pressures accurately except for the re-opening of the POCV's at 49.5 seconds.

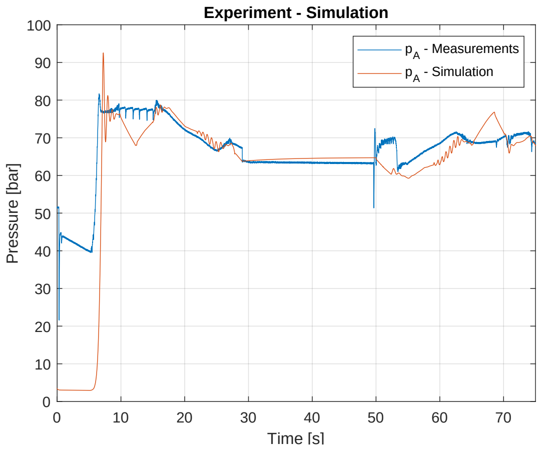

Figure 10.18: Position.

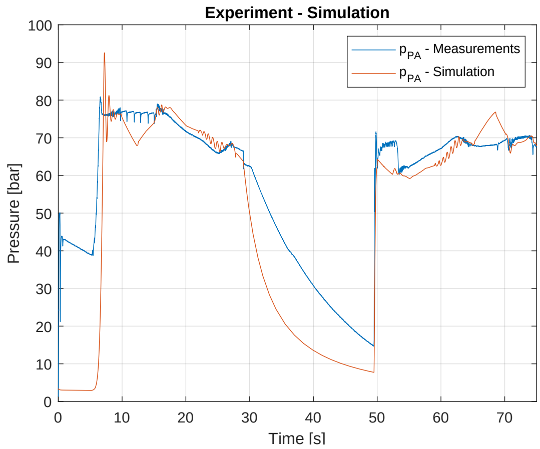

Figure 10.19: Position - Zoom.

The pressures p_B and p_{acc} are seen in figure 10.20 and figure 10.21. It can be seen that the simulated data corresponds well with the measured data.

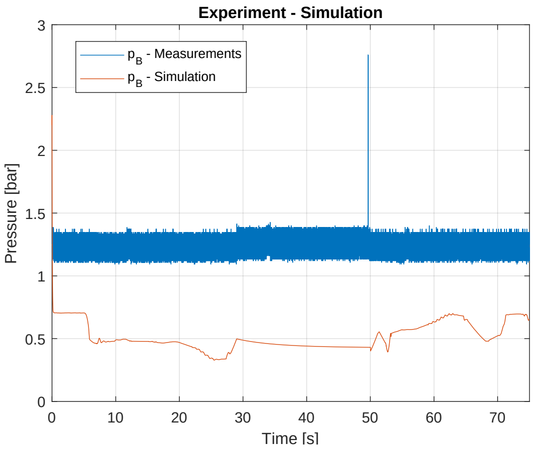

Figure 10.20: Cylinder pressure - Chamber B.

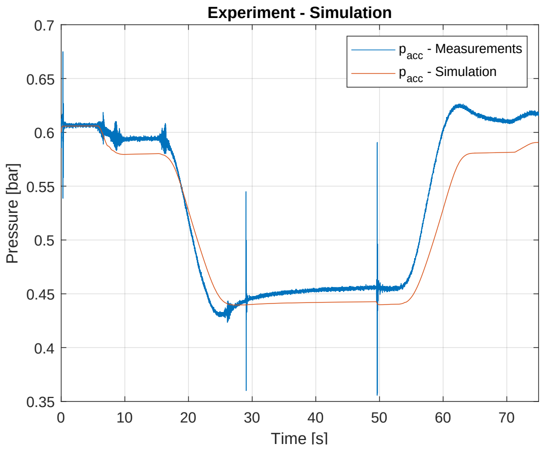

Figure 10.21: Accumulator pressure.

The measured and simulated motor speed can be seen in figure 10.22, and it can be seen that the measured and simulated data are similar.
Lastly, the velocity reference for the cylinder is plotted in order to show the linear velocity of the cylinder.

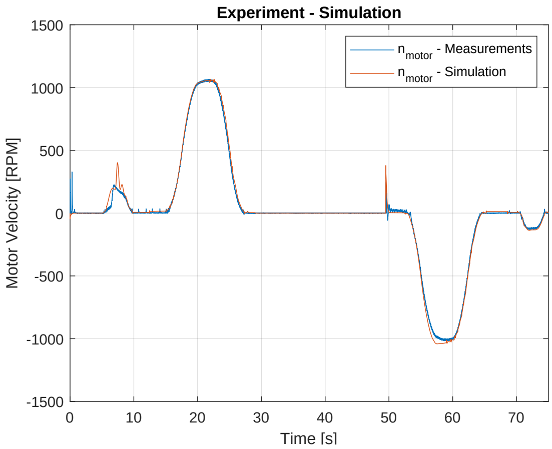

Figure 10.22: Motor speed.

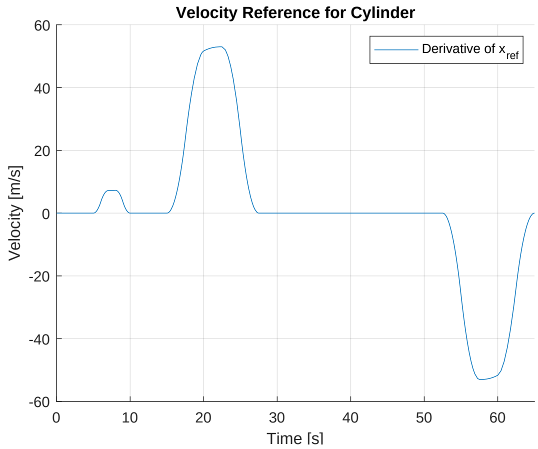

Figure 10.23: Reference speed for cylinder.

Based on the above figures it is concluded that the Simulink model is accurate, but that the volume $V_{3/2}$ seen in figure 10.10 and figure 10.11 should be implemented in the Simulink model in order to improve the accuracy.

10.2.3 Test 10, 11 and 12 - Meassurements

The designed controllers have also been tested with the 2800-RPM trajectory. The results can be seen in figure 10.24 and 10.25. It can be seen that the controllers are capable of following the trajectory precisely. However, an overshot at approximately 3 mm is present at 20 seconds. This overshot was not seen in the Simulink model, and it is believed that the reason for this is the modelled torsion spring. A previous project has included 9 torsion springs in order to describe the deflection of the beam [8].
In this project it is chosen only to include a single torsion spring, and this could explain why the overshot is not seen in the simulated results. It is chosen that including 9 torsion springs in the Simulink model is beyond the scope of this project, and thus the deviation is deemed acceptable. The overshot could most likely be reduced by adjusting the controller gains, but due to time limitations then this has not be done.

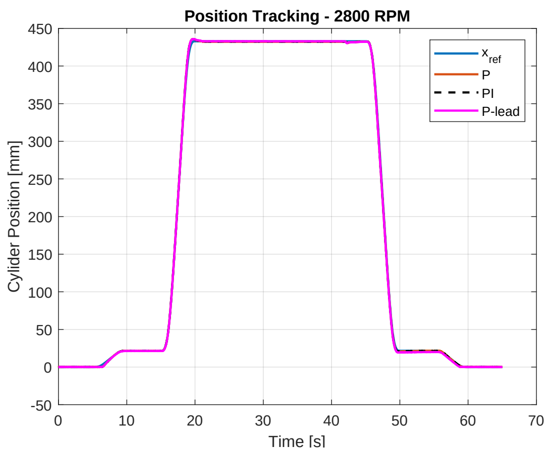

Figure 10.24: Measured cylinder position.

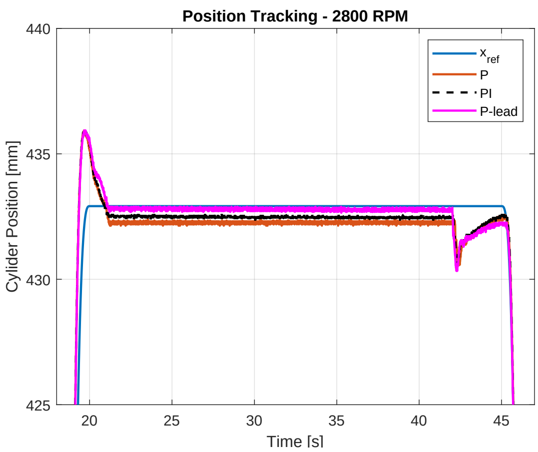

Figure 10.25: Measured cylinder position - Zoom.

The measured and simulated motor speed are seen in figure 10.26, and it can be seen that

the measured data corresponds well with the simulated data.
Lastly, the reference speed for the cylinder velocity is seen. It can be seen that linear cylinder velocity almost reaches 150 mm/s.

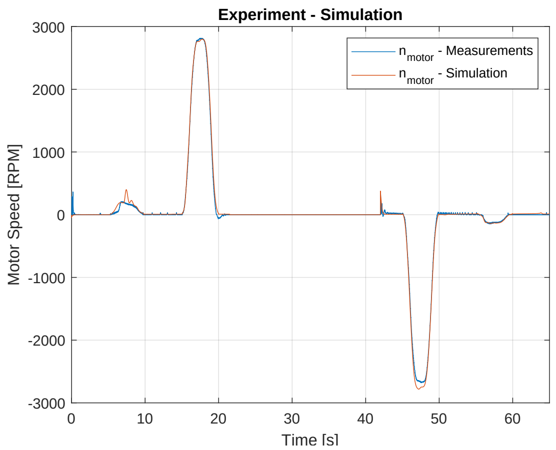

Figure 10.26: Motor speed.

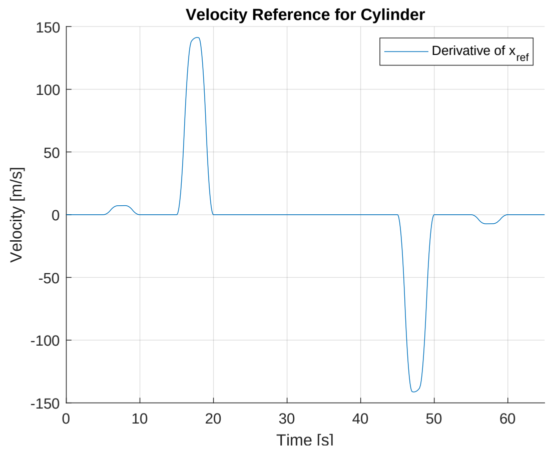

Figure 10.27: Reference speed for cylinder.

10.3 With or Without Pressure Controller

In order to investigate if a pressure controller is needed if HPPF is activated then 2 experiments have been conducted. The two experiments can be seen in table 10.4.

Test Number	Controller Choice	HPPF	VFF	Pressure Controller
13	P	On	On	On
14	P	On	On	Off

Table 10.4: Difference between the two experiments.

The position trajectory can be seen in figure 10.28 and 10.29. It can be seen that the pressure controller reduces the position drop when the POCV's open.

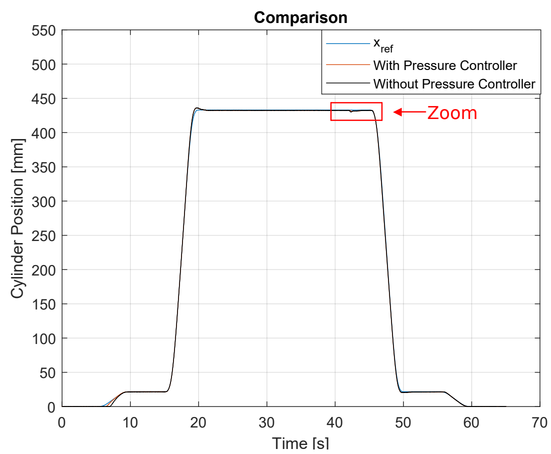

Figure 10.28: Measured position.

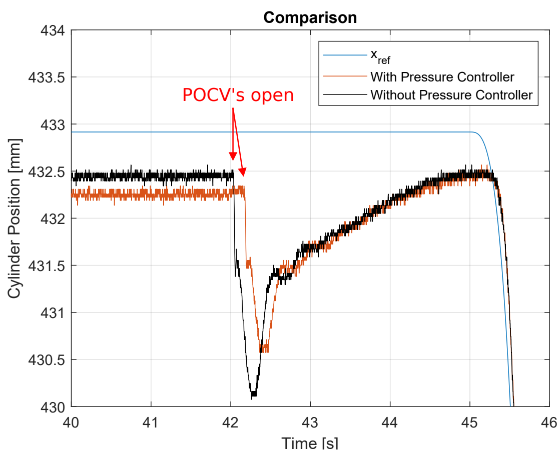

Figure 10.29: Measured position - Zoom.

The reduction in the position drop can also be seen in the pressures p_A and p_{PA}. In figure 10.30 a zoom of the two pressures can be seen when pressure controller is activated. It can be seen that the pressure p_A drops 11.0 bar when the POCV's are opened.
In contrast, in figure 10.31 it can be seen the pressure p_A drops 14.3 bar when the pressure controller is not activated. It is therefore concluded that the pressure controller works but improvements should be made in order to decrease the position drop.

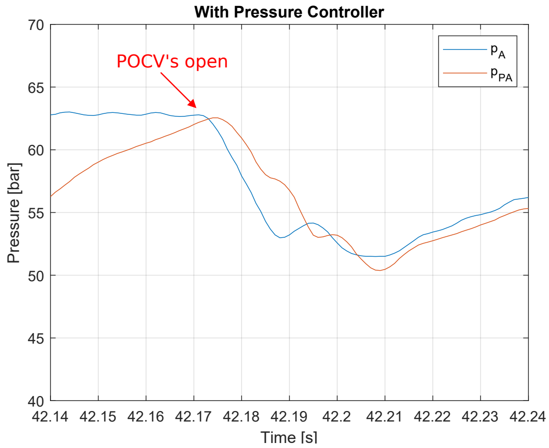

Figure 10.30: Test 13 - Zoom.

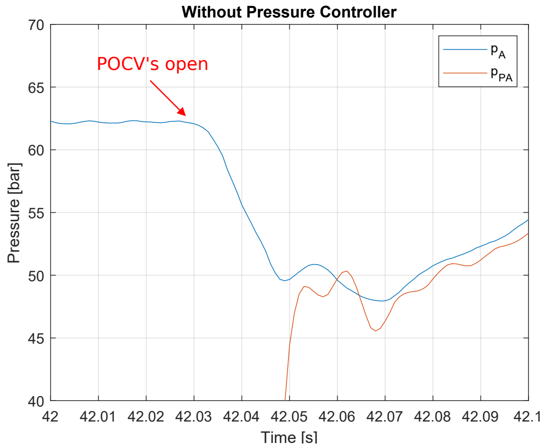

Figure 10.31: Test 14 - Zoom.

10.4 Experimental Conclusions

Test 1-6
Based on the experimental results from test 1-6, it is concluded that the designed HPPF damps the pressure oscillations significantly. In figure 10.4 it is shown that the pressure only oscillates for 0.5 seconds with HPPF. In contrast, it can be seen that without HPPF the pressure oscillations continues to oscillate until a new position reference is given.
Furthermore, based on figure 10.4 it is shown that the amplitude of the pressure oscillations is reduced if the pressure controller is activated.
It is therefore concluded that the HPPF and the pressure controller work as intended.

Test 7, 8 and 9
In order to compare the performance of the different position controllers then the position error during the 1000-RPM trajectory has been plotted in figure 10.32 and the average error can be seen in figure 10.33.
Based on figure 10.32 it can be seen that highest position error is 7mm, and therefore the position error is kept within the limitations stated in the problem statement. Furthermore, the average error is kept below 1mm, and therefore all the implemented position controllers are capable of fulfilling the demands stated in the problem statement.
However, it can be seen that when the POCV's are opened, the position drops above the 1mm as stated in the problem statement. The hypothesis for this position drop is explained in section 10.1.2, and both the Simulink model and the controller strategy should be improved. These improvements are explained in chapter 11.

Figure 10.32: Position error graph.

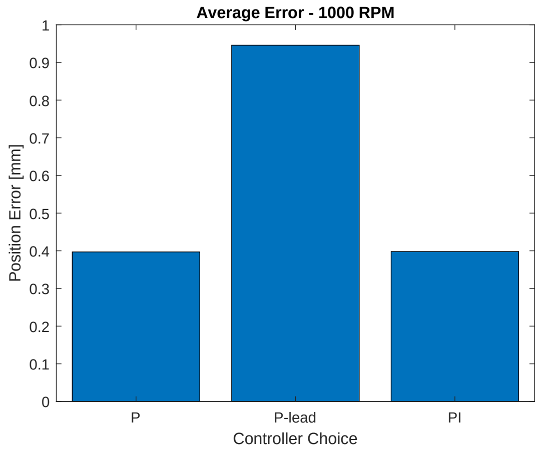

Figure 10.33: Average error.

Test 10, 11 and 12

The position error for the 2800 RPM trajectory is seen in figure 10.34, and the average error can be seen in figure 10.35. The conclusions for these experiments are very similar to the conclusions for test 7, 8 and 9, and therefore they are not repeated here.

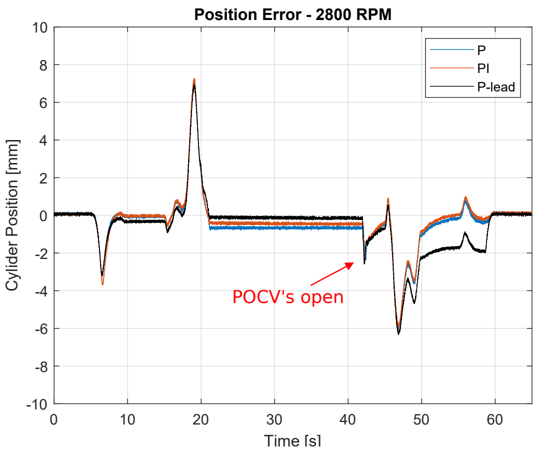

Figure 10.34: Position error graph.

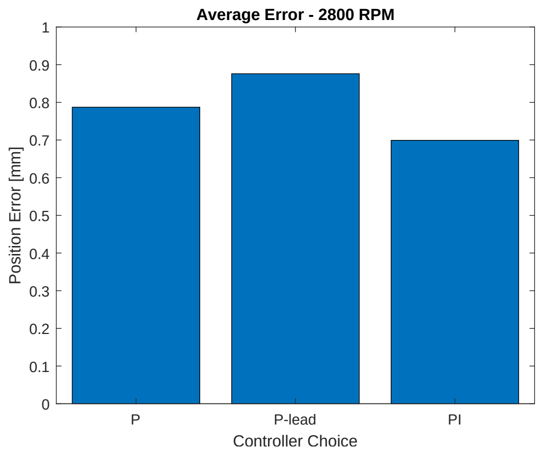

Figure 10.35: Average error.

Test 13 and 14

Based on the experimental results from test 13 and 14, it is concluded that the pressure controller reduces pressure drop when the POCV's are opened even though the HPPF is activated. In figure 10.30 it can be seen that the pressure p_A drops 11.0 bar when the POCV's are opened and the pressure controller is activated. In contrast, it can be seen in figure 10.31 that the pressure p_A drops 14.3 bar when the pressure controller is not activated.

It is therefore concluded that the pressure controller works as intended but improvements should be made in order to decrease the position drop even further.

11 | Improvements

In chapter 10 it is shown that the Simulink model is inaccurate when the POCV's are reopened. The hypothesis for this inaccuracy is that the volume $V_{3/2}$ seen in figure 10.10 and 10.11 is not included in the model. In this chapter the volume $V_{3/2}$ and the 3/2-valve is included in the Simulink model and compared with the experimental data.
Furthermore, two new control schemes are developed such the the position drop after the static load holding can be improved.

11.1 Model Modifications

It is decided to move the modelling of the 3/2 valve to appendix I such that this chapter only contains simulation and experimental results. However, the the block diagram representation for the Simulink model modifications is seen in figure 11.1.

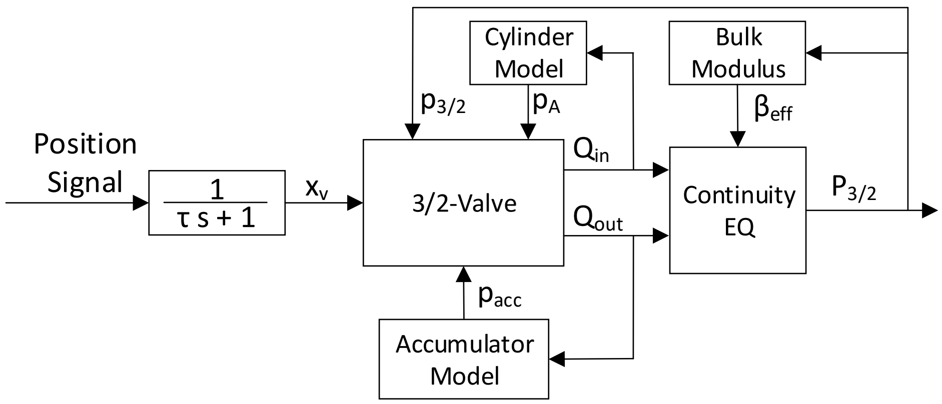

Figure 11.1: Block diagram representation for the model modifications.

11.2 Comparison: Modified Model and Experiments

In figure 11.2 the cylinder position can be seen for a 1000 RPM trajectory. The zoom in figure 11.3 shows that the Simulink model now simulates the position drop when the POCV's are opened.

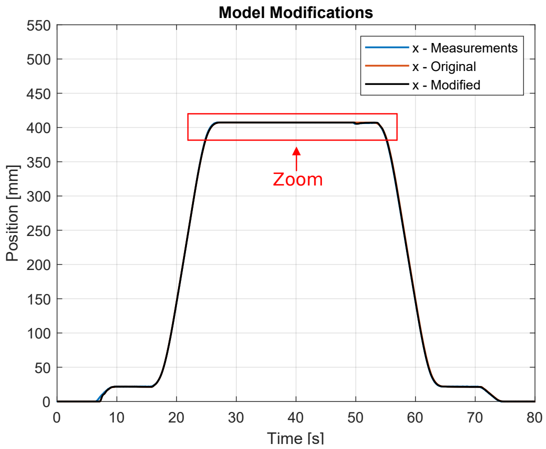

Figure 11.2: Cylinder position.

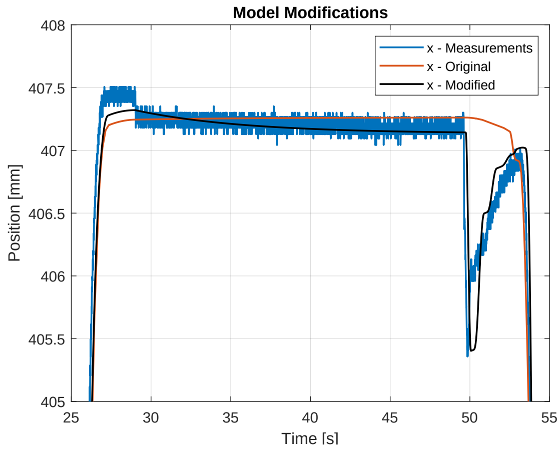

Figure 11.3: Cylinder position - Zoom.

The model modifications have also improved the accuracy of the simulated pressure p_A. This can be seen in figure 11.4 and 11.5.

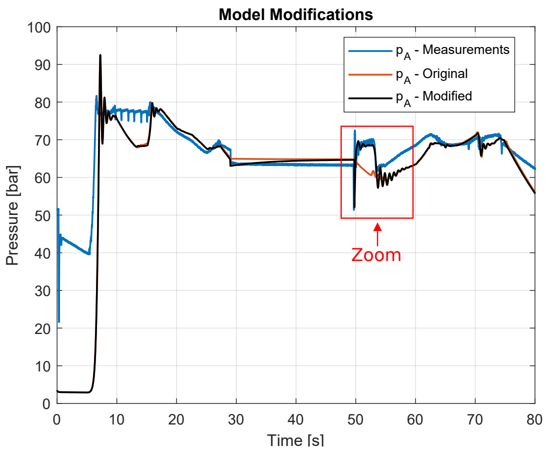

Figure 11.4: Cylinder pressure A.

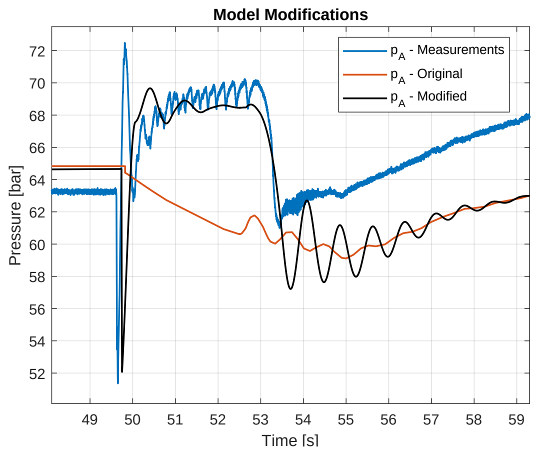

Figure 11.5: Cylinder pressure A - Zoom.

The model modifications only have only a small impact on the pressures p_B and p_{acc}, and therefore thise pressures are not shown.

Based on the simulation results it is concluded that the modified Simulink model is more accurate compared to the original Simulink model.
It is desired to reduce the position drop when the POCV's are opened, and therefore additional control schemes are developed. The modified Simulink model is used to develop switching logic and to test the new control schemes.

11.3 New Control Schemes - Feed Forward

The section starts with an explanation of the switching logic behind the feed forward because it shows the idea behind the feed forward. After this, flow feed forward (FFF) is presented and then pressure feed forward (PFF) is explained.

11.3.1 Switching Logic

The switching logic resembles the switching logic seen in figure 9.1. However, it can be seen in figure 11.6 that an additional time interval has been added (T_4). Table 11.1 provides an overview of the different trajectory and controller choices.
The value $p_{A,con}$ is a stored value when the POCV's switches from open to closed. This value is used as reference for the FFF and PFF. The pressure p_A cannot be used as the reference because p_A drops when the POCV's are opened.

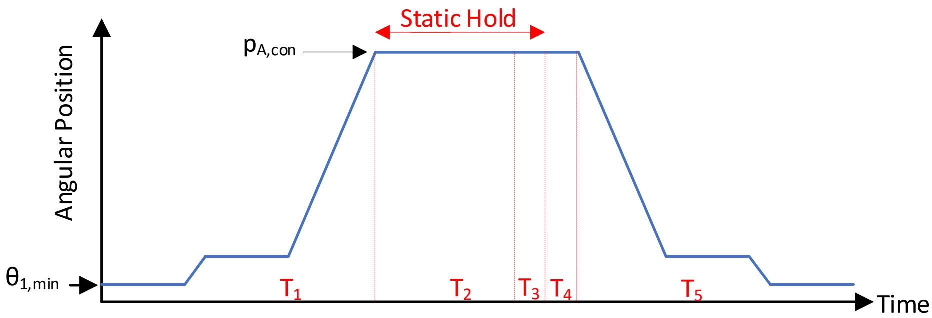

Figure 11.6: Schematic used to show the different time intervals.

Intervals	Controller Choice	Trajectory Reference	VFF	HPPF	POCV
Interval 1	Position	Position	On	On	Open
Interval 2	Internal Model Control	0 rad/s	Off	Off	Closed
Interval 3	Pressure	p_A	Off	Off	Closed
Interval 4	Position + FFF/PFF	Position and $p_{A,con}$	Off	On	Open
Interval 5	Position	Position	On	On	Open

Table 11.1: Overview of the different trajectory and controller choices.

The switching logic for the feed forward is also based on states, and it is an additional input for the motor reference.

11.3.2 Flow Feed Forward

They idea behind the flow feed forward control is to compensate for the flow Q_{in} seen in equation I.3 when the POCV's are opened. Therefore the FFF should equal Q_{in} when the POCV's are opened. This is seen in equation 11.1.

$$FFF = x_v \cdot K_{3/2} \cdot \sqrt{|p_{A,con} - p_{3/2}|} \tag{11.1}$$

The FFF has been implemented in the Simulink model, and it can be seen that when the FFF is activated then the reference for the motor exceeds the limitations of the motor. Furthermore, it can be seen that the actual motor speed can not keep of with the reference. For these reasons it is chosen to scale down the FFF before it is implemented in the experimental setup.

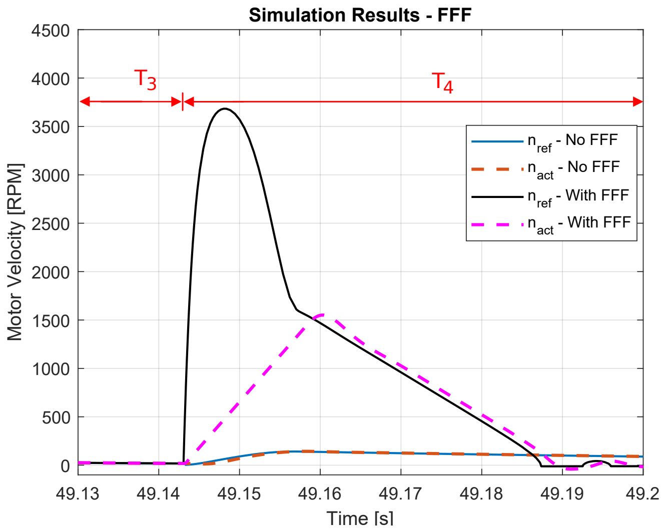

Figure 11.7: Simulation results showing the influence of FFF.

11.3.3 Pressure Feed Forward

The idea behind PFF is to use a pressure feedback controller in order to compensate for the pressure drop when the POCV's are opened. The design of the pressure feedback controller resembles the design of the pressure controllers in chapter 8, and thus the designed procedure is not included in this subsection. Instead it is found in appendix J. The equation for the PFF is seen in equation 11.2.

$$PFF = K_{p,PFF} \cdot \sqrt{|p_{A,con} - p_A|} \tag{11.2}$$

11.4 FFF and PFF Testing

In order to test the FFF and PFF then 3 different tests are conducted, and they are listed in table 11.2.

Test Number	Trajectory	HPPF, VFF and Pressure Controller	FFF	PFF
1	1000 RPM	On	On	Off
2	1000 RPM	On	Off	On
3	1000 RPM	On	Off	Off

Table 11.2: Overview of the 3 controller tests.

11.4.1 Comparison between Simulation and Experiment

As it is shown in figure 11.7 then the motor is not capable of following the reference. This problem is now investigated.

Test 1

As it can be seen in figure 11.8 then the cylinder position still drops even though the FFF is implemented. The position drop is approximately 0.6 mm.
The reason for the position drop can be seen in figure 11.9. It can be seen that the motor cannot keep up with the reference in the experiments. However, in the simulation the acceleration of the motor is faster compared to the measurements. This indicates that the saturation limit for the acceleration of the motor in the simulation is too high (see figure 4.2).
A reason for this could be that the saturation limit is based on [11], and is found for a no-load-condition as discussed in section 4.1.

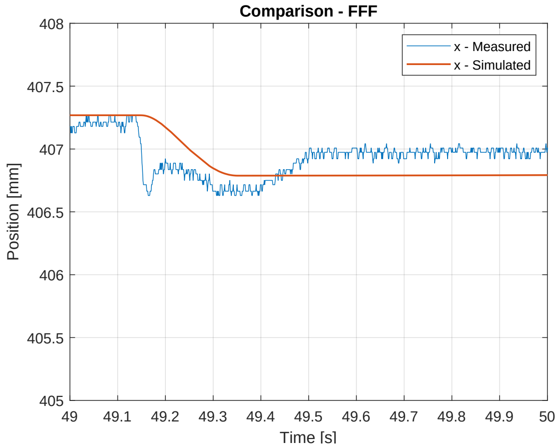

Figure 11.8: Cylinder position - Zoom.

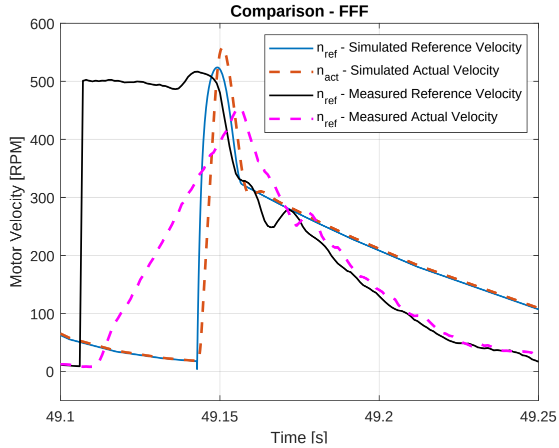

Figure 11.9: Motor Velocity - Zoom.

Test 2

As it can be seen in figure 11.10 then the cylinder position still drops even though the PFF is implemented. The position drop is approximately 0.7 mm.
Based on figure 11.11 it is concluded the motor cannot keep up with the given trajectory. Furthermore, as for the FFF then it is concluded that the saturation limit for the motor acceleration in the Simulink model is too high.

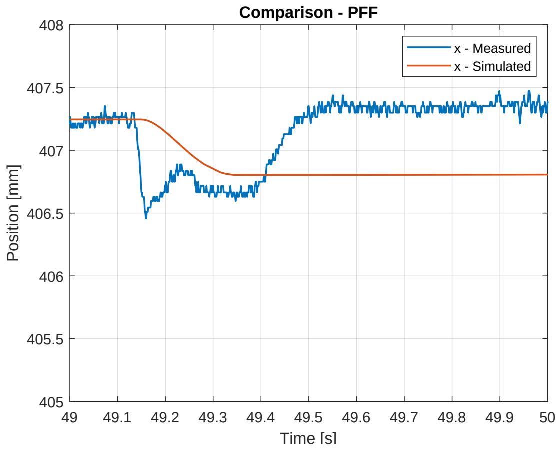

Figure 11.10: Cylinder position - Zoom.

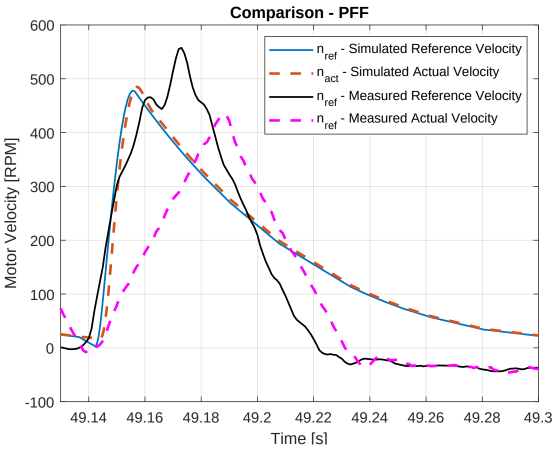

Figure 11.11: Motor Velocity - Zoom.

11.4.2 Experimental Comparison - Test 1,2 and 3

In order to see the influence of the FFF and the PFF then they plotted together with the test 3 (without FFF or PFF). The results can be seen in figure 11.12. In figure 11.13 it can be seen that even though the motor cannot keep up with the given reference then both the FFF and the PFF reduce the position drop when the POCV's are opened.

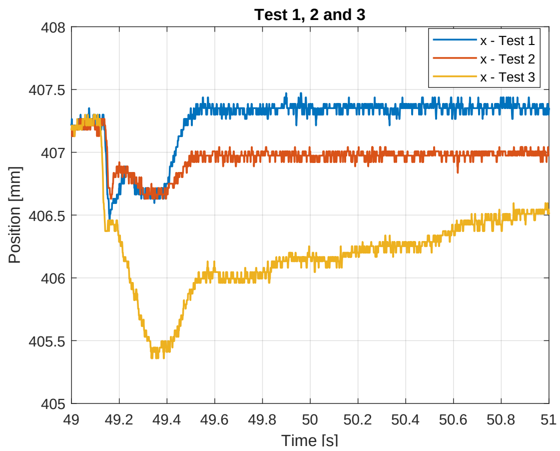

Figure 11.12: Experimental data - FFF and PFF.

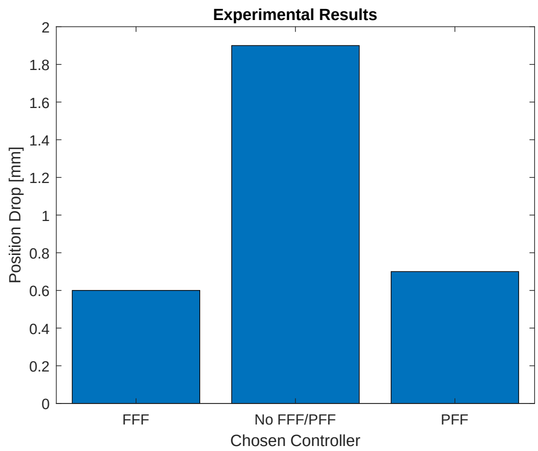

Figure 11.13: Comparison - Test 1, 2 and 3.

11.5 Preliminary Conclusions

Based on the simulation results in this chapter then the modified Simulink model describes the opening of the POCV's more accurately compared to the original Simulink model. However, through experiments it has been shown that the saturation limit for the motor acceleration should be adjusted such that that the Simulink describes reality even more precisely. If the saturation limit is adjusted then gains for the FFF and PFF can be adjusted and this could potentially lead to a lower position drop when the POCV's are opened.

Furthermore, more work should be put into developing the feed forward design. It has been shown that the motor is delayed in the response, and this could be potentially be implemented in the control logic such that the motor would speed up before the POCV's are opened.

It is concluded that both the FFF and the PFF both work, and that they reduce the position drop when the POCV's are opened. With FFF and PFF, the position drop is kept below the 1mm as stated in the problem statement.

12 | Conclusion

The goal of this project is stated in chapter 3, and the goal is to develop different control strategies for the crane such that a given trajectory is followed accurately.

In order to achieve this goal, a Simulink model of the experimental setup has been developed and validated through experimental tests. After this, the model is linearised in order to apply linear control theory, and it is concluded that the linear model describes the dynamics of the nonlinear model accurately. Based on the linearisation of the model it is concluded that the system is underdamped, and a resonance peak placed is present at approximately [12 rad/s].
During the position controller design the resonance peak is taken taken into account, and therefore high-pass filtered pressure feedback is developed such that a higher damping ratio of the system is achieved. Different, linear controllers are developed for position control, and they are implemented along with velocity feed forward.
Based on the problem statement it is also desired to reduce the position drop after the re-opening of the POCV's, and therefore pressure controllers are designed such that pressure can be build up before the opening of the POCV's.
The developed position and pressure controllers are implemented on the experimental setup, and the position errors for the 2800 RPM trajectory can be seen in figure 12.1 and 12.2. Based on figure 12.1 and 12.2 it is concluded that the errors are kept within the limitations of the hard demands from the problem statement. The average error is kept below 1mm, and the maximum deviation from the trajectory is kept below 10mm.

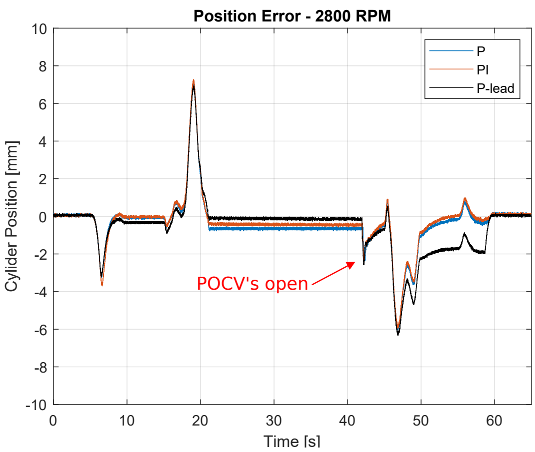

Figure 12.1: Position error graph - Experiments.

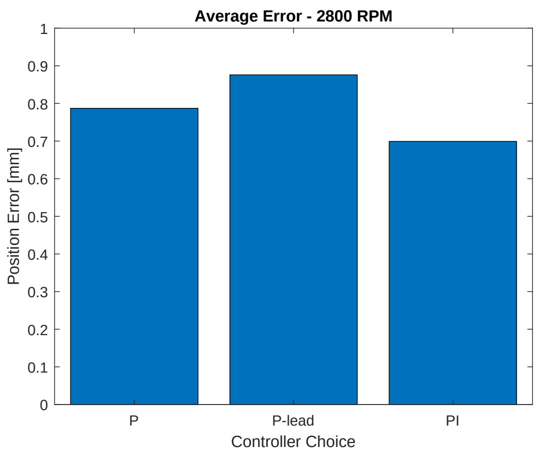

Figure 12.2: Average error - Experiments.

However, based on the problem statement, the position drop must not be above 1mm when the POCV's are opened. It can be seen in figure 12.1 that this demand is not kept below the limitation (The position drop was not foreseen because it was not present in the simulation results).
Therefore a hypothesis is developed, and the idea is that the pressure $p_{3/2}$ and the 3/2-valve should be included in the Simulink model. Therefore the Simulink model has been

modified in chapter 11, and hereby the accuracy of the Simulink model has been improved when the POCV's are opened.

In order to keep the position drop below 1mm then 2 new control strategies are developed (FFF and PFF). The modified Simulink model is used to test these controllers and the switching logic. The FFF and PFF have been implemented and tested at the experimental setup. The results can be seen in figure 12.3 and 12.4. It can be seen that both control strategies keep the position drop below 1mm, and therefore the demand from the problem statement is kept within the limit.

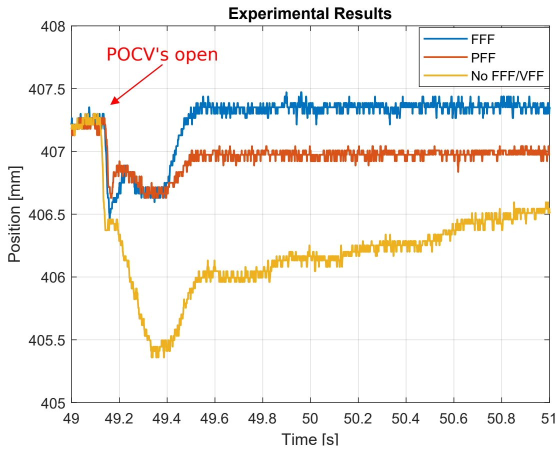

Figure 12.3: Position error graph - Experiments.

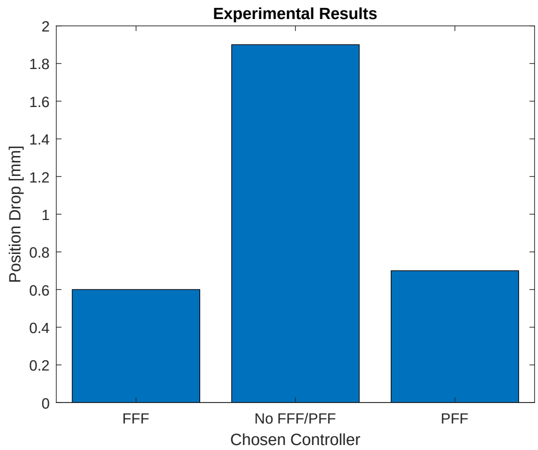

Figure 12.4: Position drop - Experiments.

It is concluded that the position drop seen in figure 12.3 is due to a delay and the acceleration limit of the motor. Further work could be put into reducing this position drop even more and this is discussed in chapter 13.

All in all it is concluded that the developed control schemes work satisfactory because all demands from the problem statement are kept within the boundaries. Therefore it is concluded that the project is a success.

13 | Future Work

Model Adjustments

In section 11.5 it is concluded that the implemented FFF and PFF both reduce the position drop when the POCV's are opened. However, it is also concluded that the motor model should be adjusted in the Simulink model.
Firstly, the delay seen in figure 13.1 and 13.2 should be implemented in the Simulink model. Furthermore, it is also included in section 11.5 that the saturation limit for the motor acceleration should be decreased. This would improve the accuracy of the Simulink model.
These 2 adjustments in the Simulink model could be used to test the developed FFF and PFF such that the position drop could be decreased even further.

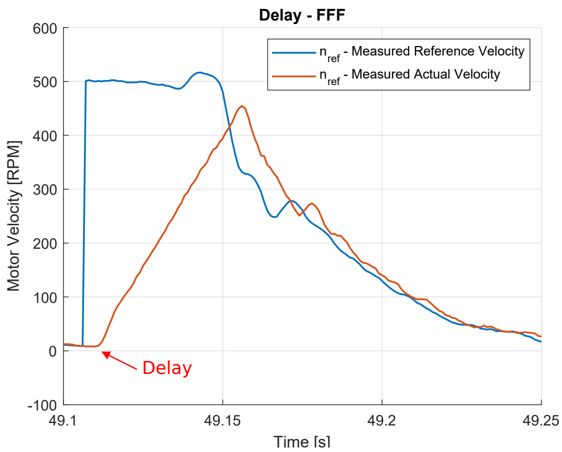

Figure 13.1: Experimental data - FFF test.

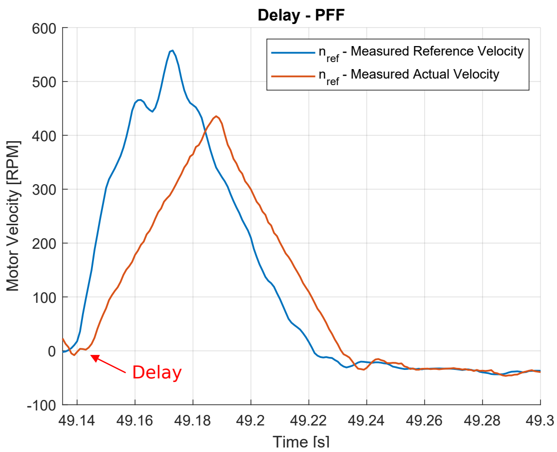

Figure 13.2: Experimental data - PFF test.

New Control Strategies

The adjusted Simulink model could be used to investigate the influence of a delayed opening of the POCV's. If the opening is delayed with the same amount as the motor delay seen in figure 13.1 and 13.2 then the motor most likely would be able to follow the trajectory more precisely. Furthermore, it could also be tested if it would be an advantage to give the motor a "head start" before the opening of the POCV's. If the motor speed is increased before the opening of the POCV's then this might decrease the position drop. However, care should be taken because if the motor velocity is increased before the opening of the POCV's then the pressure p_{PA} is increased. This could potentially lead to an undesired and unintended opening of the POCV's because the crack pressure of the POCV's could be exceeded.

Improving Present Control Strategies

Throughout the development of pressure controllers it has been shown that gain schedule could potentially be a good solution. The reason for this is that the gain schedule controller could decrease the time used to build up the pressure p_{PA} before the opening of the POCV's. This would lead to a more smooth operation of the crane because the pressure-build-up-time would be reduced. Therefore more work should be put into the implementation of these controllers.

Furthermore, in section 10.2.3, the 2800RPM trajectory is tested. In the experimental results it is shown that an position error of approximately 7.5mm is present after 20 seconds. It could be interesting to adjust the designed controller such that the position error is reduced. Based on the discussion in section 5.4 it is concluded that the designed controller potentially could be design more aggressively. This would most likely reduce the position error and more work could be put into this topic.

Bibliography

[1] Torben Ole Andersen. *Fluid Power Systems*. 2003. Aalborg University.

[2] Torben Ole Andersen and Michael Rygaard Hansen. Fluid power circuits - system design and analysis. 2007. Institute of Energy Technology and Institute of Mechanical Engineering - Aalborg University.

[3] Bosch Rexroth Group. Datasheet: Variable-speed drive with fixed displacement unit a10fzo/g. .

[4] Bosch Rexroth Group. Datasheet: Bladder-type accumulator - type hab. .

[5] Bosch Rexroth Group. Datasheet: Inline filter with filter element according to din 24550, type: 50len0040 to 0400; 50le0130, 0150. .

[6] Hawe Hydraulics. Datasheet: Check valve type rk and rb. 2017.

[7] Argo Hytos. Datasheet: 3/2 directional valve, solenoid operated, poppet type, blocking: Model sd1e-a3. 2016.

[8] Michael Rygaard Hansen Jesper Kirk SÃ¸rensen and Morten Kjeld Ebbesen. Numerical and experimental study of a novel concept for hydraulically controlled negative loads. 2016. Department of Engineering Sciences, Facultu of Engineering and Science, University of Agder.

[9] Seth Hutchinson Mark W. Spong and M. Vidyasagar. Robot dynamics and control. 2004. Second Edition.

[10] Dipl.-Ing. Sebastian Michel and Professor Dr.-Ing. Jürgen Weber. Electrohydraulic compact-drives for low power applications considering energy-efficiency and high inertial loads.

[11] Morten Grønkjær and Henrik Rahn. Master thesis: Control and experimental evaluation of speed-variable switched differential pump concept.

[12] Charles L. Phillips and John M. Parr. Feedback control systems. 2011. Fifth Edition.

[13] Rexroth. Datasheet: Rexroth indradyn s msk synchronous motors. 2018. Fith Edition.

[14] SunHydraulics. Datasheet: Pilot-to-open check valve with standard pilot: Model ckeb. 2018.

[15] SunHydraulics. Datasheet: Vented pilot-to-open check valve: Model cvev. 2018.

[16] Jinman Zhang Zhongyi Quan, Long Quan. Review of energy efficient direct pump controlled cylinder electro-hydraulic tecnology. 2014. Taiyuan University of Technology.

Appendices

A | Constants

Geometrical Constants

Abbreviation	Description	Value	Unit
$\lvert AB \rvert$	Length from point A to point B	1.136	m
$\lvert AB_x \rvert$	X component of |AB|	0.420	m
$\lvert AB_y \rvert$	Y component of |AB|	1.055	m
$\lvert AC \rvert$	Length from point A to point C	0.565	m
$\lvert AC_x \rvert$	X component of |AC|	0.550	m
$\lvert AC_y \rvert$	Y component of |AC|	0.130	m
$\lvert BC_{min} \rvert$	Minimum length from point B to point C	0.772	m
l_1	Beam length	3.680	m
l_2	Beam length	0.080	m
l_3	Beam length	0.215	m
l_4	Beam length	0.100	m
l_5	Beam length	0.150	m
l_6	Beam length	0.006	m
l_7	Stack length	0.700	m
l_8	Stack length	0.300	m
l_9	Stack length	0.100	m
l_{10}	Stack length	0.150	m
l_{cm1}	Length from attachment of joint 1 to COM of beam 1	1.66	m
l_{cm2}	Length from attachment of joint 2 to COM of beam 2	0.135	m
α_1	Constant geometrical angle	0.2321	rad
α_2	Constant geometrical angle	1.1919	rad
$\theta_{1,min}$	Minimum angle for θ_1	-0.400	rad
$\theta_{1,max}$	Maximum angle for θ_1	0.5208	rad

Hydraulic Constants

Abbreviation	Description	Value	Unit
A_p	Area of piston area	0.0033	m^2
A_r	Area of rod side area	0.0024	m^2
$B_{\omega,N}$	Viscous torque coefficient for $\dot{\theta}_1 < 0$ rad/s	2300	$Nm \cdot s$
$B_{\omega,P}$	Viscous torque coefficient for $\dot{\theta}_2 > 0$ rad/s	2300	$Nm \cdot s$
c_{ad}	Adiabatic constant of air	1.4	$-$
$K_{L,ext}$	External leakage coefficient for the pump	$3.96 \cdot 10^{-14}$	m^3/rad
$K_{L,int}$	Internal leakage coefficient for the pump	$2.03 \cdot 10^{-13}$	m^3/rad
K_V	Displacement coefficient	$1.6 \cdot 10^{-6}$	m^3/rad
L_c	Cylinder stroke length	0.5	m
p_0	Accumulator precharge pressure	$0.051 \cdot 10^5$	Pa
V_{01}	Control volume	$3.31 \cdot 10^{-5}$	m^3
V_{02}	Control volume	$3.31 \cdot 10^{-5}$	m^3

V_{acc}	Accumulator volume	0.0092	m^3
$V_{0,acc}$	Control volume for accumulator	$5 \cdot 10^{-5}$	m^3
β_{oil}	Stiffness of pure oil	$16000 \cdot 10^5$	Pa
ε_{air}	Volumetric constant of air in fluid	0.9	%
$\omega_{n,m}$	Eigenfrequency for motor	754	rad/s
$\zeta_{n,m}$	Damping for motor	0.5	$-$
$\tau_{cou,N}$	Coulomb torque for $\dot{\theta}_1 < 0$ rad/s	650	Nm
$\tau_{cou,P}$	Coulomb torque for $\dot{\theta}_1 > 0$ rad/s	700	Nm

Mechanical Constants

Abbreviation	**Description**	**Value**	**Unit**
A_1	Cross section sub-area of ballast stack	0.090	m^2
A_2	Cross section sub-area of ballast stack	0.105	m^2
I_1	Moment of Inertia beam 1	289	$kg \cdot m^2$
I_2	Moment of Inertia beam 1	3962	$kg \cdot m^2$
k_s	Spring constant	$3 \cdot 10^7$	N/m
M_1	Submass of beam	1.557	kg
M_2	Submass of beam	75.7	kg
M_3	Submass of beam	4.82	kg
M_4	Mass of ballast stack	320	kg
ρ_{steel}	Density of steel	7850	kg/m^3

Linearisation Constants

Abbreviation	**Description**	**Value**	**Unit**
d_{11}	Entrance in $\underline{\underline{D_0}}$	8526	kg·m^2
d_{12}	Entrance in $\underline{\underline{D_0}}$	4116	kg·m^2
d_{21}	Entrance in $\underline{\underline{D_0}}$	4116	kg·m^2
d_{22}	Entrance in $\underline{\underline{D_0}}$	3968	kg·m^2
d_a	Entrance in $\underline{\underline{D_0}}^{-1}$	$2.349 \cdot 10^{-4}$	1/(kg·m^2)
d_b	Entrance in $\underline{\underline{D_0}}^{-1}$	$-2.437 \cdot 10^{-4}$	1/(kg·m^2)
d_c	Entrance in $\underline{\underline{D_0}}^{-1}$	$-2.437 \cdot 10^{-4}$	1/(kg·m^2)
d_d	Entrance in $\underline{\underline{D_0}}^{-1}$	$5.048 \cdot 10^{-5}$	1/(kg·m^2)
$K_{\phi 1}$	Linearisation constant	3689	-
$K_{\phi 2}$	Linearisation constant	126.8	-
$K_{\phi 3}$	Linearisation constant	$3 \cdot 10^7$	-
$K_{\tau 1}$	Linearisation constant	7988	Nm / rad
$K_{\tau 2}$	Linearisation constant	0.0017	Nm / Pa
K_{LA1}	Linearisation constant	0.0039	m/(s·rad)
K_{LA2}	Linearisation constant	0.3567	m/rad

Universal Constants

Abbreviation	**Description**	**Value**	**Unit**
g	Gravitational acceleration	9.2	m/s^2
γ	Gas constant for N_2	1.4	-

B | Mechanical Analysis

B.1 Mass of Crane

In order to calculate the masses M_1, M_2, M_3 and M_4 (see figure B.1) then the following two assumptions are made:

- The beam consists of steel with a density of $\rho_{steel} = 7850\frac{kg}{m^3}$
- The ballast stack is assumed to be one solid block

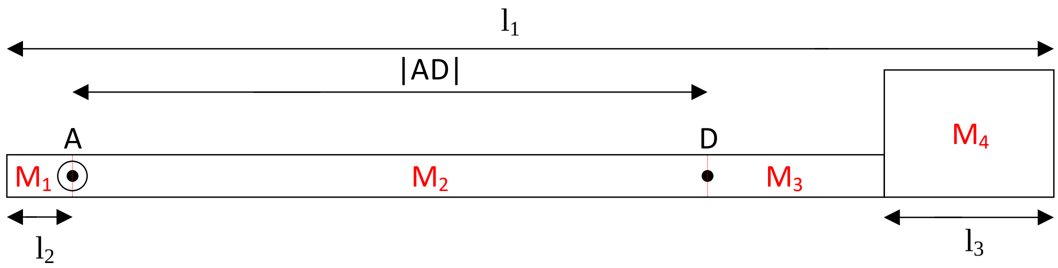

Figure B.1: Sketch of beam and ballast stack.

M_1, M_2 and M_3 is calculated based on figure B.2 and is given by equation B.1, B.2 and B.3.

$$M_1 = \rho_{steel} \cdot l_4 \cdot l_5 \cdot l_2 - \rho_{steel} \cdot (l_4 - 2 \cdot l_6) \cdot (l_5 - 2 \cdot l_6) \cdot l_2 - \rho_{steel} \cdot r^2 \cdot \pi \cdot l_6 \tag{B.1}$$

$$M_2 = \rho_{steel} \cdot l_4 \cdot l_5 \cdot |AD| - \rho_{steel} \cdot (l_4 - 2 \cdot l_6) \cdot (l_5 - 2 \cdot l_6) \cdot (|AD|) - \rho_{steel} \cdot r^2 \cdot \pi \cdot l_6 \tag{B.2}$$

$$M_3 = \rho_{steel} \cdot l_4 \cdot l_5 \cdot (l_1 - l_2 - |AD|) - \rho_{steel} \cdot (l_4 - 2 \cdot l_6) \cdot (l_5 - 2 \cdot l_6) \cdot (l_1 - l_2 - |AD|) \tag{B.3}$$

Hereby the total mass of the beam is calculated by equation

$$M_{beam} = M_1 + M_2 + M_3 = 82kg \tag{B.4}$$

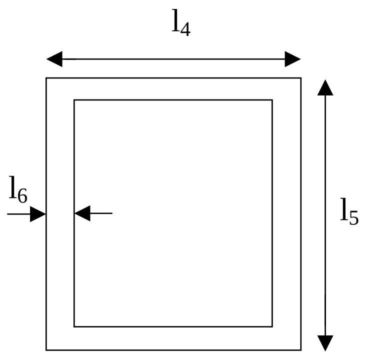

Figure B.2: Sketch used to calculate the positions of the center of masses.

The stack consists of four ballast plates and an end plate. Each of the ballast plates weighs 76 kg and the end plate weighs 16 kg. Hereby M_4 is calculated is equation B.5.

$$M_4 = 4 \cdot 76kg + 16kg = 320kg \tag{B.5}$$

B.2 Center off Mass

In the mathematical model it is decided split the beam into 2 beams. The two beams are connected with an artificial spring. This decision is based on observations from the experimental setup. The beam is vibrating during movement, and these vibrations cause oscilations in the pressures. In order to imitate these vibrations then the artificial spring is included. The position of the spring can be seen in figure B.3.

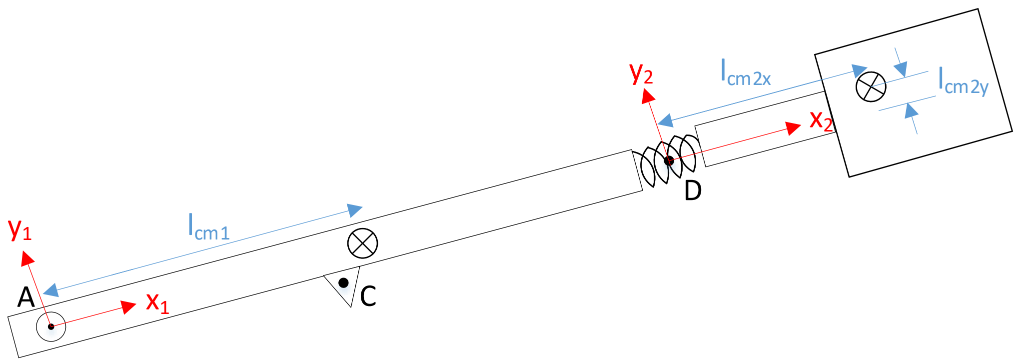

Figure B.3: Cross section of the beam

The lengths l_{cm1}, l_{cm2x} and l_{cm2y} are used in appendix E, and the lengths are calculated in the following equations.
l_{cm1} is calculated with respect to the x_1-y_1-coordinate system.

$$l_{cm1} = \frac{M_1 \cdot \frac{-l_2}{2} + M_2 \cdot \frac{|AD|}{2}}{M_1 + M_2} = 1.66m \tag{B.6}$$

The center of mass for the ballast stack is based on figure B.4.

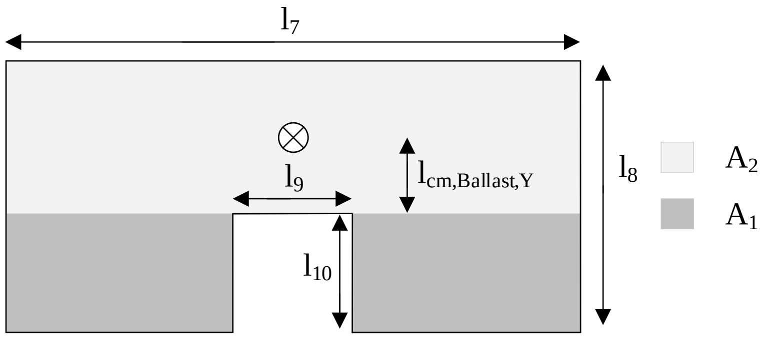

Figure B.4: Cross section of the ballast stack

$$l_{cm,Ballast,Y} = \frac{\frac{l_{10}}{2} \cdot A_1 + (l_{10} + \frac{l_8 - l_{10}}{2}) \cdot A_2}{A_1 + A_2} = 0.08m \tag{B.7}$$

l_{cm2x} and l_{cm2y} are calculated with respect to the x_2-y_2-coordinate system.

$$l_{cm2x} = \frac{M_3 \cdot \frac{l_1 - l_2 - |AD|}{2} + M_4 \cdot (l_1 - l_2 - |AD| - \frac{l_3}{2})}{M_3 + M_4} = 0.11m \tag{B.8}$$

$$l_{cm2y} = \frac{M_3 \cdot 0 + M_4 \cdot (l_{cm,Ballast,Y} + \frac{l_{10}}{2})}{M_3 + M_4} = 0.08m \tag{B.9}$$

Hereby l_{cm2} is calculated to be:

$$l_{cm2} = \sqrt{l_{cm2x}^2 + l_{cm2y}^2} = 0.13m \tag{B.10}$$

From equation B.8 and B.10 then is can be seen that $l_{cm2} \approx l_{cm2x}$. This approximation is chosen as it simplifies the calculation in the Euler Lagrange (No constant angle has to be added).

B.3 Mass Moment of Inertia

The calculations of I_1 and I_2 are essential for the Euler-Lagrange equations in appendix E. I_1 describes the mass moment of inertia of the first part of the beam, and I_2 describes the mass moment of inertia of the second part of the beam (see in figure B.5). The beam rotates around point A.

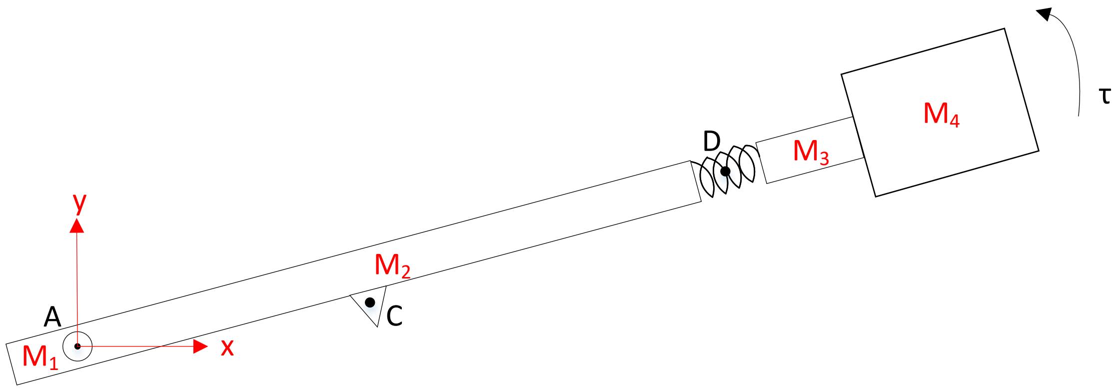

Figure B.5: Sketch of the beam used to calculate I_1 and I_2.

$$I_1 = \frac{1}{3} \cdot l_2^2 \cdot M_1 + \frac{1}{3} \cdot |AD|^2 \cdot M_2 = 289kg \cdot m^2 \tag{B.11}$$

$$I_2 = \frac{1}{3} \cdot (l_1 - l_2)^2 \cdot (M_2 + M_3) - \frac{1}{3} \cdot |AD|^2 \cdot M_2 + (l_1 - l_2 - \frac{l_3}{2})^2 \cdot M_4 = 3962kg \cdot m^2 \tag{B.12}$$

C | Signal Overview

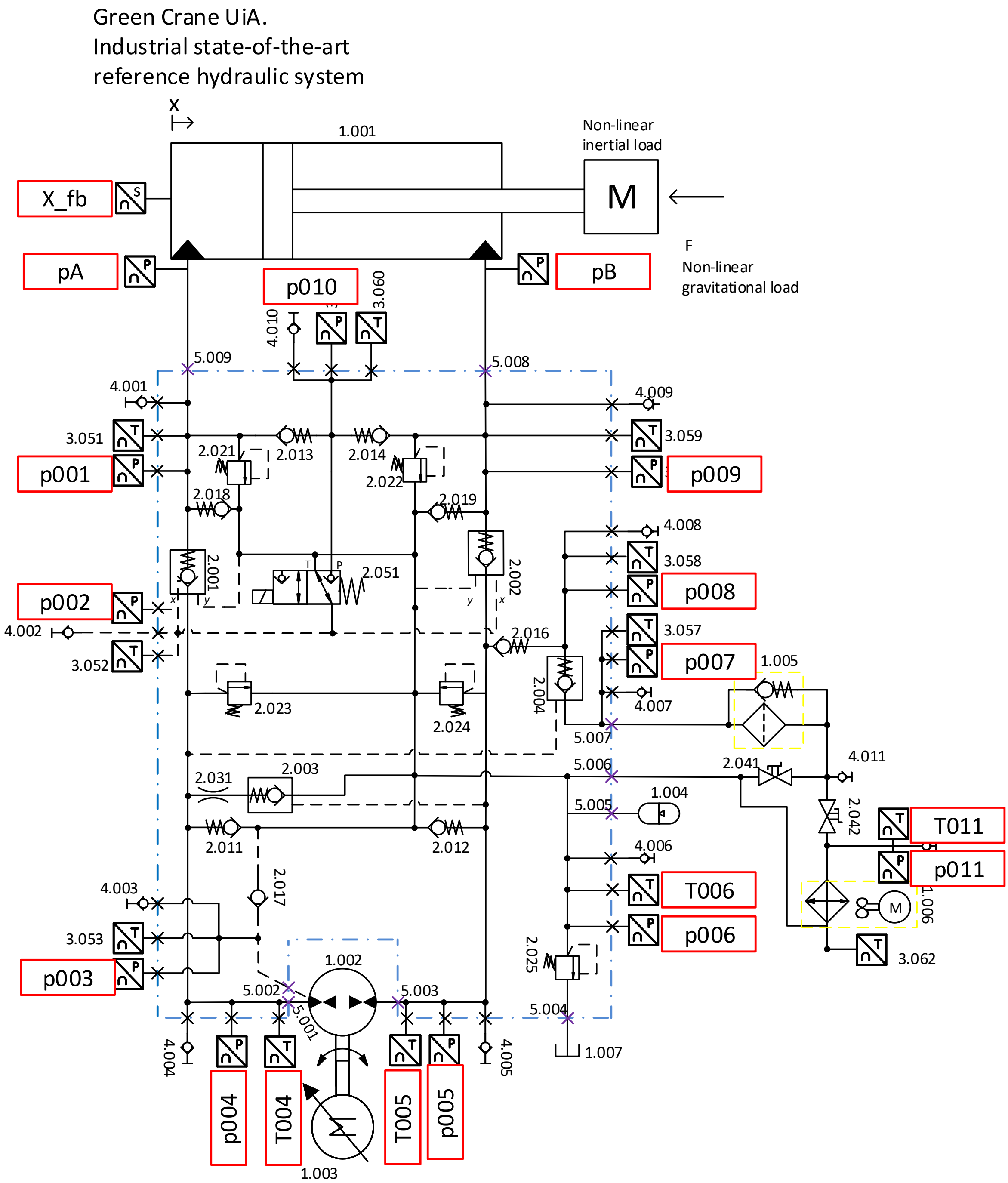

Figure C.1: Sketch showing the hydraulic setup.

D | POCV's and Orifice Model

Pilot Operated Check Valves

The pilot operated check valves (POCV) with number 10 are modelled with the same procedure as for the check valves (section 4.2.2).

Pilot Operated Check Valve Number 10

The flow through the pilot operated check valves is described be equation D.1.

$$Q_{cv} = \frac{Q_{cv,n}}{\Delta p_{cv,n}} \cdot x_{cv,n} \cdot \sqrt{\Delta p_{cv}} \cdot sign(\Delta p_{cv}) \tag{D.1}$$

The difference between the pilot operated check valves and the check valves is that the opening of the pilot operated check valves may be aided by a pilot pressure. Therefore the expression for $x_{cv,n}$ is changed, and $x_{cv,n}$ is given by equation D.2.

$$x_{cv,n} = \begin{cases} 0 & \Delta p_{ABCD} < p_{cv,cp} \\ \frac{\Delta p_{ABCD} - p_{cv,cp}}{p_{cv,cpe} - p_{cv,cp}} & p_{cv,cp} < \Delta p_{ABCD} < p_{cv,cpe} \\ 1 & \Delta p_{ABCD} > p_{cv,cpe} \end{cases} \tag{D.2}$$

Where p_{ABCD} is given by equation D.3, and the pressures are defined in figure D.1.

$$p_{ABCD} = \begin{cases} p_A - p_B & p_C < p_D \\ p_A - p_B + (p_C - p_D) \cdot R_{cv} & p_C > p_D \end{cases} \tag{D.3}$$

R_{cv}	Area ratio between spool and poppet [-]

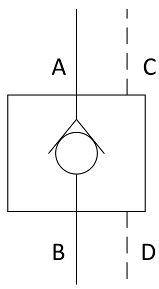

Figure D.1: *Schematic of a pilot operated check valve.*

A comparison between the datasheet and the approximation is seen in figure D.2. It can be seen that 2 different approximations are present in the figure. The blue graph represents

the flow if the valve is fully open (the pilot pressure opens the valve fully). The red graph represents the flow if the pilot pressure does not aid the opening of the valve. The flow through the POCV is modelled as the red approximation. However, in the model the pilot pressure is also included.
During normal operation of the system the POCV is fully opened due to the pilot pressure (high pressure side is connected to port C - See figure D.1 and 2.3). During the static hold of the load port C is connected to the accumulator pressure, and in this case the POCV is fully closed. This means that due to the operation principle of the POCV then the POCV is either fully open or closed.

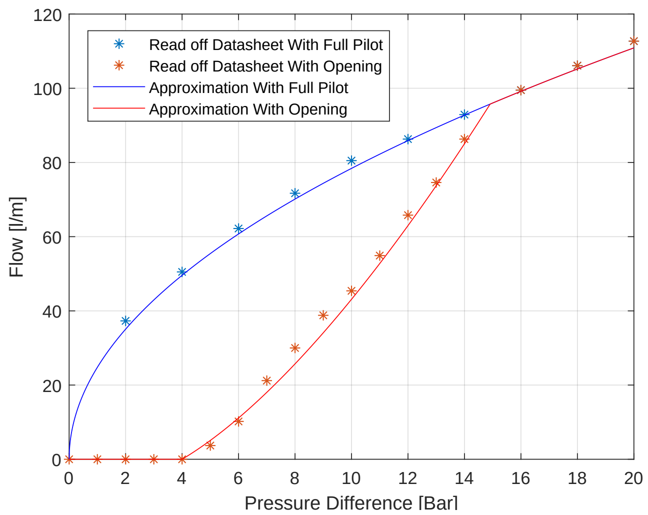

Figure D.2: *Comparison between data point and approximation.*

Orifice Model

The orifice simplification seen in figure 2.4 is modelled as seen in figure D.3. In the following the models of the POCV with number 4 and the oil filter are described.

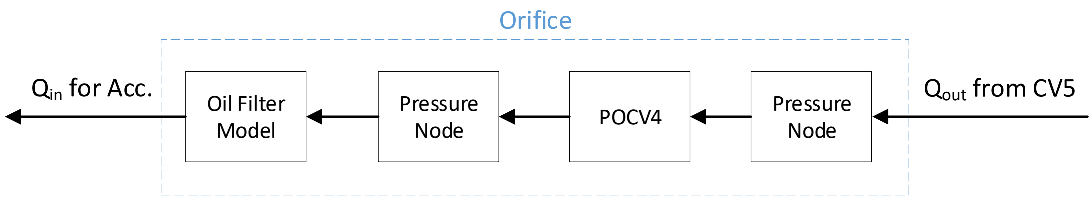

Figure D.3: *Flow diagram showing how the orifice is modelled.*

Pilot Operated Check Valve Number 4

As it can be seen in figure 2.3 then during the operation of the system then the POCV number 4 is always fully open. Therefore the modelling of the POCV is simplified and the flow through the POCV is modelled as seen in equation D.4.

$$Q_{cv} = \frac{Q_{cv,n}}{\Delta p_{cv,n}} \cdot \sqrt{\Delta p_{cv}} \tag{D.4}$$

The approximation can be seen in figure D.4.

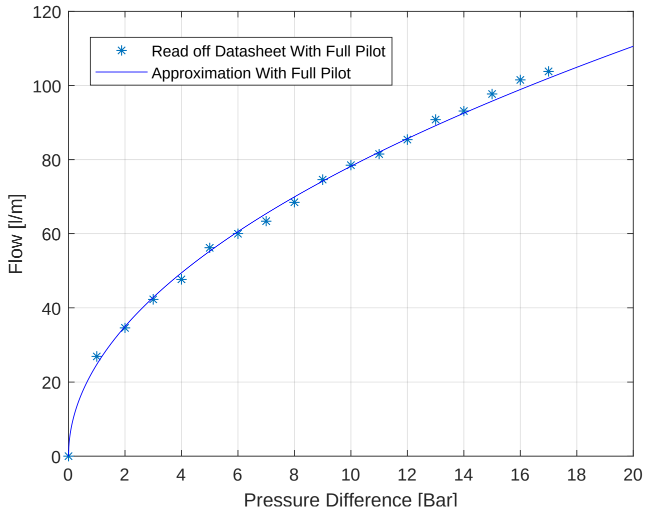

Figure D.4: *Comparison between data point and approximation.*

Oil Filter Model

The oil filter is modelled based on information in the datasheet. It is known that the viscosity of the oil is approximately 46 mm^2/s. However, information regarding the flow is only available for a viscosity at 30 mm^2/s and 68 mm^2/s. Therefore an approximation has been calculated for a viscosity at 46 mm^2/s based on datasheet information [5].
The implemented approximation can be seen in figure D.5, and the approximation consists of 3 piecewise linear functions.

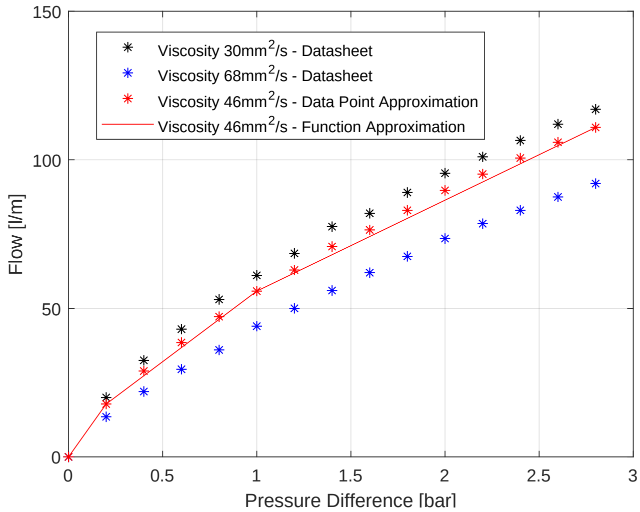

Figure D.5: *Approximation that describes the flow through the oil filter.*

E | Euler Lagrange

E.1 Geometry

It has been observed that during movement of the crane then the beam vibrates. This causes oscillations in the pressures during the movement of the crane. In order to include the vibrations in the simulation then an artificial spring is included in the model. The spring is placed at point D as seen in figure E.1.

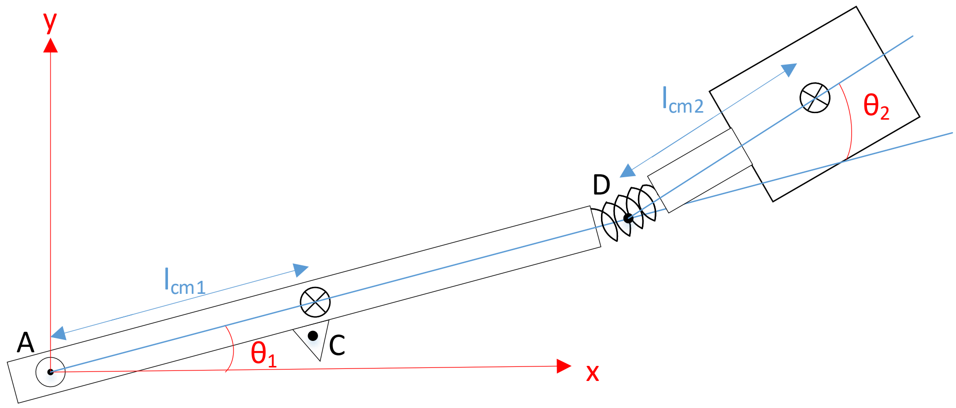

Figure E.1: Sketch used to illustrate the spring at point D. The angel θ_2 is exaggerated

Hereby the beam is divided into 2 sections, and thus 2 different center of masses are present in the drawing. The position of the center of masses are given in the following equations.

$$\underline{p_{cm1}} = \begin{bmatrix} x_{cm1} \\ y_{cm1} \\ z_{cm1} \end{bmatrix} = \begin{bmatrix} l_{cm1} \cdot cos(\theta_1) \\ l_{cm1} \cdot sin(\theta_1) \\ 0 \end{bmatrix} \tag{E.1}$$

$$\underline{p_{cm2}} = \begin{bmatrix} x_{cm2} \\ y_{cm2} \\ z_{cm2} \end{bmatrix} = \begin{bmatrix} |AD| \cdot cos(\theta_1) + l_{cm2} \cdot cos(\theta_1 + \theta_2) \\ |AD| \cdot sin(\theta_1) + l_{cm2} \cdot sin(\theta_1 + \theta_2) \\ 0 \end{bmatrix} \tag{E.2}$$

E.2 Jacobian Matrix

The Jacobian matrix is used to describe both the linear velocity and the angular velocity of the system. The expression is used in the Euler-Lagrange section.

Linear Velocity

The linear velocity of the system is described by equation E.3.

$$\underline{v} = \underline{\underline{J_v}} \begin{bmatrix} \dot{\theta}_1 \\ \dot{\theta}_2 \end{bmatrix} \tag{E.3}$$

$\underline{v}$	3x1 linear velocity vector
$\underline{\underline{J_v}}$	3x2 linear velocity matrix

$\underline{\underline{J_v}}$ is calculated by differentiation of equation E.1 and E.2 [9].

$$\underline{\underline{J_{v1}}} = \begin{bmatrix} \frac{\partial \underline{p_{cm1}}}{\partial \theta_1} & \frac{\partial \underline{p_{cm1}}}{\partial \theta_2} \end{bmatrix} = \begin{bmatrix} -l_{cm1} \cdot sin(\theta_1) & 0 \\ l_{cm1} \cdot cos(\theta_1) & 0 \\ 0 & 0 \end{bmatrix} \tag{E.4}$$

$$\underline{\underline{J_{v2}}} = \begin{bmatrix} \frac{\partial \underline{p_{cm2}}}{\partial \theta_1} & \frac{\partial \underline{p_{cm2}}}{\partial \theta_2} \end{bmatrix} = \begin{bmatrix} -|AD| \cdot sin(\theta_1) - l_{cm2} \cdot sin(\theta_1 + \theta_2) & -l_{cm2} \cdot sin(\theta_1 + \theta_2) \\ |AD| \cdot cos(\theta_1) + l_{cm2} \cdot cos(\theta_1 + \theta_2) & l_{cm2} \cdot cos(\theta_1 + \theta_2) \\ 0 & 0 \end{bmatrix} \tag{E.5}$$

Angular Velocity

The angular velocity is described by equation E.6.

$$\underline{\omega} = \underline{\underline{J_\omega}} \begin{bmatrix} \dot{\theta}_1 \\ \dot{\theta}_2 \end{bmatrix} \tag{E.6}$$

$\underline{\omega}$	3x1 angular velocity vector
$\underline{\underline{J_\omega}}$	3x2 angular velocity matrix

Since the hydraulic setup is restricted to rotate around the z-axis then a unit coordinate vector is used to described the angular velocity [9].

$$\underline{\omega_1} = \underline{k} \cdot \dot{\theta}_1 = \begin{bmatrix} 0 \\ 0 \\ \dot{\theta}_1 \end{bmatrix} \tag{E.7}$$

$$\underline{\omega_2} = \underline{k} \cdot (\dot{\theta}_1 + \dot{\theta}_2) = \begin{bmatrix} 0 \\ 0 \\ \dot{\theta}_1 + \dot{\theta}_2 \end{bmatrix} \tag{E.8}$$

E.3 Euler-Lagrange

The dynamics of the crane is described by the Euler-Lagrange equation, and the equation is seen in equation E.9. [9].

$$\frac{d}{dt}\frac{\partial \mathcal{L}}{\partial \dot{\underline{\theta}}} - \frac{\partial \mathcal{L}}{\partial \underline{\theta}} = \underline{\tau} \tag{E.9}$$

With $\underline{\tau}$ seen in equation E.10.

$$\underline{\tau} = \begin{bmatrix} F_{cyl} \cdot |AC| \cdot sin(\theta_\tau) \\ 0 \end{bmatrix} \tag{E.10}$$

For a 2-DOF system then the following is defined:

$$\begin{aligned} \underline{\theta} &= \begin{bmatrix} \theta_1 \\ \theta_2 \end{bmatrix} \\ \dot{\underline{\theta}} &= \begin{bmatrix} \dot{\theta}_1 \\ \dot{\theta}_2 \end{bmatrix} \end{aligned} \tag{E.11}$$

$\mathcal{L}$ is the Lagrangian of the system, and it is the difference between the kinetic energy and the potential energy. This is seen in equation E.12.

$$\mathcal{L} = \mathcal{K} - \mathcal{P} \tag{E.12}$$

The kinetic energy is defined as the sum of translational and rotational energy, and the kinetic energy is given by equation E.13 [9].

$$\mathcal{K}(\theta, \dot{\theta}) = \frac{1}{2} \cdot \dot{\underline{\theta}}^T \left(m_1 \cdot \underline{\underline{J_{v1}}}^T \cdot \underline{\underline{J_{v1}}} + m_2 \cdot \underline{\underline{J_{v2}}}^T \cdot \underline{\underline{J_{v2}}} + \begin{bmatrix} I_1 + I_2 & I_2 \\ I_2 & I_2 \end{bmatrix} \right) \cdot \dot{\underline{\theta}} = \frac{1}{2} \cdot \dot{\underline{\theta}}^T \cdot \underline{\underline{D}} \cdot \dot{\underline{\theta}} \tag{E.13}$$

m_i	Mass of link i, i = 1,2

Where the inertia matrix $\underline{\underline{D}}$ is given by equation E.14 [9].

$$\underline{\underline{D}} = \begin{bmatrix} m_1 l_{cm1}^2 + m_2[|AD|^2 + l_{cm2}^2 + 2|AD|l_{cm2}^2 + 2|AD|l_{cm2} \cdot cos(\theta_2)] + I_1 + I_2 & m_2[l_{cm2}^2 + |AD|l_{cm2} \cdot cos(\theta_2)] + I_2 \\ m_2[l_{cm2}^2 + |AD|l_{cm2} \cdot cos(\theta_2)] + I_2 & m_2 l_{cm2}^2 + I_2 \end{bmatrix} \tag{E.14}$$

The potential energy $\mathcal{P}$ is given by the sum of the potential energy in the two beams and the artificial spring.

$$\begin{aligned} \mathcal{P}(\underline{\theta}) &= \mathcal{P}_1 + \mathcal{P}_2 + \mathcal{P}_{spring} \\ \mathcal{P}(\underline{\theta}) &= m_1 g l_{cm1} \cdot sin(\theta_1) + m_2 g |AD| \cdot sin(\theta_1) + m_2 g l_{cm2} \cdot sin(\theta_1 + \theta_2) + \frac{1}{2} k_s \theta_2^2 \end{aligned} \tag{E.15}$$

Now that the kinetic energy and the potential energy has been defined then equation E.9 can be calculated. The first part of equation E.9 is now calculated.

$$\frac{d}{dt}\frac{\partial \mathcal{L}}{\partial \dot{\underline{\theta}}} = \frac{d}{dt}\left(\frac{\partial}{\partial \dot{\underline{\theta}}} \mathcal{K}(\underline{\theta}, \dot{\underline{\theta}}) - \frac{\partial}{\partial \dot{\underline{\theta}}} \mathcal{P}(\underline{\theta}) \right) \tag{E.16}$$

As it can be seen in equation E.16 then the potential energy does not depend on $\dot{\underline{\theta}}$, and thus equation E.16 reduces to equation E.17.

$$\frac{d}{dt}\frac{\partial \mathcal{L}}{\partial \dot{\underline{\theta}}} = \frac{d}{dt}\left(\frac{\partial}{\partial \dot{\underline{\theta}}}\mathcal{K}(\underline{\theta}, \dot{\underline{\theta}})\right) = \frac{d}{dt}\frac{\partial}{\partial \dot{\underline{\theta}}}\left(\frac{1}{2}\dot{\underline{\theta}}^T \underline{\underline{D}}\dot{\underline{\theta}}\right) = \frac{d}{dt}\underline{\underline{D}}\dot{\underline{\theta}} = \underline{\underline{D}}\ddot{\underline{\theta}} \tag{E.17}$$

Now the second part of equation E.9 is calculated. The second part of the equation is given by equation E.18 [9].

$$\frac{\partial \mathcal{L}}{\partial \underline{\theta}} = \frac{\partial}{\partial \underline{\theta}}\left(\mathcal{K}(\underline{\theta}, \dot{\underline{\theta}}) - \mathcal{P}(\underline{\theta})\right) = \frac{\partial}{\partial \underline{\theta}}\left(\frac{1}{2}\cdot\dot{\underline{\theta}}^T \underline{\underline{D}}\dot{\underline{\theta}}\right) - \frac{\partial}{\partial \underline{\theta}}\mathcal{P} = -\underline{\underline{C}}\dot{\underline{\theta}} - \underline{\phi} \tag{E.18}$$

Where $\underline{\underline{C}}$ and $\underline{\phi}$ is given in equation E.19 and E.20

$$\underline{\underline{C}} = \frac{\partial}{\partial \underline{\theta}}\left(\frac{1}{2}\cdot\dot{\underline{\theta}}^T \underline{\underline{D}}\right) = \begin{bmatrix} -m_2|AD|l_{cm2}\cdot sin(\theta_2)\dot{\theta}_2 & -m_2|AD|l_{cm2}\cdot sin(\theta_2)\cdot(\dot{\theta}_2+\dot{\theta}_1) \\ m_2|AD|l_{cm2}\cdot sin(\theta_2)\dot{\theta}_1 & 0 \end{bmatrix} \tag{E.19}$$

$$\underline{\phi} = \frac{\partial}{\partial \underline{\theta}}\mathcal{P} = \begin{bmatrix} m_1 g l_{cm1}\cdot cos(\theta_1) + m_2 g|AD|\cdot cos(\theta_1) + m_2 g l_{cm2}\cdot cos(\theta_1+\theta_2) \\ m_2 g l_{cm2}\cdot cos(\theta_1+\theta_2) + k_s\theta_2 \end{bmatrix} \tag{E.20}$$

Hereby the dynamics of the system can be described by equation E.21.

$$\underline{\underline{D}}(\underline{\theta})\ddot{\underline{\theta}} + \underline{\underline{C}}(\underline{\theta}, \dot{\underline{\theta}}) + \underline{\phi}(\underline{\theta}) = \underline{\tau} \tag{E.21}$$

Isolating for $\ddot{\theta}$ yields equation E.22, and the block diagram representation can be seen in figure E.2.

$$\ddot{\underline{\theta}} = \underline{\underline{D}}^{-1}(\underline{\theta})[\underline{\tau} - \underline{\underline{C}}(\underline{\theta}, \dot{\underline{\theta}}) - \underline{\phi}(\underline{\theta})] \tag{E.22}$$

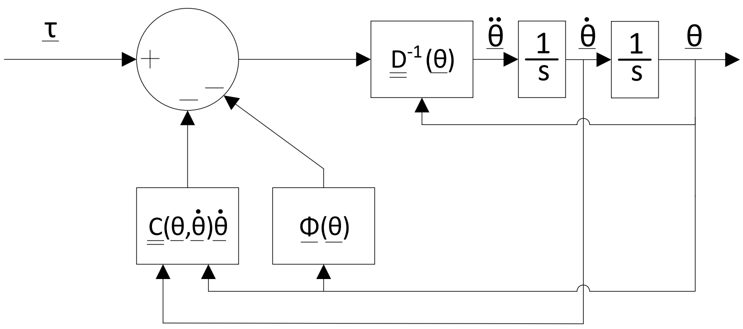

Figure E.2: Block diagram of the implementation of the Euler Lagrange equations.

F | Pump Leakage

In figure F.1 a schematic of a swash plate axial piston pump can be seen.

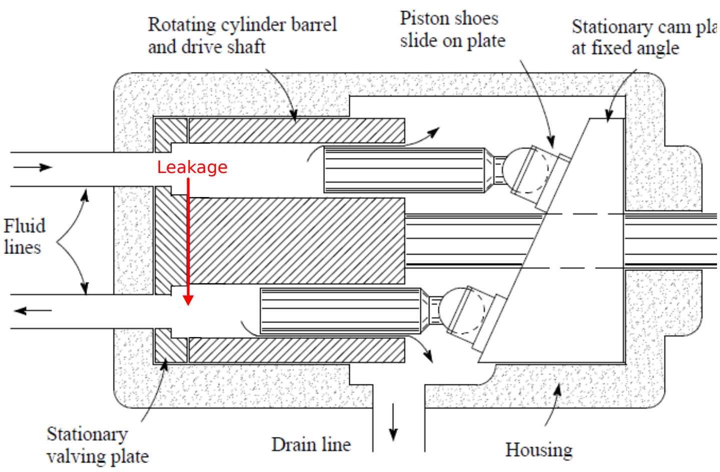

Figure F.1: Modified sketch of a swash plate axial piston pump [2].

Based on figure F.1, two simpler drawings have been made in order to explain why the leakage coefficient varies depending on the pump position. In figure F.2 it can be seen that the narrow passage for the leakage flow is longer compared to figure F.3. A longer passage results in a lower leakage coefficient, and this could explain why the leakage flow varies in the experiments.

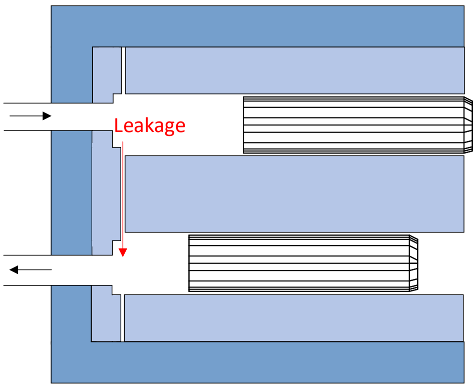

Figure F.2: Low leakage coefficient.

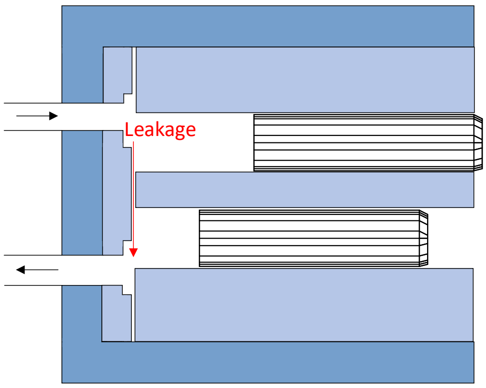

Figure F.3: High leakage coefficient.

G | Euler Lagrange Study

In order to study the different terms in the Euler-Lagrange equations then a sweep has been conducted for θ_1 and θ_2.
The values for θ_1 ranges from $\theta_{1,min}$ to $\theta_{1,max}$. These values corresponds to the minimum and maximum lengths of the cylinder.
The values for θ_2 ranges from $-4 \cdot 10^{-5}$ [rad] to $4 \cdot 10^{-5}$ [rad]. These values have been determined by running a simulation. In the simulation θ_2 ranged from $-2 \cdot 10^{-5}$ [rad] to $2 \cdot 10^{-5}$ [rad]. A safety margin has been added to these results.

D-matrix

In appendix E the expression for the D-matrix is derived, and it is repeated in equation G.1.

$$\underline{\underline{D}} = \begin{bmatrix} m_1 l_{cm1}^2 + m_2[|AD|^2 + l_{cm2}^2 + 2|AD|l_{cm2}^2 + 2|AD|l_{cm2} \cdot cos(\theta_2)] + I_1 + I_2 & m_2[l_{cm2}^2 + |AD|l_{cm2} \cdot cos(\theta_2)] + I_2 \\ m_2[l_{cm2}^2 + |AD|l_{cm2} \cdot cos(\theta_2)] + I_2 & m_2 l_{cm2}^2 + I_2 \end{bmatrix} \tag{G.1}$$

$$\underline{\underline{D}} = \begin{bmatrix} d_{11} & d_{12} \\ d_{21} & d_{22} \end{bmatrix} \tag{G.2}$$

It can be seen that the entrance d_{22} is constant, and thus the entrance is not studied. A sweep for d_{11}, d_{12} and d_{21} have been conducted and the results can be seen in figure G.1 and G.2.

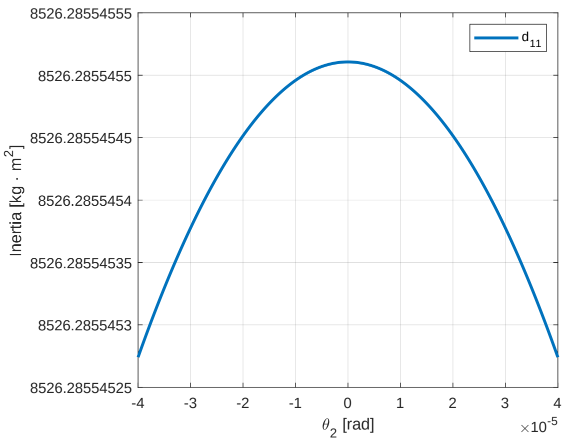

Figure G.1: d_{11} for varying θ_2.

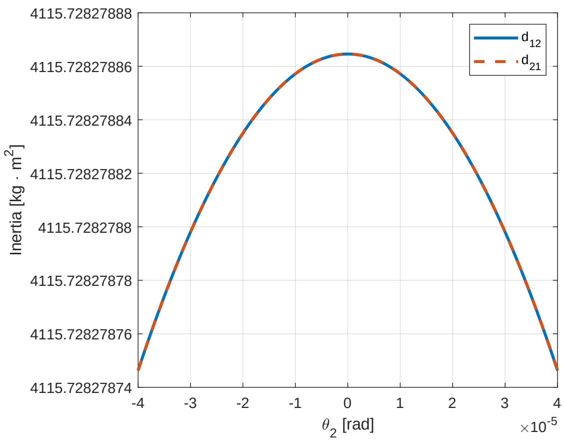

Figure G.2: d_{12} and d_{21} for varying θ_2.

Based on figure G.1 and G.2 it is concluded that $\underline{\underline{D}}$ can be treated as constant (The constant D-matrix is denoted D_0).

Furthermore, the inverse of D_0 is used to calculate the angle accelerations, and the inverse is seen in equation G.3.

$$\underline{\underline{D}}_0^{-1} = \frac{1}{d_{11}d_{22} - d_{12}d_{21}} \begin{bmatrix} d_{22} & -d_{12} \\ -d_{21} & d_{11} \end{bmatrix} = \begin{bmatrix} d_a & d_b \\ d_c & d_d \end{bmatrix} \tag{G.3}$$

C-matrix

In order to study if the term $\underline{\underline{C}}(\underline{\theta}, \underline{\dot{\theta}})\underline{\dot{\theta}}$ can be neglected from the Euler-Lagrange equations then a simulation has been conducted. The input for the simulation is seen in figure 5.1, and it is the same input as when then model is validated.

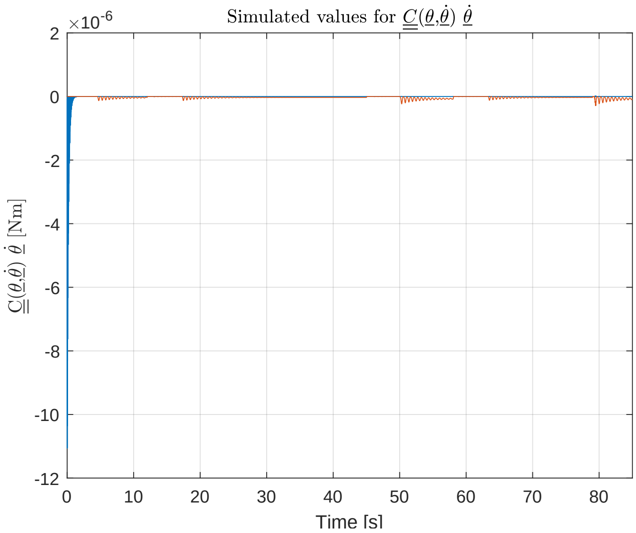

Figure G.3: Simulation results for $\underline{\underline{C}}(\underline{\theta}, \underline{\dot{\theta}})\underline{\dot{\theta}}$.

Based on figure G.3 it is concluded that the term $\underline{\underline{C}}(\underline{\theta}, \underline{\dot{\theta}})\underline{\dot{\theta}}$ can be neglected during the linearisation of the model.

ϕ-vector

In appendix E the expression for the ϕ-vector is derived, and it is repeated in equation G.4.

$$\underline{\phi} = \begin{bmatrix} \phi_1 \\ \phi_2 \end{bmatrix} = \begin{bmatrix} m_1 g l_{cm1} \cdot cos(\theta_1) + m_2 g |AD| \cdot cos(\theta_1) + m_2 g l_{cm2} \cdot cos(\theta_1 + \theta_2) \\ m_2 g l_{cm2} \cdot cos(\theta_1 + \theta_2) + k_s \theta_2 \end{bmatrix} \tag{G.4}$$

As it can be seen in the expression for ϕ_1 (equation G.4) then θ_2 only contributes to a very small margin. Therefore ϕ_1 is plotted for $\theta_2 = 0$ rad. This can be seen in figure G.4. Based on figure G.4 it is concluded ϕ_1 needs to be linearised. It is chosen to neglect the contribution from θ_2 during the linearisation of ϕ_1.

$$\phi_1(\theta_1) \approx \phi_1(\theta_{10}) + \underbrace{\frac{\partial \phi_1}{\partial \theta_1}\bigg|_{\theta_{10}}}_{K_{\phi 1}} (\theta_1 - \theta_{10}) \tag{G.5}$$

$$\Delta\phi_1 = K_{\phi 1}\Delta\theta_1 \tag{G.6}$$

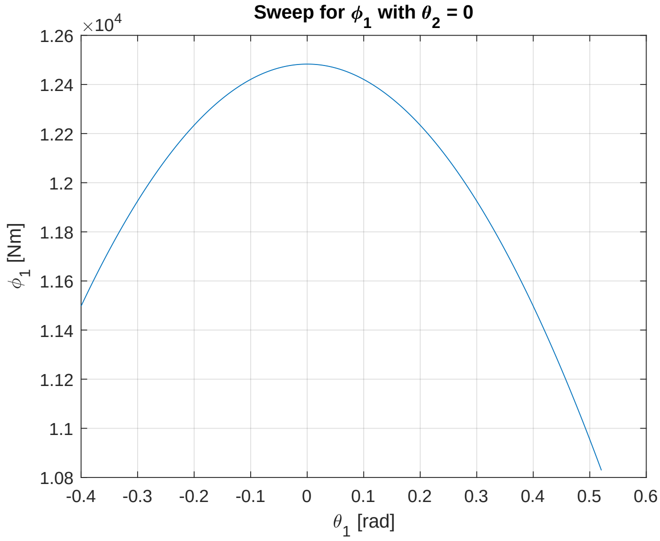

Figure G.4: Sweep for ϕ_1 with $\theta_2 = 0$.

The expression for ϕ_2 is examined first by keeping $\theta_2 = 0$. This can be seen in figure G.5. Based on figure G.5 it is chosen to linearise the expression for ϕ_2

$$\phi_2(\theta_1, \theta_2) \approx \phi_2(\theta_{10}, \theta_{20}) + \underbrace{\frac{\partial \phi_2}{\partial \theta_1}\bigg|_{\theta_{10},\theta_{20}}}_{K_{\phi 2}}(\theta_1 - \theta_{10}) + \underbrace{\frac{\partial \phi_2}{\partial \theta_2}\bigg|_{\theta_{10},\theta_{20}}}_{K_{\phi 3}}(\theta_2 - \theta_{20}) \tag{G.7}$$

$$\Delta\phi_2 = K_{\phi 2}\Delta\theta_1 + K_{\phi 3}\Delta\theta_2 \tag{G.8}$$

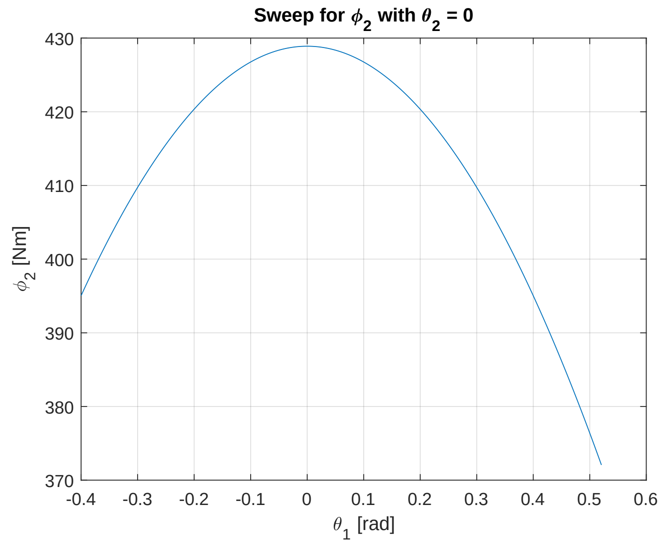

Figure G.5: Sweep for ϕ_2 with $\theta_2 = 0$.

A summery of the study-results for ϕ_1 and ϕ_2 can be seen in equation G.9 and G.10

$$\phi_1 = \underbrace{m_1 g l_{cm1} \cdot cos(\theta_1) + m_2 g|AD| \cdot cos(\theta_1) + m_2 g l_{cm2} \cdot cos(\theta_1 + \theta_2)}_{\text{Linearised with respect to } \theta_1} \tag{G.9}$$

$$\phi_2 = \underbrace{m_2 g l_{cm2} \cdot cos(\theta_1 + \theta_2) + k_s \theta_2}_{\text{Linearised with respect to } \theta_1 \text{ and } \theta_2} \tag{G.10}$$

Another approach which could have been taken was to see the contribution from the gravitational forces as a disturbance. However, as seen in figure G.4 and G.5 then $\underline{\phi}$ varies, and thus it is decided to linearise the expressions.

Results of Euler-Lagrange Study

Based on the study then it is decided to keep the D-matrix constant ($\underline{\underline{D}}_0$). Furthermore, it is chosen to neglect the expression for $\underline{\underline{C}}(\underline{\theta}, \underline{\dot{\theta}})\underline{\dot{\theta}}$. Lastly, it is chosen to linearise the expressions for $\underline{\phi}$.
Hereby the simplified and linear expression for the Euler-Lagrange expression are seen in equation G.11.

$$\underline{\ddot{\theta}} = \underline{\underline{D}}_0^{-1}(\underline{\theta})[\underline{\tau} - \underline{\phi}(\underline{\theta})] \tag{G.11}$$

The viscous friction is also added to equation in order to see the whole, linear expression for the Euler-Lagrange equations. This can be seen in equation G.12. It should be noted that the Δ-signs are omitted.

$$\underline{\ddot{\theta}} = \underline{\underline{D}}_0^{-1}(\underline{\theta}) \left(\begin{bmatrix} \tau_1 \\ 0 \end{bmatrix} - \begin{bmatrix} B_\omega \dot{\theta}_1 \\ B_s \dot{\theta}_2 \end{bmatrix} - \begin{bmatrix} K_{\phi 1} \theta_1 \\ K_{\phi 2} \theta_1 + K_{\phi 3} \theta_2 \end{bmatrix} \right) \tag{G.12}$$

H | Passive Pressure Feedback

In order to damp the system, it is decided to test if passive pressure feedback could be a solution. The gain K_{PF} is designed based on an analysis of the linear system. However, before the design procedure is begun, then the linear system is simplified.

Simplifying the Linear System

In order to calculate an appropriate gain for the pressure feedback then the transfer function derived from the state space model is simplified. The simplified block diagram representation is seen in figure H.1.

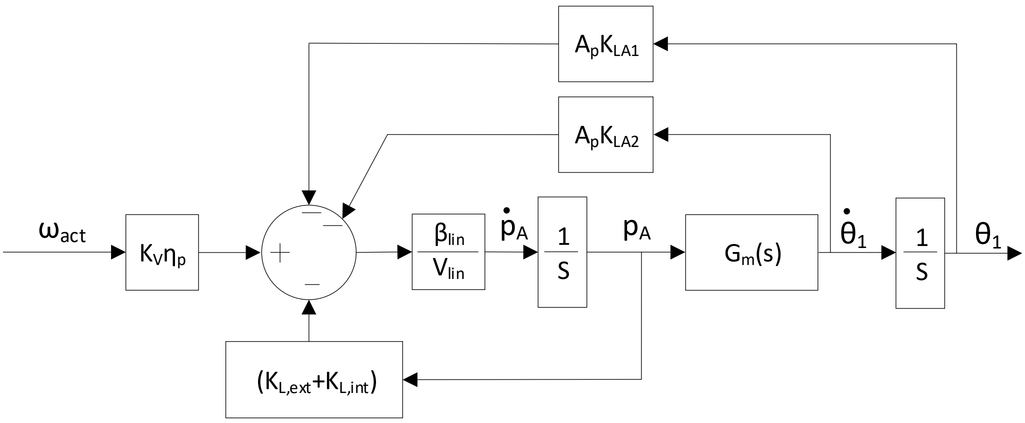

Figure H.1: Simplified block diagram for the linear model.

Based on figure H.1 it can be seen that the motor dynamics have been neglected. Furthermore, the $G_m(s)$ is a first order system which approximates the mechanical dynamics.

$$G_m(s) = \frac{K_{m1}}{K_{m2}s + K_{m3}} \tag{H.1}$$

Now the system is put into state space form in the equations below.

$$\begin{bmatrix} x_1 \\ x_2 \\ x_3 \end{bmatrix} = \begin{bmatrix} \theta_1 \\ \dot{\theta}_1 \\ p_A \end{bmatrix} \quad , \quad \begin{bmatrix} \dot{x}_1 \\ \dot{x}_2 \\ \dot{x}_3 \end{bmatrix} = \begin{bmatrix} \dot{\theta}_1 \\ \ddot{\theta}_1 \\ \dot{p}_A \end{bmatrix} \tag{H.2}$$

$$\underline{\underline{A}x} = \begin{bmatrix} 0 & 1 & 0 \\ 0 & -\frac{K_{m3}}{K_{m2}} & \frac{K_{m1}}{K_{m2}} \\ -ApK_{LA1}\frac{\beta_{lin}}{V_{lin}} & -ApK_{LA2}\frac{\beta_{lin}}{V_{lin}} & -(K_{L,ext} + K_{L,int})\frac{\beta_{lin}}{V_{lin}} \end{bmatrix} \begin{bmatrix} \theta_1 \\ \dot{\theta}_1 \\ p_A \end{bmatrix} \tag{H.3}$$

$$\underline{\underline{B}}\underline{u} = \begin{bmatrix} 0 \\ 0 \\ \frac{K_V \eta_p \beta_{lin}}{V_{lin}} \end{bmatrix} \omega_{act} \tag{H.4}$$

In figure H.2 the difference between the original transferfunction and the simplified transfer function is seen. It can be seen that the 2 transfer functions are similar, and thus the simplified transfer function can be used for designing pressure feedback.

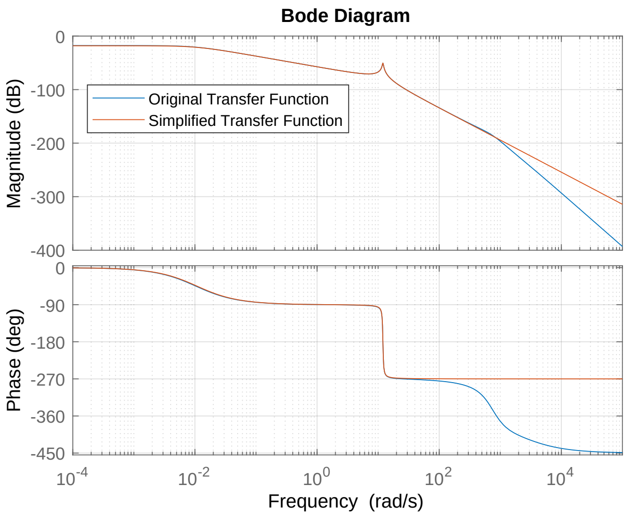

Figure H.2: Simplified block diagram for the linear model.

Passive Pressure Feedback

In order to see the effect of the pressure feedback then the simplified 3^{rd} order system is analysed. It should be noted that the outermost loop has been neglected (1^{st} order system), and instead it is replaced with a free integrator. This replaced it deemed acceptable for this investigation because as seen in the bodeplot in figure H.2 then the first order system does not influence the second order system. The block diagram of the second order system is seen in figure H.3.

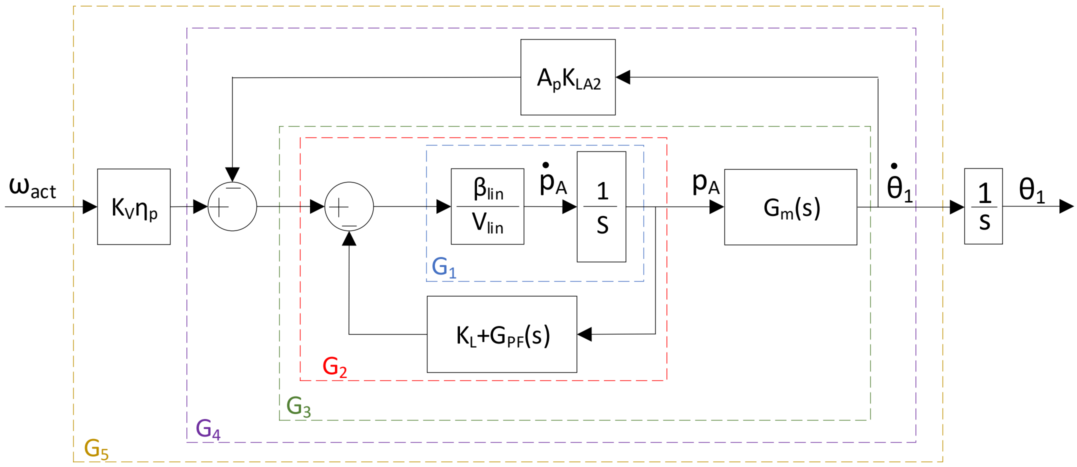

Figure H.3: Block diagram representation for the simplified transfer function.

The transfer function G_5 is seen in equation H.5

$$G_5 = \frac{K_V \cdot \eta_p \cdot K_{m1} \cdot \beta_{lin}}{V_{lin}K_{m2}s^2 + ((K_L + G_{PF})\beta_{lin}K_{m2} + V_{lin}K_{m3})s + A_pK_{LA2}\beta_{lin}K_{m1} + (K_L + G_{PF})\beta_{lin}K_{m3}} \tag{H.5}$$

Based on equation H.5 then the eigenfrequency, the damping and the steady state magnitude can be derived to the equations below.

$$\omega_n = \sqrt{\frac{A_pK_{LA2}\beta_{lin}K_{m1} + (K_L + G_{PF})\beta_{lin}K_{m3}}{V_{lin}K_{m2}}} \tag{H.6}$$

$$\zeta = \frac{1}{2\omega_n} \cdot \frac{(K_L + G_{PF})\beta_{lin}K_{m2} + V_{lin}K_{m3}}{V_{lin}K_{m2}} \tag{H.7}$$

$$G_5(0) = \frac{K_V \cdot \eta_p \cdot K_{m1} \cdot \beta_{lin}}{ApK_{LA2}K_{m1} + (K_L + G_{PF})\beta_{lin}K_{m3}} \tag{H.8}$$

The pressure feedback gain is calculated based on equation H.7. A damping of 0.707 is desired, and thus equation H.7 is solved for this value. Hereby the the pressure feedback gain K_{PF} is calculated.

$$K_{PF} = 2.733 \cdot 10^{-11} \tag{H.9}$$

The calculated gain K_{PF} is now implemented in the full state space model, and the effect of the gain K_{PF} can be seen in the bode diagram in figure H.4.

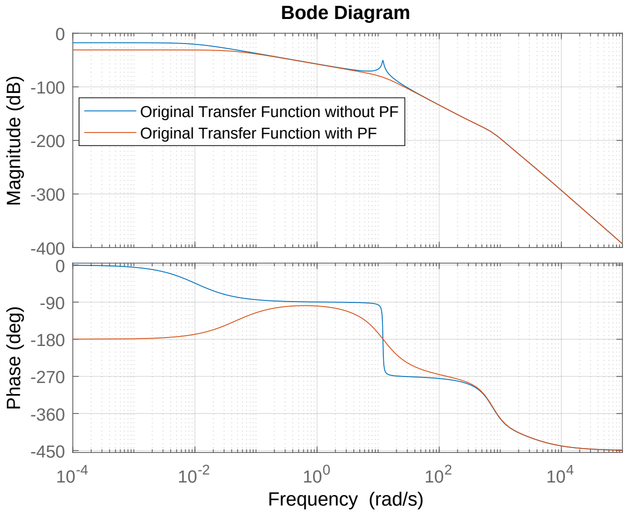

Figure H.4: Bode diagram showing the effect of the pressure feedback without HP.

Based on figure H.4 it can be seen that the desired damping effect is achieved. However, it can also bee observed that pressure feedback decreases the DC value significantly, and therefore it is chosen not to implement the passive pressure feedback.

I | 3/2-Valve Model

The flow directions Q_{in} and Q_{out} are defined as in figure I.1. Furthermore, the equation for Q_{in} and Q_{out} is seen in equation I.1.

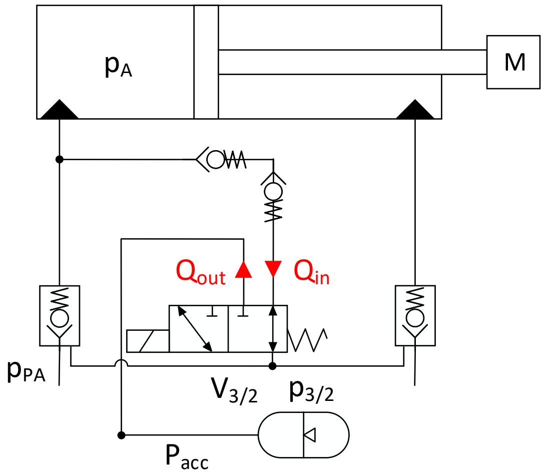

Figure I.1: Flow directions in the 3/2-valve model.

$$
\begin{aligned}
Q_{in} &= x_v \cdot K_{3/2} \cdot \sqrt{|p_A - p_{3/2}|} \\
Q_{out} &= -(1 - x_v) \cdot K_{3/2} \cdot \sqrt{|p_{acc} - p_{3/2}|} && \big\{ p_A > p_{3/2} \quad and \quad p_{acc} > p_{3/2} \\
Q_{in} &= -x_v \cdot K_{3/2} \cdot \sqrt{|p_{3/2} - p_A|} \\
Q_{out} &= -(1 - x_v) \cdot K_{3/2} \cdot \sqrt{|p_{acc} - p_{3/2}|} && \big\{ p_A < p_{3/2} \quad and \quad p_{acc} > p_{3/2} \\
Q_{in} &= x_v \cdot K_{3/2} \cdot \sqrt{|p_A - p_{3/2}|} \\
Q_{out} &= (1 - x_v) \cdot K_{3/2} \cdot \sqrt{|p_{3/2} - p_{acc}|} && \big\{ p_A > p_{3/2} \quad and \quad p_{acc} < p_{3/2} \\
Q_{in} &= -x_v \cdot K_{3/2} \cdot \sqrt{|p_{3/2} - p_A|} \\
Q_{out} &= (1 - x_v) \cdot K_{3/2} \cdot \sqrt{|p_{3/2} - p_{acc}|} && \big\{ p_A < p_{3/2} \quad and \quad p_{acc} < p_{3/2} \\
Q_{in} &= 0 \\
Q_{out} &= 0 && \big\{ Else
\end{aligned}
\tag{I.1}
$$

Where the position signal is either 1 or 0, and it is assumed that valve position x_v can be approximated by a fast 1^{st} order system.
The constant $K_{3/2}$ has been determined by approximating the datapoints seen in figure I.2.

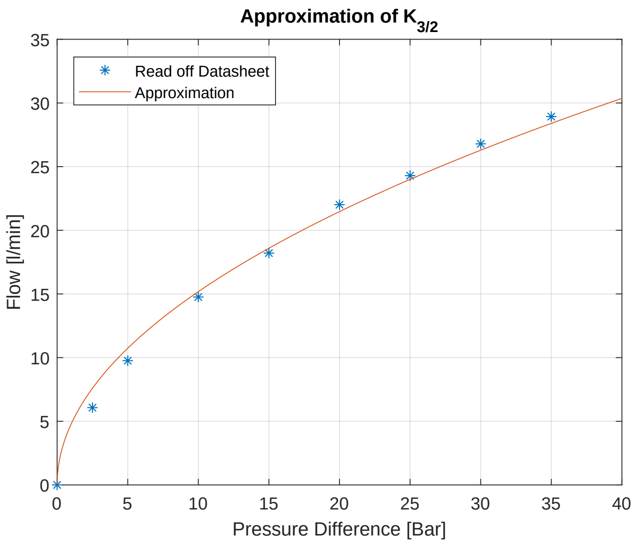

Figure I.2: Comparison between datapoints and approximation [7].

The continuity equation for $\dot{p}_{3/2}$ is given by equation I.2.

$$\dot{p}_{3/2} = (Q_{in} - Q_{out}) \cdot \frac{\beta_{eff}}{V_{3/2}} \tag{I.2}$$

It should be noted that the volume $V_{3/2}$ has been subtracted from the volume V_{PA} (see figure 4.3) such that the same amount of oil is present in the system after the modifications. The cylinder and accumulator model are also modified, and the modifications (marked with red) can be seen equation I.3.

$$\begin{aligned} \dot{p}_A &= (Q_A - A_p\dot{x} - {\color{red}Q_{in}}) \cdot \frac{\beta_{eff}}{A_p x + V_{01}} \\ \dot{p}_{acc} &= (Q_{out,orifice} - Q_{out,CV5} + Q_{ext,leak} + {\color{red}Q_{out}}) \cdot \frac{1}{\frac{V_{acc}+V_0-V_g}{\beta_{eff}} + \frac{1}{\gamma} \cdot \frac{V_g}{p}} \end{aligned} \tag{I.3}$$

J | PFF Controller

The idea is to design a P-controller for pressure feed forward such that the the position drop of the cylinder can be reduced. It is decided to design a conservative P-controller due to time limitations. However, a gain schedule controller could be a solution for further work, because the developed transfer function depends both on cylinder position and the bulk modulus value.

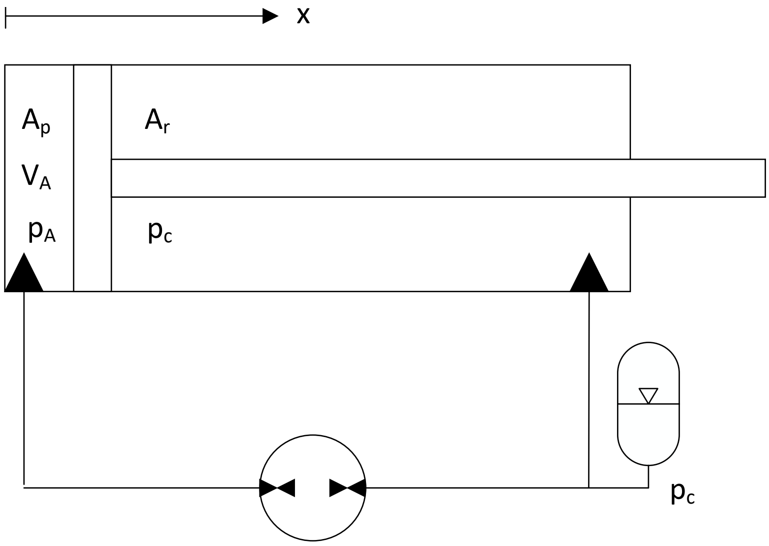

Figure J.1: Sketch used to show the cylinder position during the linearisation.

State Space - POCV's opened

The derivation of the state space representation is based on the principles as in section 8.1. Therefore it will not be repeated here, only the state space representation is given.

$$\underline{x} = \begin{bmatrix} x_1 \\ x_2 \\ x_3 \end{bmatrix} = \begin{bmatrix} p_A \\ \omega_{act} \\ \dot{\omega}_{act} \end{bmatrix} \quad , \quad \underline{\dot{x}} = \begin{bmatrix} \dot{p}_A \\ \dot{\omega}_{act} \\ \ddot{\omega}_{act} \end{bmatrix} \tag{J.1}$$

$$\underline{\underline{A}}\underline{x} = \begin{bmatrix} (-K_{L,ext} - K_{L,int}) \cdot \frac{\beta_A}{V_A} & K_V \cdot \eta_p \cdot \frac{\beta_A}{V_A} & 0 \\ 0 & 0 & 1 \\ 0 & -\omega_{n,m}^2 & -2\zeta_m \omega_{n,m} \end{bmatrix} \begin{bmatrix} p_A \\ \omega_{act} \\ \dot{\omega_{act}} \end{bmatrix} \tag{J.2}$$

$$\underline{\underline{B}}\underline{u} = \begin{bmatrix} 0 \\ 0 \\ \omega_{n,m}^2 \end{bmatrix} \omega_{ref} \quad , \quad \underline{\underline{C}}\underline{x} = \begin{bmatrix} 1 & 0 & 0 \end{bmatrix} \begin{bmatrix} p_A \\ \omega_{act} \\ \dot{\omega}_{act} \end{bmatrix} \tag{J.3}$$

The chosen linearisation point for the cylinder is chosen close to x = 0m because hereby the value for V_A is small. This means that the eigenvalue for the system is low, and this yields a conservative pressure controller design. Furthermore, through a simulation it is determined that the highest value for β_{eff} 7000 bar when the POCV's are opened. A safety margin has been added to this result, and thus it is decided to linearise the bulk modulus at $\beta_A = 8000$ bar.

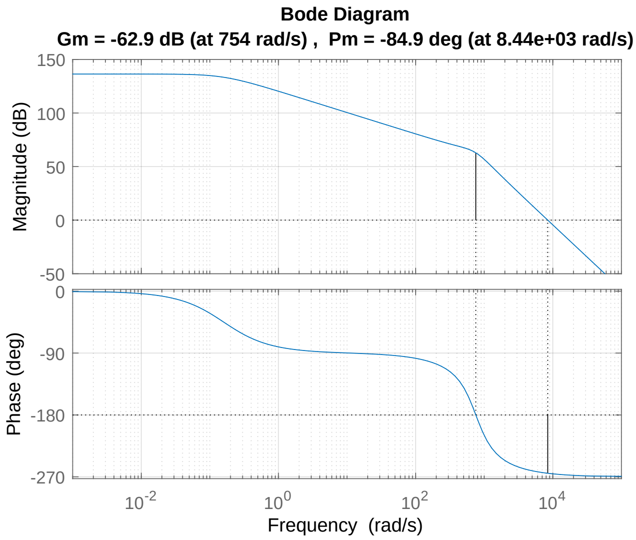

Figure J.2: Gain and phase margin for the system.

It is decided to design the P-controller such that a GM of 30 dB is reached. This is decided it yields a time constant of 0.0423 seconds. The time constant corresponds well with a sample time of 0.001 seconds because approximately 42 data points are measured during one time constant. Hereby the calculated K_p-value is seen in equation J.4.

$$K_{p,PFF} = \frac{1}{(61.8 + 30)} = 2.264 \cdot 10^{-5} \tag{J.4}$$

The system with the developed P-controller can be seen in figure J.3.

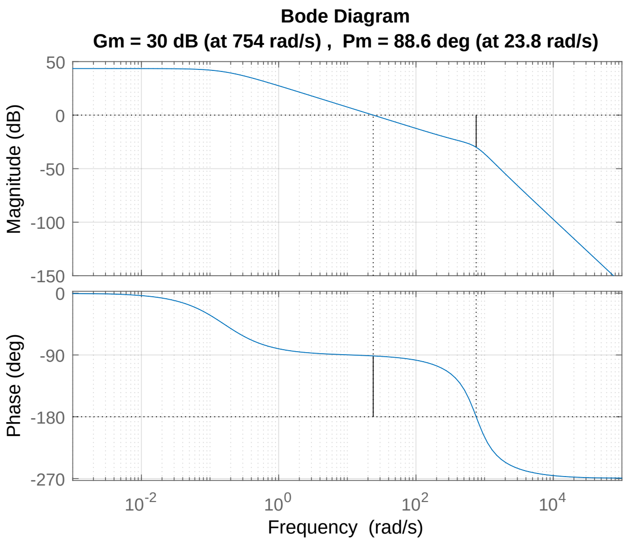

Figure J.3: Gain and phase margin for the system with P-controller.